Structure and Evolution of Circumstellar Envelopes and Outflows in Intermediate-mass Protostars.

Dissertation Presented
by
TAKAHASHI Satoko

Department of Astronomical Science,
School of Physical Science,
The Graduate University for Advanced Studies
2007

Table of Contents

Acknowledgments

The authour would like to thank all persons who have been assisting, and encouraging me, to complete this thesis.

First of all, the authour would like to give my special thanks to Prof. Ryohei Kawabe, my supervisor, for his much of continuous encouragement and invaluable comments, not only for scientific studies but also my astronomer life. The authour also gives my special thanks to Dr. Masao Saito, Dr. Shigehisa Takakuwa, my best supporter, for invaluable suggestions and comments on this work. They are always thoughtful and kind-hearted supervisors for me.

The authour is deeply indebted to the NMA members, Prof. Sachiko Okumura, Prof. Koh-Ichiro Morita, Dr. Kouichiro Nakanishi and Dr. Tomoka Tosaki for their effort to operate the NMA. Especially, Dr. Koichiro Nakanishi provide me much of knowledge about interferometric observations during past 5 years. The authour is grateful to Hiroyuki Iwashita, Kazuyuki Handa, Toshikazu Takahashi for excellent technical works for the NMA. The authour also thanks to the NRO 45 m team for supporting me the common use observations. Especially, The authour would like to thank Dr. Norio Ikeda for a kindly advice in the 45 m observations.

The authour would like to deeply acknowledge Dr. Tsuyoshi Sawada, Dr. Takeshi Kamazaki, and ASTE team for their support during the ASTE observations at Chile. The authour also acknowledges Prof. Motohide Tamura, Mr. Nobuhiko Kusakabe, Ms. Akika Ishihara and SIRIUS/IRSF team for providing me the chance to have a collaboration in near-infrared astronomy. The authour has also been encouraged through discussions by many astronomers, particularly Mr. Yoshito Shimajiri, Dr. Daisuke Iono, Dr. Kazuya Saigo, Dr. Takeshi Nakazato, Dr. Shuro Takano, Dr. Harold Butner, Dr. Hiroyuki Nakanishi, Mr. Yasutaka Kurono, and Mr. Takashi Tsukagoshi.

The authour also thanks to Dr. Dough Johnstone and Dr. Darek Lis for providing us the submillimeter continuum data taken by JCMT and CSO, and respectively. The authour also thanks the thesis committee for the constructive comments that have helped to improve this thesis.

A part of ASTE study was financially supported by the MEXT Grant-in Aid for Scientific Research on Priority Areas No. 15071202. The authour is supported by the Grant-in -Aid for Japan Society for the Promotion of Science (JSPS) for Young Scientists by the Ministry of Education, Science, Sports and Culture.

The authour deeply thanks to Dr. Aya Yamauchi, Dr. Ayumi Asai, Dr. Naoko Sato for discussion and continuous encouragement as a friend. The authour also thanks to Ms. Mitsue Takasawa, Ms. Setsuko Koike, Mr. Mitsuaki Nimura, Ms. Toeko Nakamura, Ms. Chieko Miyazawa, and Mr. Kazuhiko Miyazawa for supporting Nobeyama life, and Ms. Rie Miura and Ms. Aya Higuchi for talking me with.

Finally, the authour would like to thank my friends and family, especially my mother always support and encourage me.

Abstract

In the last two decades, the development of millimeter interferometers has enabled us to establish a standard scenario of sun-like ($M_*\sim1\ M_\odot$) star formation. However, details of formation and evolution of more massive stars ($\geq 2\ M_\odot$), that is, intermediate- and high-mass protostars, remain poorly understood. Studies of the formation and evolution of intermediate-mass protostars will allow us to understand whether the established low-mass star-formation scenario is applicable to a wide range of protostar masses. However, there is no systematic observation toward intermediate-mass protostars. It is important to directly verify the accretion and dissipation (or destruction) processes of dense gas envelopes around intermediate-mass protostars. For these purposes, The author has performed multi-wavelength and multi-line survey observations toward intermediate-mass pre- and proto-stellar candidates in the Orion Molecular Cloud -2/3 region (OMC-2/3). The OMC-2/3 region is one of the best targets to conduct a systematic survey of intermediate-mass protostars, because all of the sources are in the same distance and under the similar starforming environment.

Using the NMA, ASTE and SIRIUS/IRSF, The author observed the 3.3 mm dust continuum, $H^{13}CO^+$(1–0), CO(1–0), CO(3–2) emissions, and near infrared (JHK_s-band) continuum emissions toward the entire sample of intermediate-mass pre- and proto-stellar candidates in the Orion Molecular Cloud -2/3 region (OMC-2/3). Based on our $H^{13}CO^+$(1–0), 3.3 mm continuum, CO(3–2) and JHK_s results, combined with the published VLA 3.6 cm and the archived 24 *mu*m data taken by Spitzer, The author unveiled the evolutionary changes, morphology and velocity structures of the dense envelopes and accompanied CO outflows around intermediate-mass protostars for the first time. The author classified these intermediate-mass pre- and proto-stellar candidates into three evolutionary phases as (i) pre-stellar phase, (ii) Class A phase, and (iii) Class B phase. Pre-stellar sources have no compact dusty emission taken with the NMA and 24 μm source, suggesting no any signature of dense ($> 10^7$ cm^{-3}) and hot ($>$ 100 K) envelopes. In this phase, there are no signature of jets/outflows. Class A sources are corresponding to the earlier evolutionary phase of the protostellar cores, which are associated with compact dust emission and 24 μm sources, suggesting the presence of the heating source. 0.1 pc scale CO outflows are also detected in this phase. Finally, Class B sources correspond to the later evolutionary phase of the protostellar cores, which are associated with the compact dust and 24 μm sources. 0.5 – 1.0 pc scale CO outflow and free-free jet are associated with these objects. In addition, our JHK_s images show a reflection nebula, suggesting the formation of the cavity along the CO outflows. In this phase, the author detected fan-shaped $H^{13}CO^+$ envelopes with a size scale of 0.1 pc.

The author also found that the CO outflow momentum increases from the evolutionary sequence of Class A to Class B. The 24 μm peak flux also increases from the evolutionary sequence of Class A to Class B. The author suggests that the enhancement of the 24 μm flux is caused by the growth of the cavity (i.e., the CO outflow destroys the envelope) as the evolutionary sequence. Our results show that the dissipation of the dense gas envelope plays an essential role in the evolution of the intermediate-mass protostars.

Chapter I

General Introduction

1. Historical Background

Star-formation is one of the most important issues in modern astronomy, which is deeply related to the formation and evolution of galaxies to the origin of planetary systems. In 1980s, the success of Infrared Astronomical Satellite (IRAS) mission enables us to study a new era of star-formation. IRAS produced the all-sky survey at wavelengths of 12, 25, 60 and 100 μm. One of the major results of IRAS is discovery of many young stellar objects (YSOs). IRAS also discovered the peculiar objects which have luminosities same as typical T Tauri stars (i.e., YSOs), but with the excess emission, peaking at 60 –100 μm (Beichman et al. 1986). Now, these objects are generally identified as a "protostellar cores", which are the earliest evolutionary stage of the pre-main sequence stars and are still surrounded by much of the material from its parent cores. The dusty envelope of these objects absorb energy from the central star at optical and near-infrared wavelengths, and re-emit this energy at far-infrared wavelength. Then the envelopes are sufficiently transparent for the radiation to escape. Theoretical models of the dust emission from protostellar envelopes in gravitational free-fall can reproduce the observed infrared emission of these heavily-extincted young stellar objects (Adams, Lada, & Shu 1987, Butner et al. 1991, Kenyon, Calvet, & Hartmann 1993).

Extensive IRAS surveys of the low-mass star forming region Taurus (e.g. Beichman et al. 1986, Cohen , Emerson & Beichman 1989, Kenyon et al. 1990, 1994) indicate that 10 % of total pre-main sequence population is in the "protostellar" phase. This result suggests that the time for protosellar collapse is similarly about 10 % of the age of the pre-main sequence stars, implying the estimated time-scale of protostars is approximately 10^5 yr. This time scale is roughly consistent with the expected time-scale of collapse for the formation of typical low-mass stars (Larson 1969*a*, *b*; Shu 1977)

At the same time developments of millimeter and submillimeter interferometers with higher-sensitivity and higher-spatial resolution have enabled us to directly image structures and kinematics of circumstellar material around protostellar cores. Observations with molecular line emission such as CO and its isotopes have directly revealed presence of Keplarian rotating disks around T Tauri stars whose radii is several $\times$ 100 AU (e.g. Kawabe et al. 1993, Guilloteau et al. 1998, Dutrey et al. 1998). Observations of protostars with a dense gas tracer such as $C^{18}O$, CS and $H^{13}CO^+$ have revealed extended envelopes with a typical size of several $\times$ 1000 AU and mass of 0.01 –0.1 $M_\odot$. These envelopes exhibit infall motion (i.e. dynamical collapse) toward the central stars with a typical mass accretion rate of several $\times$ 10^{-6} – 10^{-5} $M_\odot$ (Hayashi et al. 1993, Saito et al. 1996, Momose et al. 1998).

In the following sections, The author will introduce the scenario of early evolution of low- and high-mass stars and unresolved issues of star formation study.

1.1. A Brief Evolutionary Scenario of Low-mass Young Stars

Isolated low-mass stars are formed in molecular cloud cores with their mass of order of several $\times$ $0.1 - -1$ $M_\odot$, densities of $\sim$ 10^4 cm^{-3}, radii of approximately 0.1 pc and temperatures of 10 K (e.g. Myers & Benson 1983, Myers & Goodman 1988 *a*, *b*, Onishi et al. 2002). These cores become gravitationally unstable and collapses will ensure when the balance between the self-gravity, inner pressures and outer pressures has lost owing to such as magnetic field diffusion, or some compression from outer environment (e.g., Adams, Lada, & Shu 1987). After that, the

central star is formed and that circumstellar material dynamically accreted to the central star (e.g., Hayashi et al. 1966, Larson et al. 1969, Shu et al. 1977, Hayashi et al. 1993). In this stage, there is a circumstellar envelope with a typical size of a few thousands AU surrounding the central star which exhibits an infalling motion (Hayashi et al. 1993) and also accompanied by an active molecular outflows (e.g. Snell et al. 1980). After the protostellar phase, the central star become visible and its associated circumstellar disk have appeared (T Tauri stars).

YSOs are frequently classified by the shape of spectral energy distributions (SEDs) from near- to far-infrared spectral regions, which emphasizes the properties of circumstellar dust and traces a evolutionary sequence of YSOs (Lada & Wilking 1984; Lada 1987). A classification of YSOs based on SED is categorized into three with a spectral index,

$$s = \frac{d\log\nu F_\nu}{d\log\nu}. \tag{I.1}$$

where s of the SED is measured at the range of 1–10 μm (e.g. Adams, Lada, & Shu 1987, Lada 1991). class I sources have a positive value of s = 0 to 3 whose SED is broader than a single black body. For class II sources have a negative value of s = -2 to 0. class III sources have a negative value of s = -3 to -2, suggesting a SED from a single black body (i.e. central star). After categorization of classes The author, II, to III, and much younger objects than those of YSOs are classified as class 0 objects. The class 0 objects were defined as a source with a ratio $L_{\rm bol}/L_{\rm smm} < 200$ and that the SEDs are well fitted by their thermal radiation from cold black bodies with a temperature of several $\times$ 10 K (Andre et al. 1993). In this phase, the central stars and its associated disks have grown thorough mass accretion from the envelopes, and the accreted gas associated with an angular momenta have released through the powerful bipolar outflows. The typical age of class 0 objects is approximately 10^4 yr.

Class I sources are embedded protostars surrounded by significant circumstellar material. The peak of SED is far-infrared which comes from re-emitted emission from a central star. Most of its luminosity from these protostars are through to be released by the accretion energy (i.e., accretion luminosity). The typical time scale of class I objects is approximately 10^5 yr. In class II phase, circumstellar materials are already dissipated and that the central star becomes visible. These sources are categorized as a classical T Tauri stars (CTTSs), and have a compact circumstellar disks with a size scale and mass of several $\times$ 100 AU and several $\times$ 0.001 – 0.1 $M_\odot$, respectively (e.g., Kitamura et al. 2002). The infrared excess emission from circumstellar disks are observed in SEDs. The typical time scale of class II objects is approximately 10^6 yr. When coagulation of the dust particles has progressed and planetesimals have formed, infrared excess emission has disappeared. These objects are called weak line T Tauri stars (WTTSs) and categorized as class III objects. The typical time scale of class III object is approximately 10^7 yr. After the stage of class III, the stars go in to the main-sequence stages.

1.2. Molecular Outflows associated with Low-mass Protostars

CO molecular outflows are a fairly common phenomenon in star forming regions (e.g. Arce et al. 2005, and Bachiller & Tafalla 1999 for reviews). The CO outflows are thought to be directly associated with the main accretion phase of low-mass proto-stars, and its detection is usually used to identify protostars in dense cores. The geometry of the outflow is also a key for identifying

dynamical mass infall in the disk-like envelopes around central protostars (e.g., Hayashi et al. 1993, Momose et al. 1998, Saito et al. 2001). On the other hand, the CO outflows interact with both gas in the dense cores itself and the larger scale interstellar ambient material, and accelerate the dissipation of the dense cores and might cause successive gas compression via shock. Physical nature of CO outflows has been intensively studied so far for those associated with low mass protostars (e.g., Bontemps et al. 1996, Saraceno et al. 1996). One of the interesting results about relation between outflows and circumstellar material that the momentum rate of the molecular outflow decreases with time during the accretion phase and that the outflow is most powerful in the earliest stage at the Class 0 phase in low-mass protostars (i.e, $F_{\rm CO} - L_{\rm bol}$ correlation; Bontemps et al. 1996). These results suggest that outflow activities reflect a corresponding decay in the mass accretion rate.

Recent works revealed that outflow significantly interacts with a natal core even if in the earlier evolutionary stage of protostars (e.g., Class 0 Object: IRAM 04191+1522 observed by Takakuwa et al. 2003). A high-angular resolution imaging survey toward low-mass stars have revealed that the outflow opening angle widens as the nascent star evolves due to erosion the circumstellar envelope through the entrainment of the outer envelope gas, and the dense envelope with a size scale of several $\times$ 10^3 AU is dissipated (e.g., Saito et al. 2001, Arce et al. 2005). They also suggest that the mass of these envelopes are decrease with protostellar to YSO evolution. These results indicate that the evolution of outflows and dissipation process of natal cores/envelopes are significantly important to consider evolution of central stars, because these phenomena prevent the mass accretion process which determines the final mass of the central star (e.g., Nakano et al. 1995)

1.3. The Studies of High-mass young stars

Majority (90 %) of stars formed in embedded clusters in our galaxy (Lada & Lada 2003). and most of massive stars ($M_* > 8\ M_\odot$) located at the center of these clusters and have a significant influence on these environment. However, their formation remains poorly understood, because these objects are distant from the sun ($d > 1$ kpc) and have complexity structure (i.e., member of cluster). In this section, The author make a brief summary of the current status in observational and theoretical side of the high mass YSOs.

One of the major problems to form massive stars exert on the surrounding material. In principle, radiation pressure could be strong enough to stop further accretion (e.g., Yorke and Sonnhalter, 2002). In theoretical, there are two approaches to overcome these problems, although The author have no clear answer in each approach. The first is an "accretion-based picture" which composed of two possibilities. One possibility is that turbulent cloud cores (or clumps) have much higher accretion rates of the order $10^{-4} - 10^{-3}\ M_\odot\ {\rm yr}^{-1}$ compared to $10^{-6} - 10^{-5}\ M_\odot\ {\rm yr}^{-1}$ for low-mass star formations (e.g., McKee & Tan, 2003). Other possibility is that the mass accretion is caused by via disks (e.g., York & Sonnhalter 2002). In contrast, a different paradigm to form massive stars have been proposed based on the observational fact that massive stars always form at the dense centers of stellar clusters: "the coalescence scenario". In this scenario, the protostellar and stellar densities of a forming massive cluster are high enough ($\sim 10^8\ {\rm pc}^{-3}$) that protostars undergo physical collisions and merge, thereby avoiding the effect of radiation pressure (e.g., Bonnell et al. 1998).

In observational side, candidates of high-mass disks (rotating torus) have been reported in

several early -type B YSOs (e.g., Cesaroni et al. 2005 for a review, Patel et al. 2005). Furthermore, recent observational results may suggest non-spherical mass accretion via disk around a later of the O type YSOs (Beltran et al. 2006). In addition, massive ($M_{\rm flow}$~10 $M_{\odot}$) and energetic ($P_{\rm CO}$~ a few $\times$ 100 $M_{\odot}$ km s^{-1}) outflows, are also detected toward high-mass protostellar candidates with their IRAS luminosities from 10^3 – 10^5 $L_{\odot}$ with a high outflow detection rate of 90 % (Zhang et al. 2001). These results support that high-mass stars may form via an accretion -outflow process, similar to their low-mass counterpart.

2. Motivation of the Thesis

In the last two decades, the development of millimeter interferometers and infrared observations has enabled us to establish a standard scenario of sun-like (M_*~1 $M_{\odot}$) star formation (i.e., accretion and dissipation processes in envelopes; Hayashi et al. 1993, Ohashi et al. 1996, 1997, Momose et al. 1998, Saito et al. 1996, 2001) . On the other hand, formation and evolution of high-mass protostars ($M_* \geq 8$ $M_{\odot}$) remain poorly understood. Although recent observational studies with high-angular resolution may suggest that high-mass young stars also have accretion disks (e.g., Beltran et al. 2006). Study of the formation and evolution of intermediate-mass protostars ($2 \leq M_* \leq 8$ $M_{\odot}$) will allow us to understand whether the low-mass star-formation scenario is applicable to more massive star-formation. Figure 1 shows the schematic picture of the previously proposed evolutionary sequence of low- to high-mass YSOs (e.g., Adams, Lada & Shu 1987, Beuther et al. 2007). There are many of systematic observations toward low and high-mass young stars and that the evolutionary sequence are discussed through the difference of the gas status and kinematics (as shown in Figure 1). Further, in intermediate-mass region ($2 \leq M_* \leq 8$ $M_{\odot}$), there are several millimeter and infrared observations of later evolutionary phase of YSOs; Herbig Ae/Be stars (e.g., Hillenbrand 1995, Fuente et al. 2002; See Figure 2). In particular, Fuente et al. revealed that the relatively dense gas (n~10^3 cm^{-3}) traced by the ^{13}CO(1–0) emission is dispersed with YSO evolution between early Herbig Ae/Be star and ZAMS as shown in Figure 2. On the other hand, early evolutionary phase of intermediate-mass protostars were not well understood, because of the lack of systematic observations toward them. It is important to directly verify the accretion and dissipation (or destruction) processes of dense gas envelope around intermediate-mass pre- and proto-stellar candidates.

The final goal of the study is to obtain the unified picture of formation and evolution of low- to high-mass protostars. In this thesis, as a first step, the author focus on formation and evolution of the envelopes/outflows associated with the intermediate-mass pre- and protostellar candidates. Since intermediate-mass star-formation is less complicated than high-mass star-formation, it provide us a key to extend the low-mass scenario and to bridge a missing link between the high-mass and low-mass star formation. In this thesis, the author especially focuses on the following points,

- □ Classification of the evolutionary sequence of intermediate mass protostars, M_*~2-4 $M_{\odot}$ based on systematic survey observations and comparison of the low- and high- mass evolutionary pictures. Especially, Is the low-mass star formation picture with a disk accretion-outflow applicable to intermediate-mass counterparts ?
- □ Quantitative comparison of the physical properties of proto-stellar cores and associated outflows. Especially, does intermediate mass protostars have higher mass accretion (or

dissipation) and momentum rate of associated outflow than low mass counterparts ?

- □ Initial condition of intermediate-mass starforming cores. Is there difference of star-forming environment between intermediate-mass protostars and low-mass counterparts. The author would like discuss to the angular momentum, density and mass of dusty condensations.

3. The Observational Approach

3.1. Our Targets: Orion Molecular Cloud -2 and -3 region.

The Orion Molecular Cloud -2/3 region (OMC-2/3; d=450 pc; Genzel & Stutzki 1989), which is located at the northern part of Orion A giant molecular cloud, is one of the nearest active star-forming regions. There are 28 millimeter- and 33 submillimeter dust condensations in this region (Chini et al. 1997, Lis et al. 1998, Nielbock et al. 2003; See Figure 3 and Table 1). Although it cannot be excluded that this is an artifact of the IRAS detection limits, six condensations in OMC-3 millimeter sources associated with class 0-type SEDs by the L_{bol}/L_{smm} diagnose (Andre et al. 1993). In addition, the bolometric luminosity and core mass of these dust continuum sources are at least one order of magnitude larger than low-mass counterparts. Furthermore, the range of the bolometric luminosity and core mass are less than roughly factor of two * , suggesting that these continuum sources potentially form a similar mass intermediate-mass protostars (2-4 $M_{\odot}$ or a A0 star at the ZAMS). Hence, the OMC-2/3 region is one of the best targets to conduct a systematic survey of intermediate-mass protostars, because all of the sources are in the same distance and under the similar environment (e.g., similar chemical condition). This means that it is not needed to consider the difference of sensitivity or chemical affect caused by the samples in different starforming region which enable us to discuss the quantitative comparison of physical parameters. Table 2 summarizes physical properties of each core.

Until now, there are many of multi-wavelength surveys in the OMC-2/3 region. For example, 3.6 cm free-free jets are also detected toward 7 of the millimeter dust sources (Reipurth et al. 1999). Shock-excited H_2 knots, which trace a shock front of each flow, are associated with these embedded sources, identified by Yu et al. (1997) and Stanke et al. (2002). Aso et al. (2000) and Williams et al. (2003) made mapping observations in the CO(1–0) emission and identified nine of CO outflows associated with the millimeter sources in OMC-3 and northern part of OMC-2. These results strongly suggest that several cores in OMC -2/3 region are in the active proto-stellar phase. However, there was very few observational studies to focus on kinematics, physical properties and evolutionary phase of these cores.

3.2. Observational Strategies

As a first step, the author has performed unbiased outflow survey in CO(3–2) and JHK_S continuum emission toward OMC -2/3 with the ASTE telescope and the SIRIUS/IRSF. The author has also performed unbiased dense core survey in $H^{13}CO^+$(1–0) and 3.3 mm continuum emissions taken with the NMA, simultaneously. The author, here, also would like to mention

*Here, a few of peculiar sources (millimeter sources, MMS6 and FIR 4) are included in our samples.

that there are many data in different wavelength (i.e. radio to X-ray data) as archive or previous articles which enable us to obtain a comprehensive picture in each object. From combining these data, the author obtained structure and physical properties associated with intermediate-mass pre- and protostellar candidates in each object with a size scale of a few $\times$ 0.01 – 1 pc.

3.3. Molecular Line Probes

It is crucial to select proper tracers in order to study dense envelopes around protostellar candidates. The $H^{13}CO^+$ (1-0) molecular line ($n_{\rm crit} \sim 10^5$ cm^{-3}) is one of the promising tracers of moderately dense gas. For example, it is usually detected toward low- to intermediate-mass cores and envelopes (e.g., Ohnisi et al. 2000, Takakuwa et al. 2000, Saito et al. 2001, Fuente et al. 2005). The $H^{13}CO^+$ (1-0) molecular line is well known as an appropriate cold dense gas tracer such as infalling (and dissipating envelope) with a size scale of a few thousands AU. $H^{13}CO^+$(1-0) observations of dense gas in the Taurus Molecular Cloud complex have been carried out by Saito et al. (2001). They revealed that the dense gas dissipates as protostars evolution from class A (infalling envelope) to Class C (remnant of dense envelope). In addition, recent observational results suggest that the HCO^+ molecules are affected the chemical composition of the surrounding environment. In fact, HCO^+ abundances toward several of low-mass protostars are enhanced under the outflow region (Arce et al. 2006).

In the following, the formation process of $H^{13}CO^+$ molecule is briefly introduced. In pure gas-phase chemical evolutionary models in molecular clouds, chemistry of molecular clouds is non-equilibrium and time-dependent (e.g. Leung, Herbst, & Huebner 1984). The time dependence of molecular abundances is mainly due to the status of carbons. In the earlier evolutionary stage, carbons are mainly in the form of C^+ and C. On the other hand, in the later evolutionary stages carbons are mostly in the form of CO. The main formation process of the $H^{13}CO^+$ molecule are proposed as,

$$H_3^+ + {}^{13}CO \rightarrow H^{13}CO^+ + H_2 \qquad \text{(I.2)}$$

3.4. Thesis Outline

The outline of this thesis is as follows. In Chapter II, the author presents the results of the later evolutionary phase of protostellar core, MMS 7, and discuss the properties and mechanisms of dispersing dense gas. In Chapter III, the author shows the results of unbiased outflow survey observations in CO(3–2) emission with the Atacama Submillimeter Telescope Experiment (ASTE) and $JHK's$ observations with the SIRIUS/IRSF. In Chapter IV, the author shows survey observations of dense gas in $H^{13}CO^+$(1–0) and millimetric dust-continuum emissions with the Nobeyama Millimeter Array (NMA). Finally, the author discusses the formation and evolutionary scenario of intermediate-mass protostars in OMC-2/3 based on the above results (in Chapter II to IV), and compare with the established low and high-mass formation scenario in Chapter VI.

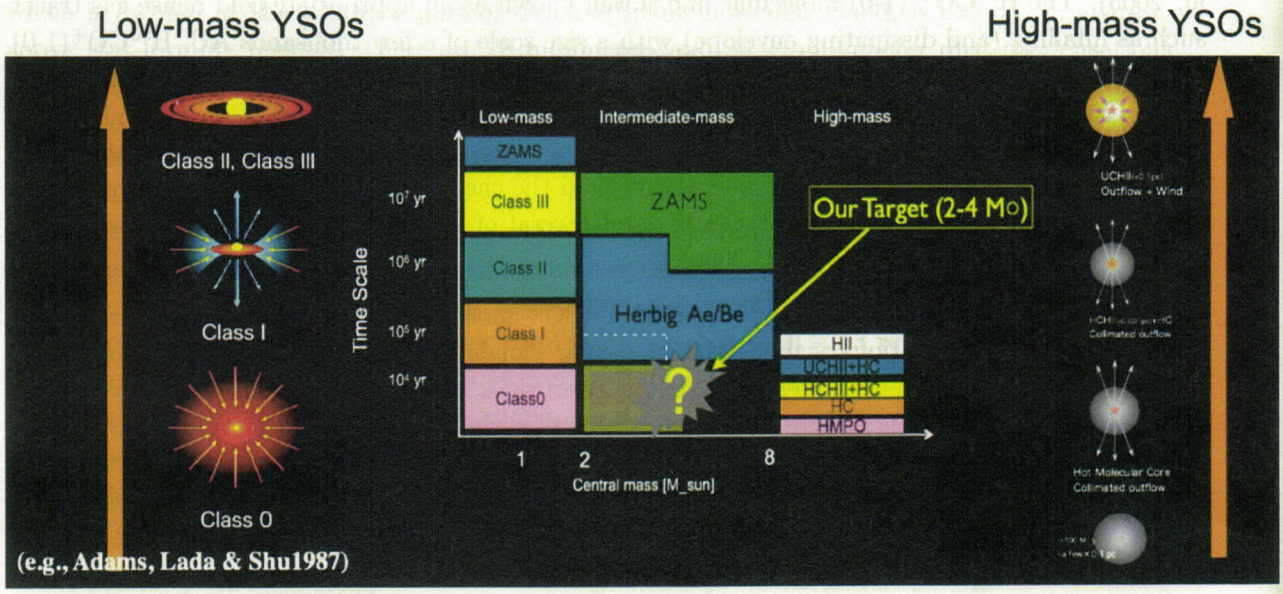

Fig. 1.— Schematic picture of the evolutionary sequence between low and high-mass YSOs referred from e.g., Adams, Lada, & Shu 1987 and Beuther et al. 2007. Vertical and abscissa axes show the age and mass of YSOs, respectively.

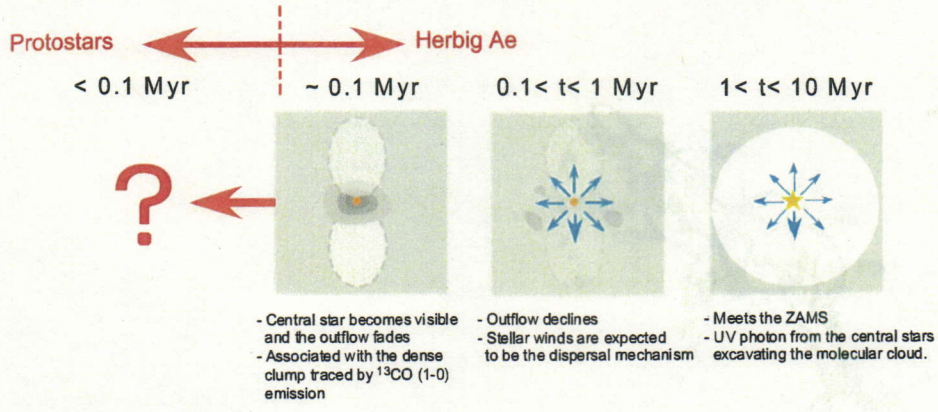

Fig. 2.— Schematic picture of mass dissipation processes toward Herbig Ae stars proposed by Fuente et al.

Table 1. Source List

Object name	RA. (J2000.0)	Dec. (J2000.0)	$F_{1.3mm(peak)}$ (mJy)	350 μm	IRAS	2MASS	3.6 cm	H_2
			OMC-3					
SIMBA *a*	05 35 30.2	-04 58 48.0	570	CSO 1	—	—	—	—
MMS 1	05 35 18.0	-05 00 19.8	347	CSO 5	—	—	—	—
MMS 2	05 35 18.3	-05 00 34.8	249	CSO 6	—	2062	VLA 1	flow B
MMS 3	05 35 19.2	-05 00 51.2	152	CSO 7	—	—	—	—
MMS 4	05 35 20.5	-05 00 53.0	354	CSO 8	—	—	—	—
MMS 5	05 35 22.4	-05 01 14.1	400	CSO 9	—	—	—	flow C
MMS 6	05 35 23.5	-05 01 32.2	2000	CSO 10	—	—	VLA 3	flow A
MMS 7	05 35 26.4	-05 03 53.4	360	CSO 12	05329-0505	2006	VLA 4	flow F
MMS 8	05 35 26.5	-05 05 17.4	268	CSO 13	—	—	—	—
MMS 9	05 35 26.0	-05 05 42.4	412	CSO 14	—	—	VLA 5	flow H
MMS 10	05 35 32.3	-05 05 41.8	166	—	—	—	—	—
			OMC-3					
FIR 1*c*	05 35 24.6	-05 07 53.3	180	CSO 16	05329-0508	1954	—	—
FIR 1*b*	05 35 23.4	-05 07 32.2	195	CSO 17	—	—	—	—
FIR 1*a*	05 35 23.7	-05 07 10.2	393	CSO 18	—	—	VLA 8	—
FIR 2	05 35 24.3	-05 08 33.3	340	CSO 20	—	—	—	flow O
FIR 3	05 35 27.5	-05 09 32.5	676	CSO 22	—	1886	VLA 11	flow J
FIR 4	05 35 26.7	-05 10 00.4	1252	CSO 23	—	1876	VLA 12	—
FIR 5	05 35 26.4	-05 10 23.4	452	CSO 24	05329-0512	1862	—	—
FIR 6*a*	05 35 23.4	-05 12 36.2	361	CSO 28	—	—	—	—
FIR 6*b*	05 35 23.4	-05 12 03.2	300	CSO 25	—	—	—	flow L
FIR 6*c*	05 35 21.5	-05 13 15.1	450	CSO 29	—	—	—	—
FIR 6*d*	05 35 20.0	-05 13 14.9	314	CSO 30	—	1796	—	—

References. — (1) Chini et al. 1997; (2) Lis et al. 1998; (3) Reipurth et al. 1999;(4) Nielbock et al. 2002.

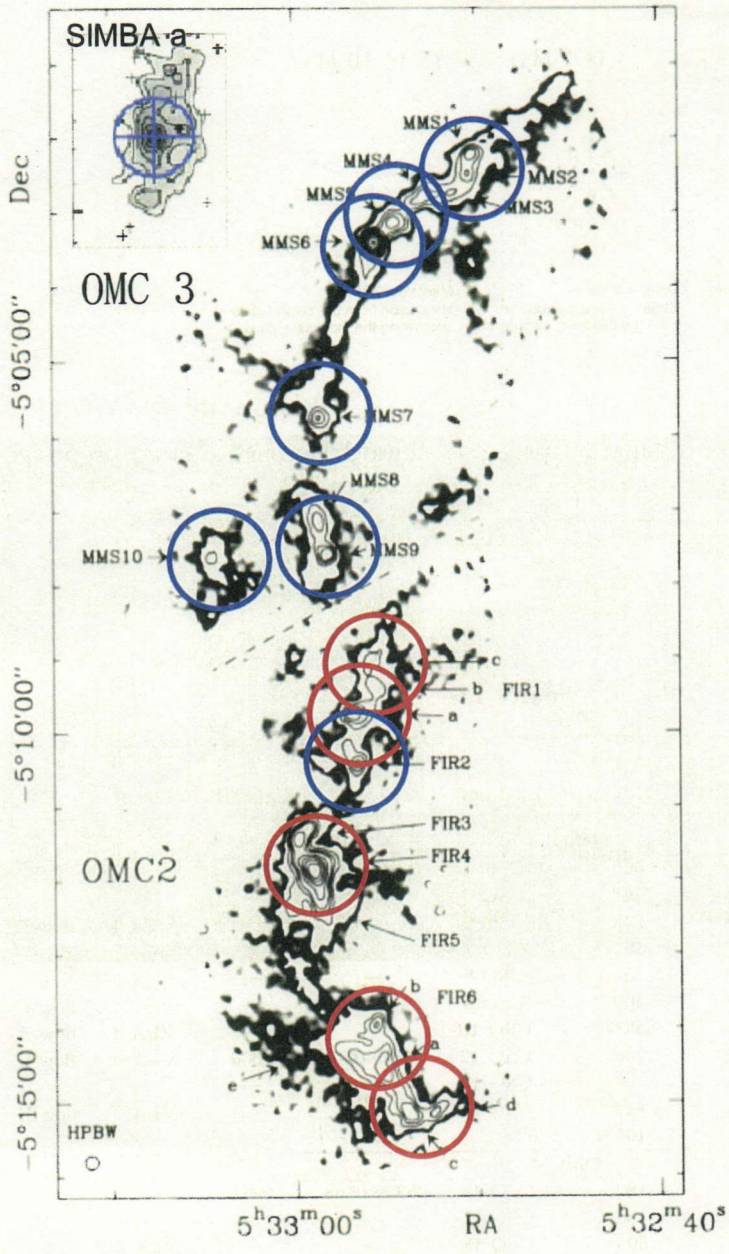

Fig. 3.— A 1300 m map of the OMC-2 and OMC-3 region in Orion referred from Chini et al. (1997) in B1950. The faintest emission, between 25 and 100 mJy, is shown in gray scale, followed by contours, which are 100 – 400 in steps of 100, 600 –1200 in steps of 200, and 1600 and 2000 mJy. The rms noise in the map is 25 mJy per 11″ beam. The left bottom circle shows one of the 11″ beams of the MPIR 19-channel bolometer array. The NMA field center is denoted by blue and red circles. Since the sources with red circles have been observed by the other collaborator, in this thesis the author only demonstrates the data of the eight field of views denoted by the blue circles.

Table 2. Properties of 1.3 mm Cores

Object	$L_{\rm bol}$ ($L_\odot$)	$L_{\rm smm}$ ($L_\odot$)	$L_{\rm bol}/L_{\rm smm}$	T_d (K)	M_{gas} $M_\odot$
		OMC-3			
SIMBA *a*	—	0.30	—	11	24
MMS 1	< 55	0.90	< 61	20-25	18
MMS 4	< 56	0.78	< 72	20-25	11
MMS 6	< 60	1.21	< 50	15-25	36
MMS 7	76	0.59	129	26	8
MMS 8	< 89	0.50	< 178	20	9
MMS 9	< 94	0.65	< 145	20	10
		OMC-2			
FIR 1*c*	128	0.36	356	33	5
FIR 1*a*	< 138	—	—	—	—
FIR 2	< 157	0.49	< 327	20	8

References. — (1) Chini et al. 1997; (2) Lis et al. 1998; (3) Reipurth et al. 1999;(4) Nielbock et al. 2002.

Chapter II

Dispersing and Rotating Core around an Intermediate-mass Protostar MMS 7 in the OMC-2/3 region

This chapter have accepted to The Astrophysical Journal as,
Millimeter- and Submillimeter-Wave Observations of the OMC-2/3 Region;
I. Dispersing and Rotating Core around an Intermediate-mass Protostar MMS 7
co-authored by
Ryohei Kawabe, Masao Saito, Shigehisa Takakuwa (NAOJ)

ABSTRACT

We report results of $H^{13}CO^+$(1–0), CO(1–0), and 3.3 mm dust continuum observations toward one of the strongest mm-wave sources in OMC-3, MMS 7, with the Nobeyama Millimeter Array (NMA) and the Nobeyama 45 m telescope. With the NMA, we detected centrally-condensed 3.3 mm dust-continuum emission which coincides with the MIR source and the free-free jet. Our $H^{13}CO^+$ observations revealed a disk-like envelope around MMS 7, whose size and mass are 0.15 × 0.11 pc and 5.1 $M_\odot$, respectively. The outer portion of the disk-like envelope has a fan-shaped structure which delineates the rim of the observed CO outflow. The position-velocity diagrams in the $H^{13}CO^+$ (1–0) emission show that the velocity field in the disk-like envelope is composed of a dispersing gas motion and a possible rigid-like rotation. The mass dispersing rate is estimated to be 3.4×10^{-5} $M_\odot$ yr^{-1}, which implies that MMS 7 has an ability to disperse ~10 $M_\odot$ during the protostellar evolutionary time. The specific angular momentum in the disk-like envelope is nearly two orders of magnitude larger than that in low-mass cores. The turn-over point of the power law of the angular momentum distribution in the disk-like envelope ($\leq$ 0.007 pc), which is likely to be related to the outer radius of the central mass accretion, is similar to the size of the 3.3 mm dust condensation. We propose that the MMS 7 is in the last stage of the main accretion phase and that the substantial portion of the outer gas has already been dispersed, while the mass accretion may still be on-going at the innermost region traced by the dusty condensation.

1. Introduction

Particularly, it is important to verify the mechanisms and the differences of the destruction or dissipation of the natal dense cores between intermediate- and low-mass star formation, because these phenomena are related to the termination of the mass accretion which determines the final mass of the central star (Nakano et al. 1995). A key to these questions is investigation of structures and kinematics of dense cores around intermediate-mass protostars. For these purposes, we have been conducting survey observations toward protostellar cores in the Orion Molecular Cloud -2 and -3 region (OMC-2/3), relatively close (d = 450 pc; Genzel and Stutzki 1989) and the most representative intermediate-mass star-forming region. We, here, report the results of one of the typical intermediate-mass protostars, MMS 7 in OMC-3, in the $H^{13}CO^+$(1–0), ^{12}CO(1–0) and 3.3 mm continuum emission with the Nobeyama Millimeter Array (NMA) and the Nobeyama 45 m telescope. The $H^{13}CO^+$ (1–0) molecular line is one of the most appropriate tracers of dense gas, which has a high critical density ($n_{\rm crit} \sim 10^5$ cm^{-3}) and is usually detected toward low- to intermediate-mass protostellar envelopes (Takakuwa et al. 2000, Saito et al. 2001, Fuente et al. 2005).

MMS 7 is one of the Class 0 candidates identified by the 1.3 mm continuum observations toward OMC-3 (Chini et al. 1997). This object is also identified as CSO 12 by the 350 μm continuum observations (Lis et al. 1998) and is associated with the IRAS point source 05329-0508. The dust mass derived from the 1.3 mm continuum emission and the bolometric luminosity are 8 $M_\odot$ and 76 $L_\odot$, respectively (Chini et al. 1997). This bolometric luminosity corresponds to ~ 3 $M_\odot$ or a A0 star at the ZAMS. Dense molecular gas around MMS 7 is also detected by

$H^{13}CO^+$(1–0) observations (Aso et al. 2000). MMS 7 is also associated with a bright reflection nebula, Haro-5a/6a (Haro et al. 1953), and 2MASS and mid-infrared sources are located at the root of the eastern reflection nebula (Nielbock et al. 2003). At MMS 7, a giant molecular outflow (0.86 pc; Aso et al. 2000) is also observed along the east-west direction, and 2.12 μm H_2 v=1-0 $S(1)$ knots are detected up to 1.45 pc to the western side (Yu et al. 1997, Stanke et al. 2002). In addition, there is a 3.6 cm continuum source elongated along the large-scale outflow, which traces a free-free jet from the protostar. The relative isolation of MMS 7 along with the above properties makes this source one of the most appropriate objects to investigate detailed spatial and velocity structures of a dense core around an intermediate-mass protostar.

2. Observations and Data Reduction

2.1. NMA Observations

We have observed $H^{13}CO^+$ (J=1–0; 86.754 GHz) and CO (J=1–0; 115.271 GHz) lines in MMS 7 with the six-elements NMA from 2004 November to 2005 March. Detailed NMA observational parameters are summarized in Table 1. Since the minimum projected baseline lengths of the $H^{13}CO^+$(1–0) and CO(1–0) observations were 2.9 and 6.3 kλ, our observations were insensitive to structures more extended than 57″ (0.13 pc) and 32″ (0.07 pc) at the 10 % level, respectively (Wilner and Welch 1994). The overall flux uncertainty was estimated to be $\sim$ 15 percent. After the calibrations, we made final images only from the data taken under good weather conditions. We have CLEANed images with a natural weighting by using Astronomical Image Processing System (AIPS) developed at NRAO * .

The 3.3 mm continuum data with the D, C, and AB configurations was obtained simultaneously with the $H^{13}CO^+$ data by using a digital spectral correlator UWBC (Okumura et al. 2000), which has 128 frequency channels and a 1024 MHz bandwidth per baseline. Both the lower (87 $\pm$ 0.512 GHz) and upper (99 $\pm$ 0.512 GHz) sidebands were obtained simultaneously with a phase-switching technique. To obtain a higher signal-to-noise ratio, the data of both sidebands were added (effective frequency = 92 GHz). We have CLEANed the continuum data with a uniform weighting (see Table 2 and Section 3.1).

2.2. 45 m Observations and Combining with the NMA Data

Single-dish mapping observations of MMS 7 in the $H^{13}CO^+$ (1–0) line were also conducted with the 5×5 SIS array receiver BEARS equipped in the 45-m telescope on 2005 April. At 87 GHz, the half-power beamwidth (HPBW) and the main-beam efficiency of the 45 m antenna were 18″.5 and 0.5, respectively. We observed the 190″ × 190″ area (corresponding to 0.43 pc×0.43 pc) centered on the NMA field center with a grid spacing of 8″.2. The temperature scale was determined by a chopper-wheel method, which provides us the antenna temperature corrected for the atmospheric attenuation. As a backend, we used an auto correlator with a frequency resolution of 31.12 kHz, corresponding to 0.11 km s^{-1} at the $H^{13}CO^+$ frequency. We applied scaling factors

*NRAO is facility of the National Science Foundation operated under cooperative agreement by Associated Universities, Inc.

to correct for variations of the gain and the DSB ratio in each beam, which were measured by the Nobeyama Radio Observatory and the typical value was ~1.5. The typical system noise temperature in DSB mode was 240 K at the elevation of 70°. The typical noise level was 0.1 K in T_A^*. The telescope pointing was checked every ~ 90 minutes by five-point cross scans in the SiO(v=1,J=1–0) maser emission from Orion KL [RA. = 5 h 35 m 14.5 s Dec = -05 d 22 m 30.4 s (J2000)] using the 40-GHz SIS receiver. The pointing error ranged from 1″ to 5 ″ during the observing run.

After the calibrations of the 45 m and NMA data, we combined each data set in the $H^{13}CO^+$(1–0) line using MIRIAD (we followed the instruction presented by Takakuwa et al. 2003a) to fill the missing short-spacing information of the interferometric data from the single-dish data and to obtain more feasible images. Our data taken with the 45 m telescope and the NMA show a discrepancy of the amplitude scale at the overlapping uv distance (2.8 - 6.2 kλ). In order to compensate this discrepancy, we multiply the 45 m amplitude by a scaling factor of 1.4, which was derived from the amplitude of these uv data at the overlapping uv distance. We consider that causes of the discrepancy are the degradation of the main-beam efficiency under windy conditions and the uncertainty of the DSB ratio of BEARS. We have CLEANed the combined images by uniform weighting. The combined synthesized beam has a size of 5″.81 × 3″.95 (2600×1800 AU) with a position angle of -24.26 °. Figure 1 compares the integrated intensity maps created with the 45m data (middle), NMA data (bottom left) and the combined map (bottom right). By combining the single-dish and the interferometric data, we succeeded to remove deep negative bowls seen in the NMA map (bottom left) and recover extended emission in the dense-gas filament, which is important to discuss the spatial and velocity structure without any problem of missing fluxes.

3. Results

3.1. Millimeter Continuum Images of the Inner Dusty Condensation

Figure 2 shows the 3.3 mm continuum emission observed with the NMA (white contours) superposed on the 2MASS K's-band image. Different NMA maps in Figure 2 were made from different sets of the visibility data whose parameters are listed in Table 2. We have detected the intense 3.3 mm continuum emission toward MMS 7. Although the peak position of the 3.3 mm source appears to be shifted from the 1.3 mm emission peak by 2.7″ (Chini et al. 1997; See Figure 2), the positions of these two sources are consistent within the expected positional error of the 1.3 mm observations (±5″) (Chini et al. 1997). The 3.3 mm source is located at the root of the K's reflection nebula and also coincides with the 8 and 24 μm compact source observed with *SPITZER/IRAC* and the 3.6 cm ionized jet (Reipurth et al. 1999, Reipurth 2004) and therefore, this source is considered to be a deeply embedded protostar.

On the assumption that the dust emission is optically thin at 3.3 mm and the distribution of the dust temperature is uniform, we can estimate the mass of the dusty condensation by

$$M_{\rm dust} = \frac{F_\lambda d^2}{\kappa_\lambda B_\lambda(T_{\rm dust})}, \qquad \text{(II.1)}$$

where κ_λ is a mass-absorption coefficient of dust grains, $B_\lambda(T)$ is a Planck function, F_λ is a total flux density of the continuum emission and d is a distance to MMS 7 (450 pc; Genzel

and Stutzki 1989). The total flux of the 3.3 mm continuum emission, 23.82 mJy, includes the contribution from the free-free jet. On the assumption that the spectral index of the free-free jet is ~0.6 (Anglada et al. 1998, Reynolds, S.P. 1986), the expected flux density of the free-free emission at 3.3 mm becomes 2.47 mJy based on the 3.6 cm flux density of 0.59 mJy (Reipurth et al. 1999). Thus, the flux density attributed to the dust emission is 21.35 mJy at 3.3 mm. Adopting the dust opacity of $\kappa_\lambda = 0.037$ cm^{2}g^{-1} $(\lambda/400\mu\mathrm{m})^\beta$ (Ohashi et al. 1996), $\beta = 1.0$ which is calculated from the 1.3 mm and 3.3 mm total fluxes and $T_{\mathrm{dust}} = 26$ - 50 K (Chini et al. 1997, Johnstone et al. 2003), we estimate the mass of the dusty condensation to be 0.36 - 0.72 $M_\odot$.

Figure 2*c* was made only from the visibility data taken at > 30 kλ (See Table 2). In the higher resolution image, we see an elongated structure along the NE-SW direction. This NE-SW elongation may imply the presence of a binary with a separation of $\sim$ 1″.9 (corresponds to 830 AU). However, there is no infrared or cm counterpart toward the extension of the 3.3 mm emission, and more plausible interpretation is that the faint continuum feature traces the hot and dense region heated by the associated outflow, since the direction of the elongation of the 3.3 mm emission is similar to the direction of the 3.6 cm fine-scale jet.

3.2. Bipolar Outflow associated with MMS 7

Figure 3*a* shows the distribution of the blueshifted (V_{LSR}=7.0 to 8.7 km s^{-1}) and redshifted (V_{LSR}=12.1 to 13.8 km s^{-1}) ^{12}CO(1–0) emission in MMS 7 superposed on the 2MASS K's-band image. Here, we adopt the systemic velocity of 10.6 km s^{-1} obtained from the single-dish H^{13}CO$^+$(1–0) spectrum. The outflow is elongated along the east-west direction and roughly aligned with the direction of the free-free jet (Reipurth et al. 1999). Both the blue- and red-shifted components are seen at the east and west side of MMS 7, which suggests that the axis of the bipolar outflow is near the plane of the sky. Furthermore, the outflow shows an asymmetric structure with the stronger red- and blue-shifted components at the eastern side.

Figure 4 shows velocity channel maps in the ^{12}CO(1–0) emission with a velocity interval of 0.6 km s^{-1}. The red-shifted component in the velocity range of V_{LSR}=11.6 to 13.3 km s^{-1} was already detected with the BIMA and the FCRAO 14 m telescope (Williams et al. 2003). The distribution of this component is consistent with that found by their observations. We have newly detected other components in the velocity range from V_{LSR}=7.6 to 11.0 km s^{-1}. High-velocity blue-shifted components in the velocity range of V_{LSR}=7.6 to 8.7 km s^{-1} are seen at the eastern side of MMS 7. Particularly, the strong and compact CO component is evident at the position of the K's-band nebula which is most likely illuminated by MMS 7. The strong blueshifted and redshifted components are only seen at the eastern side. These results suggest that the ^{12}CO(1–0) bipolar outflow is slightly inclined from the plane of the sky and the western components are hidden by the disk-like envelope, i.e. the eastern blue-shifted components is located near-side. This is supported by the fan-shaped brighter reflection nebula at the eastern side than that at the western side (See Figure 1). Figure 5 shows the distribution of the high-velocity ^{12}CO(3–2) emission observed with the ASTE telescope (Atacama Submillimeter Telescope Experiment). The large-scale outflow ($\sim$1 pc) also has the same configuration as that of the small-scale outflow observed with the NMA in the ^{12}CO(1–0) emission, i.e. the blue lobe is located at the eastern side and the red lobe at the western side. The detailed interpretation of the CO(3–2) outflow taken with the ASTE telescope will be the subject to the forthcoming paper.

3.3. $H^{13}CO^+(J=1–0)$ emission

Both the Single-dish (Figure 1*a*) and interferometric (Figure 1*b*) maps in the $H^{13}CO^+$(1–0) emission show an fan-shaped structure, which is approximately perpendicular to the associated bipolar outflow, and is also seen in the single-dish 1.3 mm and 350 μm continuum emission (Chini et al. 1997, Lis et al. 1998). The interferometric image, Figure 1*b*, shows an elongated disk-like envelope associated with MMS 7 (we use the term "disk-like envelope" as the compact structure detected with the NMA). The size of the disk-like envelope is estimated to be 30000×21000 AU (0.15×0.11 pc). The combined image, Figure 1*c*, reveals that the disk-like envelope observed with the NMA is embedded in the extended dense gas halo observed with the 45 m telescope.

Figure 3*b* and *c* compare the morphology of the disk-like envelope to that of the 2 μm and 8 μm emission, respectively. The distribution of the extended near- and mid-infrared emission seems to be anti-correlated with that of the disk-like envelope. Particularly, the local emission maximum in the disk-like envelope correspond to the local minimum in the 8 μm map and vice versa. The central point source in the 8 μm emission, which coincides with the 3.3 mm point source and therefore the protostellar source of MMS 7, is not located at the peak of the disk-like envelope and is shifted to the eastern side (see Figure 3*c*). One interpretation to explain this offset is that the warm and dense dusty condensation in the vicinity of the protostar does not reside at the peak of the molecular column density traced by the $H^{13}CO^+$ emission.

Table 3 summarizes physical properties of dense gas around MMS 7 derived from the 45m and NMA combined data. Assuming that the $H^{13}CO^+$ emission is optically thin and the distribution of the excitation temperature is uniform, we estimated the LTE mass as follows,

$$M_{\rm LTE}\ [{\rm M}_\odot] = 2.03{\times}10^{-2} \left(\frac{26\ {\rm K}}{T_{\rm ex}}\right) \exp\left(\frac{4.16}{T_{\rm ex}}\right) \frac{\tau}{1-\exp(-\tau)} \left(\frac{\rm d}{450\ {\rm pc}}\right)^2 \left(\frac{1.4{\times}10^{-10}}{X({\rm H^{13}CO^+})}\right) \int {\rm F}_\nu {\rm dv}\ [{\rm Jy\ km\ s^{-1}}], \quad \text{(II.2)}$$

We adopt $T_{\rm ex}$ =26-50 K (Chini et al. 1997, Johnstone et al. 2003), and X [$H^{13}CO^+$] $\sim 1.4{\times}10^{-10}$ derived from the comparison of the estimated $H^{13}CO^+$ column density and the $C^{18}O$ column density (Chini et al. 1997).

Figure 6 shows NMA velocity channel maps in the $H^{13}CO^+$ (1-0) emission at a velocity interval of 0.26 km s^{-1}. The blue-shifted emission, $V_{\rm LSR}$=9.3 – 9.8 km s^{-1}, is seen at the south-western part of the 3 mm dust peak. Close to the systemic velocity of $V_{\rm LSR}$=10.6 km s^{-1}, the peak position of the blue-shifted emission shifts from south-west to west. The red-shifted emission, $V_{\rm LSR}$=10.8 – 11.5 km s^{-1}, is seen at the northern part of the 3 mm dust peak. This velocity gradient along the major axis of the disk-like envelope implies the rotational motion. We also note the velocity gradient along the minor axis, i.e. the strong blue-shifted component in the velocity range of $V_{\rm LSR}$=10.2 – 10.4 km s^{-1} is located at the western part of the protostar, while there appears weak red-shifted extension in the velocity range of $V_{\rm LSR}$=10.6 – 11.3 km s^{-1} at the eastern side of the protostar. The fan-shaped structure in the total integrated intensity map of Figure1*b* is also confirmed in the velocity channel maps in the range of $V_{\rm LSR}$ = 10.2 – 10.4 and 10.8 – 11.3 km s^{-1}.

3.4. Another YSO candidate; MMS 7-NE

We have also detected a weak 3.3 mm continuum source at 3.8 σ level toward $\sim$ 40″ northeast of MMS 7 (see Figure 2*a*; hereafter we call this component MMS 7-NE). The peak position and

the total 3.3 mm flux of this source are estimated to be RA= $05^h35^m28.2^s$, Dec= -05°03′41.1″ (J2000) and 6.81 mJy, respectively, from the 2-dimensional Gaussian fitting to the image. This source is also seen as a point source in the K's image, and 8μm and 24μm sources taken with the *SPITZER/IRAC* (see Figure 3). This source was also detected to be a very compact 350 μm dust component by Lis et al. (1988) with CSO, which locates at the southeast of CSO 11, although they did not identify this object. The 3.3 mm continuum flux corresponds to 0.04 – 0.30 $M_\odot$ † assuming $\beta = 0 - 1$, $T_{\rm dust}$ = 20 K and gas-to-dust ratio of 100.

MMS 7-NE is associated with the weak $H^{13}CO^+$ emission (Figure 1*b*, *c* or Figure 3). The ^{12}CO emission is also seen toward MMS 7-NE (see Figure 4 in the range of $V_{\rm LSR}$ = 8.2 to 10.4 km s^{-1}), implying the association of the molecular outflow. We note that MMS 7-NE has a smaller scale (10^4 AU scale) outflow, suggesting that it has little influence to destruct the MMS 7 disk-like envelope.

MMS 7-NE is likely to be a more evolved protostar than MMS 7, because there is a diffraction ring in the 8 μm image which suggests the presence of point source (i.e. no scattering material) and a K's-band counterpart of this source. Alternatively, the circumstellar material around MMS 7-NE has already been swept up by the outflow from MMS 7, revealing the central stellar object of MMS 7-NE.

4. Discussion

Our new observations in the $H^{13}CO^+$ line have revealed systematic velocity structures in the disk-like envelope around the intermediate-mass protostar of MMS 7. In the subsequent sections, we will discuss the gas kinematics in the disk-like envelope and the difference from that in low-mass counterparts using position-velocity (P-V) diagrams.

4.1. Radial Velocity Structure of the Disk-like Envelope

4.1.1. P-V diagram

We show a P-V diagram along the minor axis of the disk-like envelope in Figure 7*b*. In the P-V diagram, there are at least two components; one is an eastern component at the velocity range of $V_{\rm LSR}$=10.7 to 11.5 km s^{-1} ((i) in Figure 7*b*) and the other western-component at the velocity of $V_{\rm LSR}$=9.6 to 10.9 km s^{-1}. The western component is associated with the 3 mm dust continuum emission (vertical solid line in Figure 7b). In this component, "X-shape" velocity structures are discerned in the P-V diagram. One of the X-shaped velocity structures as indicated by (ii) in Figure 7*b* shows blue-shifted emission ($V_{\rm LSR}$=9.6 to 10.0 km s^{-1}) at the west of the protostar and red-shifted emission ($V_{\rm LSR}$=10.6 to 10.9 km s^{-1}) at the east of the protostar. The sense of this

†No cm source was detected toward this source in the cm observations by Reipurth et al. (1999). Thus, we estimated the upper limit of the possible contribution from the free-free emission at 3.3 mm. Given the rms noise level of 40 μJy, the 3 sigma upper limit of the 3.6 cm total flux (3 sigma level) is 0.12 mJy. Thus, if we assume the spectral index of 0.6, the contribution from the free-free emission at 3.3 mm is 0.49 mJy, which is less than 5% of the total flux of the 3.3 mm continuum emission at MMS 7-NE (6.81 mJy). We can probably ignore the possible contribution.

velocity structure is opposite to that of the associated molecular outflow. On the assumption that the $H^{13}CO^+$ emission traces the flattened disk-like envelope which is perpendicular to the associated outflow, this velocity structure can be interpreted as an expanding motion in the flattened disk (e.g. Kitamura et al. 1996). The other velocity structure in the X-shape, with two components at the velocity range of V_{LSR}=9.9 to 10.4 km s^{-1} (blueshifted; (iii)-1 in Figure 7*b*) and V_{LSR}=10.5 to 11.0 km s^{-1} (redshifted; (iii)-2 in Figure 7*b*), has the same velocity sense as that of the associated outflow. These two components are located outside the central condensed gas, suggesting that these components are not associated with the central protostar. Thus, it is natural to interpret that these gas components trace swept-up dense gas by the associated outflow perpendicular to the disk-like envelope. A similar example has also been reported from observations in L1228 (Taffala et al. 1994). They detected a velocity shift in the high-density tracer of the C_3H_2 (2_{12} - 1_{01}) emission, which has the same velocity sense as that of the associated CO bipolar outflow, and they interpreted this shift as an interaction between the dense core and the high-velocity outflow. The eastern component, indicated by (i) in Figure 7, is located at 25″ east of the continuum peak position and is a part of the fan-shaped structure seen in the combined total intensity map. We interpret that this component is remnant dense gas interacting with the associated molecular outflow.

In summary, the P-V diagram can be interpreted as a mixture of the dispersing gas along the disk-like envelope and the interacting dense gas with the associated outflow perpendicularly to the disk-like envelope. Presumably due to the insufficient spatial resolution, an infall gas motion in the protostellar source of MMS 7 has not been clearly identified in our observations.

4.1.2. Properties of the Dispersing Disk

The velocity structure of the disk-like envelope shows a dispersing gas motion as discussed in the last section. The virial mass of the disk-like envelope is estimated to be 23-30 $M_\odot$ assuming D_{env} = 0.15 pc, T_{env} = 26 - 50 K, and Δv = 1.0 km s^{-1}, which is larger than the LTE mass of the disk-like envelope (5.1 - 9.1 $M_\odot$). This result suggests that the disk-like envelope is gravitationally unbound, supporting our interpretation of the dispersing gas motion. We can estimate physical parameters of the dispersing motion, such as an expanding velocity (V_{exp}), momentum (P_{exp}), expanding energy (E_{exp}), and mechanical power (L_{exp}), as $V_{exp}(\equiv V_{max})$ = 1.2 km s^{-1}, $P_{exp} = MV_{max}$ $M_\odot$km s^{-1} , $E_{exp} = MV_{max}^2/2$ $M_\odot$km^2 s^{-2}, and $L_{exp} = MV_{max}^3/2R$ $L_\odot$. We adopt the disk inclination angle from the plane of the sky to be $i \sim 80°$, which is consistent with the morphology of the CO outflow and the reflection nebula. Table 4 lists the estimated physical parameters of the dispersing motion. The dispersing envelope has also been observed in the ^{13}CO(1-0) emission around a low-mass YSO of DG Tau (Kitamura et al. 1996). We compare physical parameters specified in the dispersing process of MMS 7 to those of DG Tau in Table 4. These parameters of MMS 7 are two orders of magnitude larger than those in DG Tau. The interferometric observations of DG tau may suffer from the problem of the missing flux, which prevents us from making a direct comparison of these parameters. However, even if the interferometric observations recover only 10 % of the total flux from DG Tau, these parameters of MMS 7 are still one order of magnitude larger than those in DG Tau. These results suggest that the intermediate-mass protostar of MMS 7 has more active dispersing processes than low-mass counterparts.

There are recent studies on the dispersing gas motion around Herbig Ae/Be stars (Fuente

et al. 2002). Their studies show that intermediate-mass stars disperse $\gtrsim$ 90 % of the total mass of the parent core during the protostellar phase. Particularly, these objects which have a spectral type later than B6 evolve with the substantial dispersing material, 3 - 80 $M_{\odot}$, in the protostellar phase. We, here, define the mass-dispersing rate (mass loss rate) which is $\dot{M}_{\rm out} \sim M_{\rm env} \cdot V_{\rm exp}/R_{\rm env} = (3.4 - 6.0) \times 10^{-5}$ $M_{\odot}$ yr^{-1} . This value implies that MMS 7 has an ability to disperse a mass of 0.9-1.5 $M_{\odot}$ during the outflow dynamical time scale of 2.5×10^4 yr, which is estimated from the ASTE data. We speculate that the intermediate-mass protostar of MMS 7 will keep dispersing substantial circumstellar material during the protostellar phase and will eventually be a Herbig Ae star in $\tau \leq$ a few$\times 10^5$ yr, as proposed by Fuente et al. (2002).

4.1.3. Driving Mechanisms of the Dispersing Disk

What is the mechanism of the dispersing process in the disk-like envelope ? One of the probable candidates is the associated bipolar outflow, which is blowing away the material along the outflow axis and at the surface of the disk-like envelope. There is a twisting structure near the center of the reflection nebula Haro-5a/6a in the K's-band seen in Figure 3, and several knots (at least three components) in the red-shifted CO(3-2) emission in Figure 5 (a),(b) denoted by the dashed-blue line. The connected trajectory of those emission peaks shows a wiggled structure. These results suggest that the precessing bipolar outflow from MMS 7 is able to destruct the surface of the disk-like envelope in the east-west direction with a wide opening angle. The importance of bipolar outflows in the dispersal of ambient gas around low-mass protostars has already been pointed out by previous studies (Ohashi et al. 1997, Velusamy & Langer 1998, Takakuwa et al. 2003b). Takakuwa et al. (2003b) has reported a dispersing low-mass protostellar core around IRAM 04191+1522. The detected blueshifted CH_3OH components (see BLUE1 and BLUE2 of Figure 3 in Takakuwa et al. 2003b) are most likely to be formed in consequence of the interaction between the outflow and the ambient dense gas surrounding the protostar and pushed away from the natal cloud core.

In addition, there is a possibility that the stellar wind from the central protostar mainly contributes to the dispersion along the direction which is perpendicular to the outflow. A low-velocity wind ($\sim$100 km s^{-1}) with a wide opening angle, ($\sim$100°) is detected toward a low-mass protostar L1551 IRS 5 (Pyo et al. 2002, Pyo et al. 2005). There are also studies on the stellar wind around Herbig Ae/Be stars, which show the derived mass-loss rate in the ionized gas $\sim 10^{-8}$ - 10^{-7} $M_{\odot}$ yr^{-1} (e.g. Skinner et al. 1994). Therefore, it is possible that the stellar wind from MMS 7 drives the mass dispersion with the estimated rate of (3.4 - 6.0)$\times 10^{-5}$ $M_{\odot}$ yr^{-1}. In fact, the bolometric power of MMS 7 is 76 $L_{\odot}$, much larger than the mechanical luminosity of the dispersing motion, $L_{\rm exp} = (4.2 - 7.4) \times 10^{-3}$ $L_{\odot}$ (see Table 4), and is energetically sufficient to drive the expanding motion.

4.2. Rotating Envelope

The P-V diagram along the major axis in Figure 7*c* shows that the velocity of the disk-like envelope increases with distance up to 5200 AU from the center. One of the possible (and simple) interpretations of this velocity gradient is rigid rotation in the disk-like envelope, although, it is difficult to clearly discern it owing to the mixture of the kinematics of the filament/core/envelope.

Assuming the disk inclination of 80° and the radius of 5200 AU, the timescale of the rigid rotation in this flattened disk is estimated to be 1.5×10^5 yr, which is much longer than the outflow dynamical time scale of 2.5×10^4 yr.

Red and blue plots in Figure 8 show the local specific angular momentum in the disk-like envelope as a function of the radius around MMS 7. Our data demonstrate the angular momentum distribution on a size scale of $0.007 - 0.02$ pc (corresponding to 1500 - 4700 AU) inside the single source. For comparison, we also plot the angular momentum of low-mass dense cores and circumstellar disks (Ohashi et al. 1997b, Goodman et al. 1993). The value of the specific angular momentum around the MMS 7 is nearly two orders of magnitude larger than that of the low-mass counterparts at the same size scale. The specific angular momentum distribution of the disk-like envelope around MMS 7 has a power-law index of ~ 1.8 which is closer to the index of rigid rotation, that is, 2.0. On the other hand, the specific angular momenta of low-mass NH_3 cores observed by Goodman et al. (1993) are fitted by a power-law index of ~ 1.6 as indicated by a dashed line in Figure 8. Furthermore, we note that there is no clear turn-over point of the power-law in the plot of MMS 7 as the low-mass case, which suggests that the turn-over point is smaller than that of low-mass NH_3 cores (~ 0.03 pc) and is smaller than 0.007 pc, on the assumption that the value of the specific angular momentum at the innermost part of MMS 7 is the same as that of the low-mass value. The turn over point of the power law indicates the minimum size of the rotation where the specific angular momentum is not constant as a function of radius. At the dynamical collapsing region, the specific angular momentum should be constant in the entire radius. Therefore, the turn-over point can be considered as a starting point of the dynamical collapse toward the central protostar (Ohashi et al. 1997b). From these considerations, we suggest that the infalling radius in MMS 7 is smaller than that of low-mass counterparts. If dynamical collapse in MMS 7, if any, follows the inside-out collapse model (Shu et al. 1977), the smaller infalling radius implies that the period passed after the accretion started is shorter than that of low-mass cores (a few $\times 10^5$ yr).

4.3. Evolutionary Stage of the Intermediate-mass Protostar MMS 7

The disk-like envelope, with the fan-shaped structure and the expanding motion around MMS 7, has a larger dispersing activity than that of low-mass cores (see section 4.1). MMS 7 has a large-scale ($\sim$1 pc) active CO outflow (Figure 5) which has a dynamical time scale of $\tau_{\rm dyn} \sim 2.5 \times 10^4$ yr. These observational results suggest the presence of the significant mass-loss activity in the intermediate-mass protostar of MMS 7. Then, is there any mass supply onto the central star from the surrounding gas around MMS 7 ? In this subsection, we will discuss a possibility of the presence of mass accretion and the evolutionary stage of MMS 7.

Although an infall motion is not clearly seen in our $H^{13}CO^+$ observations, the presence of the molecular outflow implies the existence of the mass accretion toward MMS 7 (Bontemps et al. 1996). To make a 3 $M_\odot$ protostar of MMS 7, a large accretion rate ($\dot{M} \sim 1.2 \times 10^{-4}$ $M_\odot$ yr^{-1}) is required over the outflow dynamical time (we, here, assume that $\tau_{\rm dyn} \sim \tau_*$ and constant $\dot{M}$). We found the smaller turn-over radius of the specific angular momentum distribution, which implies that the radius of the infalling region, ≤ 0.007 pc (1500 AU), is smaller than low-mass counterparts. The size of the dusty condensation around MMS 7, 1500 $\times$ 1200 AU, is similar to the inferred radius of the infalling region. Thus, it is possible that inside the dusty condensation, where the present spatial resolution is not high enough to trace the internal velocity structure,

there is a substantial material which is accreting onto the central protostar. These considerations suggest that the intermediate-mass protostar MMS 7 is formed with higher mass-accretion and mass-loss rates than those of low-mass counterparts.

The small infalling radius if present, short dynamical time of the outflow, and the presence of substantial circumstellar material, could imply that MMS 7 is in the early evolutionary phase. On the other hand, our observational results show the energetic dispersing activity. Therefore, the early phase intermediate-mass protostar MMS 7 is already dispersing the surrounding envelope. Future interferometric observations with higher spatial resolution is required to investigate details of the innermost accreting region around MMS 7.

5. Summary

We have carried out $H^{13}CO^+$ (1–0), CO (1–0) and 3.3 mm dust-continuum observations toward the intermediate-mass protostar of MMS 7 in OMC-3 with the NMA and the NRO 45 m telescope. Figure 9 shows the schematic picture of MMS 7 region and the main results are summarized as follows:

1. We detected a centrally-condensed 3.3 mm continuum source which is consistent with the 1.3 mm and SPITZER source. The size and mass of the centrally-condensed component are 1500 × 1200 AU (P.A. $\sim$ 170°) and 0.36 - 0.72 $M_\odot$, respectively. This 3.3 mm source is most likely to be an associated dusty condensation around the intermediate-mass protostar of MMS 7. We have also identified a new 3.3 mm continuum source, MMS 7-NE, whose mass is estimated to be 0.04 - 0.30 $M_\odot$.
2. The $H^{13}CO^+$ emission is distributed surrounding the 3.3 mm dust-continuum emission and has fan-shaped structure at the rim of the the bipolar outflow, suggesting the presence of the interacting region. Our combined 45 m and NMA data have revealed a disk-like envelope inside the dense $H^{13}CO^+$ core. The size and the mass of the disk-like envelope are 0.5 × 0.11 pc (P.A. $\sim$ 0°) and 5.1 - 9.1 $M_\odot$ (for T_{ex} = 26 - 50 K), respectively.
3. We found that the disk-like envelope around MMS 7 is being dispersed. The momentum, expanding energy, and mechanical power of the dispersing envelope are much larger than those of low-mass dispersing envelopes. The disk-like envelope has a quite large mass-dispersing rate of (3.4 - 6.0) × 10^{-5} $M_\odot$ yr^{-1} and this result implies that MMS 7 has an ability to disperse the substantial mass ($\sim$ 10 $M_\odot$) during the protostellar evolutionary phase ($\sim$ a few×10^5 yr). The mechanism of the dispersing gas motion is considered to be the effect of the associated CO bipolar outflow and the stellar wind from the protostar.
4. We also detected a velocity gradient in the disk-like envelope from an P-V diagram along the major axis. The specific angular momentum inside the disk-like envelope is nearly two orders of magnitude larger than that in low-mass NH_3 cores at same size scale. The power-law index of the angular momentum distribution inside the envelope is estimated to be 1.8, which is closer to the index of a rigid rotation (= 2.0). In addition, we note that a turn-over point of the power-law in the disk-like envelope is $\leq$ 0.007 pc. This result suggests that the infalling radius is smaller than 0.007 pc, which is similar to the size of the 3.3 mm dust condensation. The presence of the significant mass-loss activity (dispersing envelope and molecular outflow) implies the presence of the mass supply onto the central star from the surrounding gas around

MMS 7, i.e. MMS 7 is formed with the higher mass-accretion and mass-loss rate that those of low-mass counterparts.

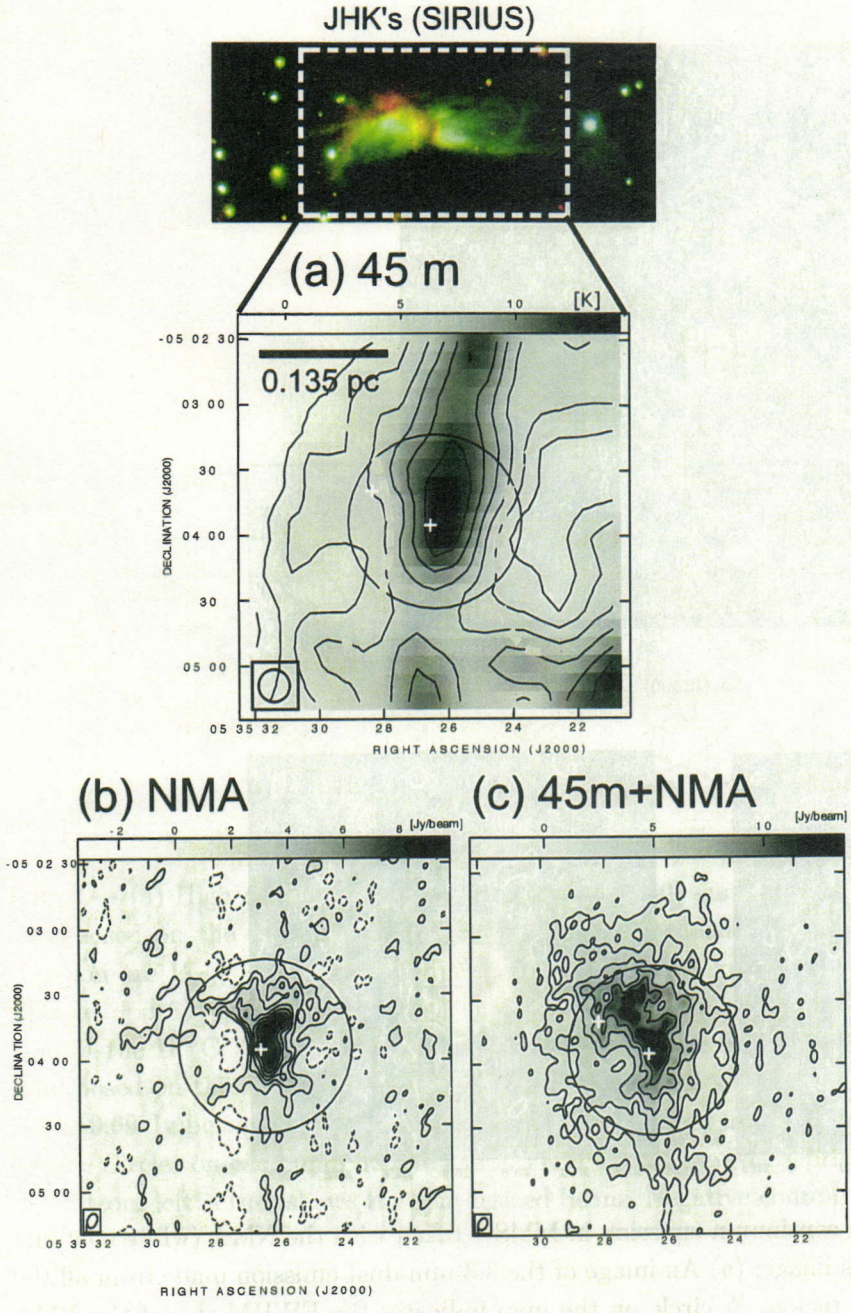

Fig. 1.— Top pannel shows a JHK's composite image taken by SIRIUS/IRSF, and bottom images show $H^{13}CO^+$(1–0) integrated intensity maps of MMS 7 in the velocity range of V_{LSR} = 9.3 to 11.9 km s^{-1} made from (a):the 45 m data (contour levels = 4.8, 9.6, 14.4, 19.2, 24.0 and 28.8 K km s^{-1}), (b):the NMA data (contour levels = ± 7.7, 15.4, 23.1, 30.8, 38.5, 46.2 and 53.9 K km s^{-1}) and (c):combined map of the 45 m and the NMA data (contour levels = ± 12.9, 25.8, 38.7, 51.6, 64.5, 77,4 and 90.3 K km s^{-1}), respectively. Negative contours are drawn in dashed lines. Open ellipse at the bottom left corner in each map is the synthesized beam (HPBW). Circles on the maps show the FWHM size of the NMA primary beam. Crosses in each map represent the 3.3 mm dust continuum peak positions (see Figure 2) observed with the NMA.

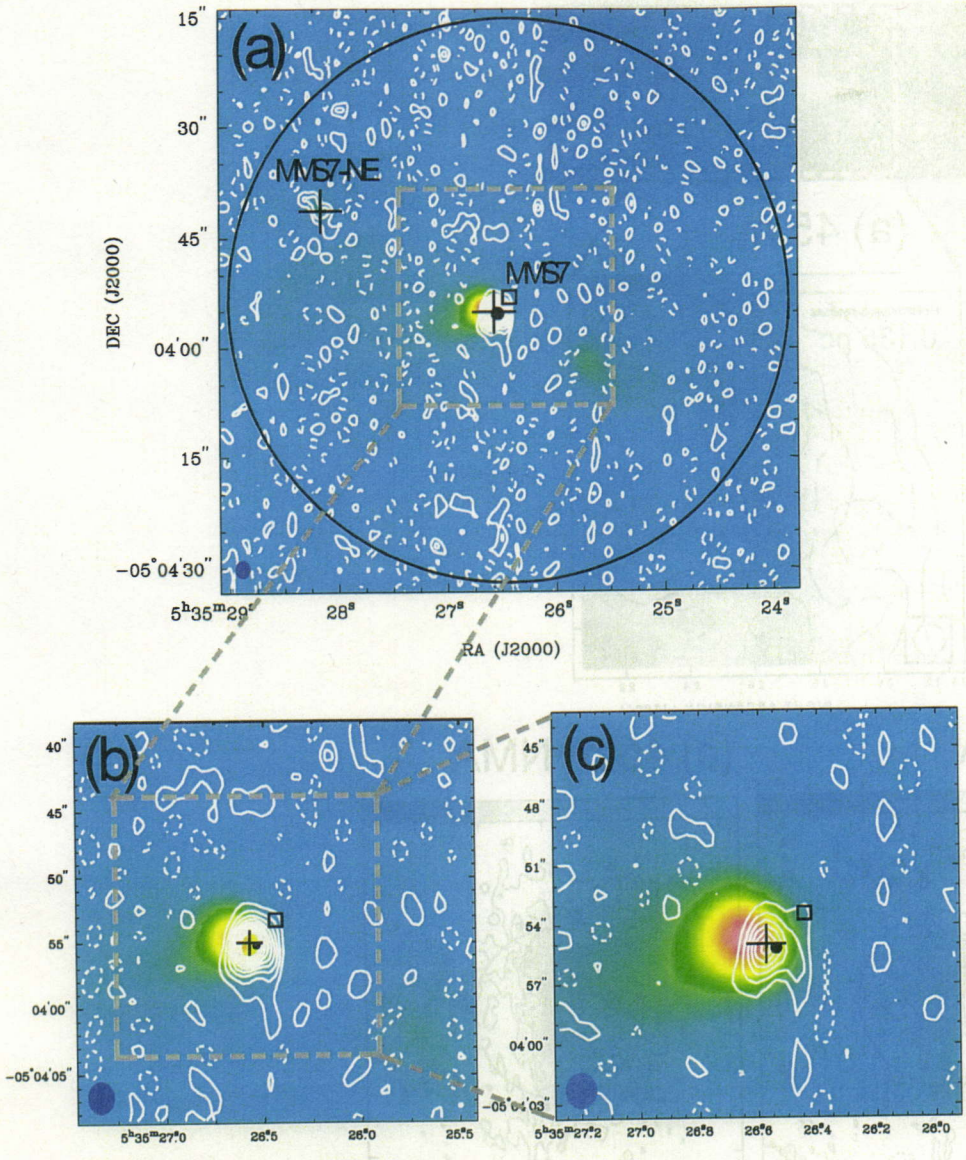

Fig. 2.— Maps of the 3.3 mm continuum emission in MMS 7 taken with the NMA (white contour) superposed on the 2MASS K's image; (a) An image of the 3.3 mm dust emission made from all the *uv* data in the entire MMS 7 region. A circle on the map indicates the FWHM size of the NMA primary beam at 86 GHz; (b) A close-up view of (a) at the center of MMS 7; and (c) the map made only from the visibility data with the projected *uv* distance larger than 30 kλ. Uniform weighting was applied in making all the maps. Contour levels start at $\pm 1.5\sigma$ levels with intervals of 1.5σ (1σ = 0.84 and 1.30 mJy beam^{-1} for (a) and (b), respectively). Negative contours are drawn by dashed lines. The open square in each map show positions of the 1.3 mm emission peak identified by Chini et al. 1997. The central and north-eastern cross indicates positions of 8 and 24 μm sources (from the SPITZER/IRAC archive data). A filled circle in each map indicates the position of the 3.6 cm source (Reipurth et al. 1999).

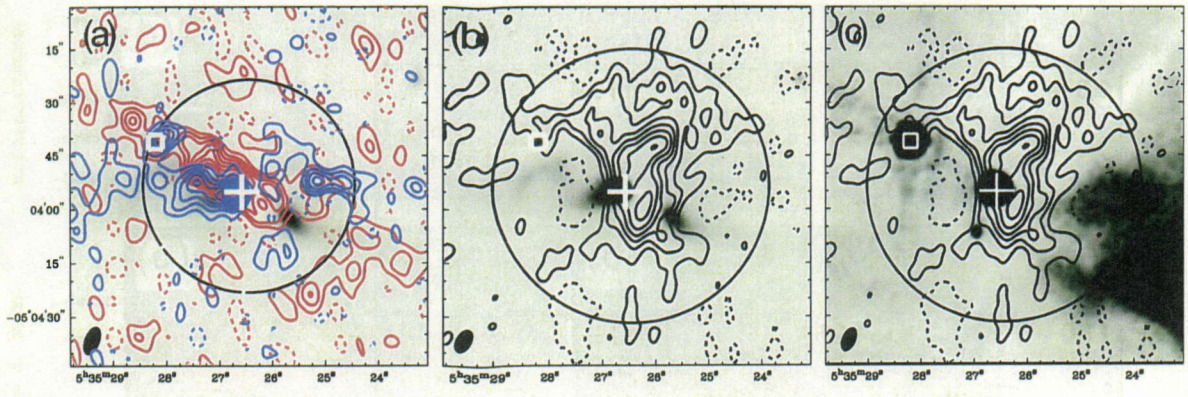

Fig. 3.— (a) High velocity components of the CO(1-0) emission in contour taken with the NMA superposed on the 2MASS K's in gray-scale. The velocity ranges of the blue- and red-shifted emission are $V_{\rm LSR}$ = 7.0 to 8.7 km s^{-1} and 12.1 to 13.8 km s^{-1}, respectively. The contour lines start at $\pm$ 1.5σ levels with intervals of 1.5σ. (1σ = 0.48 Jy beam^{-1}). (b) NMA total intensity map of the H^{13}CO$^+$(1-0) emission in contour integrated from $V_{\rm LSR}$ = 9.3 to 11.9 km s^{-1} range superposed on the 2MASS K's image. The contour lines start at $\pm$2σ levels with intervals of 2σ. (1σ = 0.69 Jy beam^{-1}). (c) The same H^{13}CO$^+$(1-0) maps is superposed on the mid-infrared 8 μm image. Circles on each map denote the FWHM size of the NMA primary beam. A filled ellipse at the bottom-left corner shows the synthesized beam. Negative contours are drawn by dashed lines.

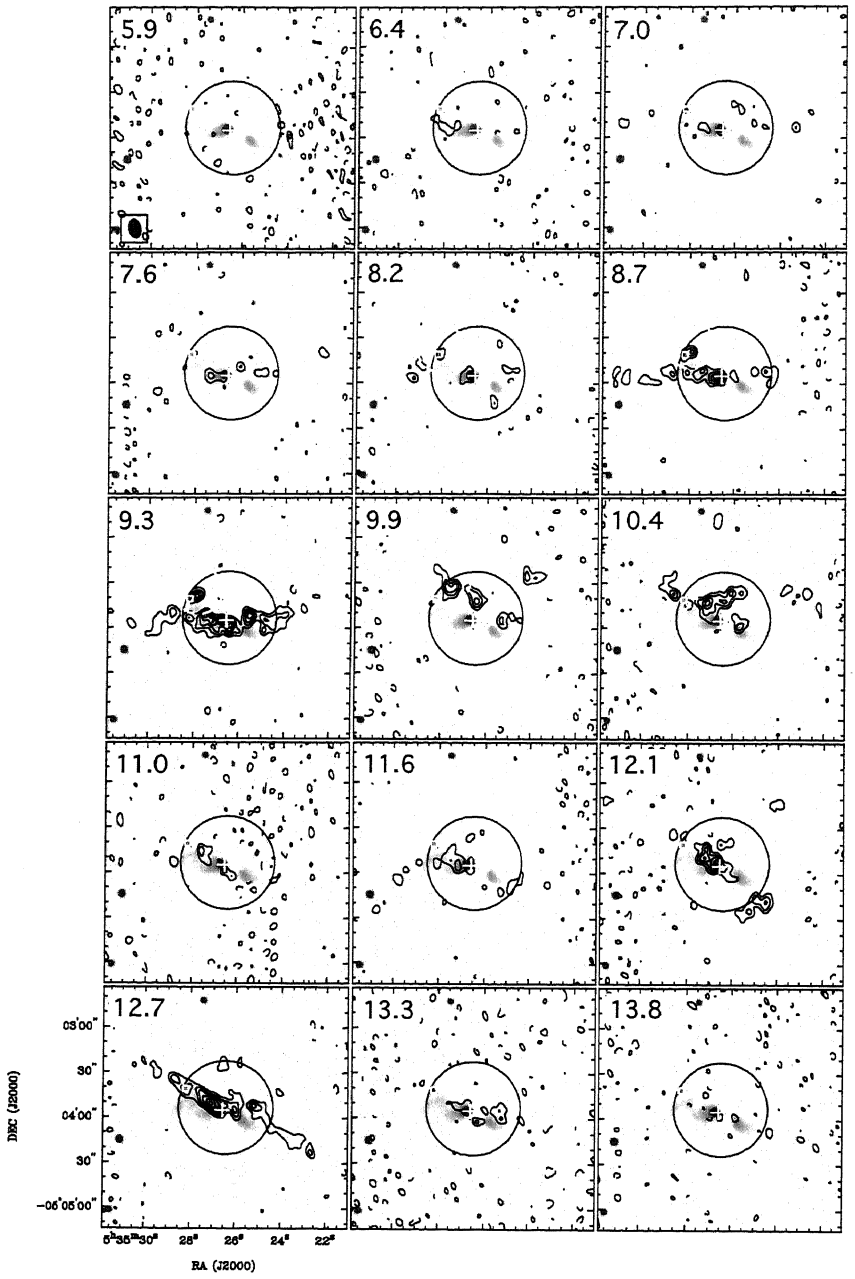

Fig. 4.— Velocity channel maps of the ^{12}CO(1-0) emission with the NMA in contour superposed on the 2MASS K's-band image in gray scale. The central LSR velocity in the unit of km s^{-1} is noted at the upper left corner of each panel. The contour lines start at $\pm$ 2σ levels with intervals of 2σ. (1σ = 0.24 Jy beam^{-1}). Circles on the maps show the NMA primary beam. A filled ellipse at the bottom-left corner indicates the synthesized beam. A cross(center) and an open box (north -west) indicate the position of 3.3 mm dust continuum, 8 μm and 24 μm mid infrared source, i.e. the positions of MMS 7 and MMS 7-NE, respectively. The emission from MMS 7-NE is indicated by a white dashed circle. Negative contours are drawn by black dashed lines.

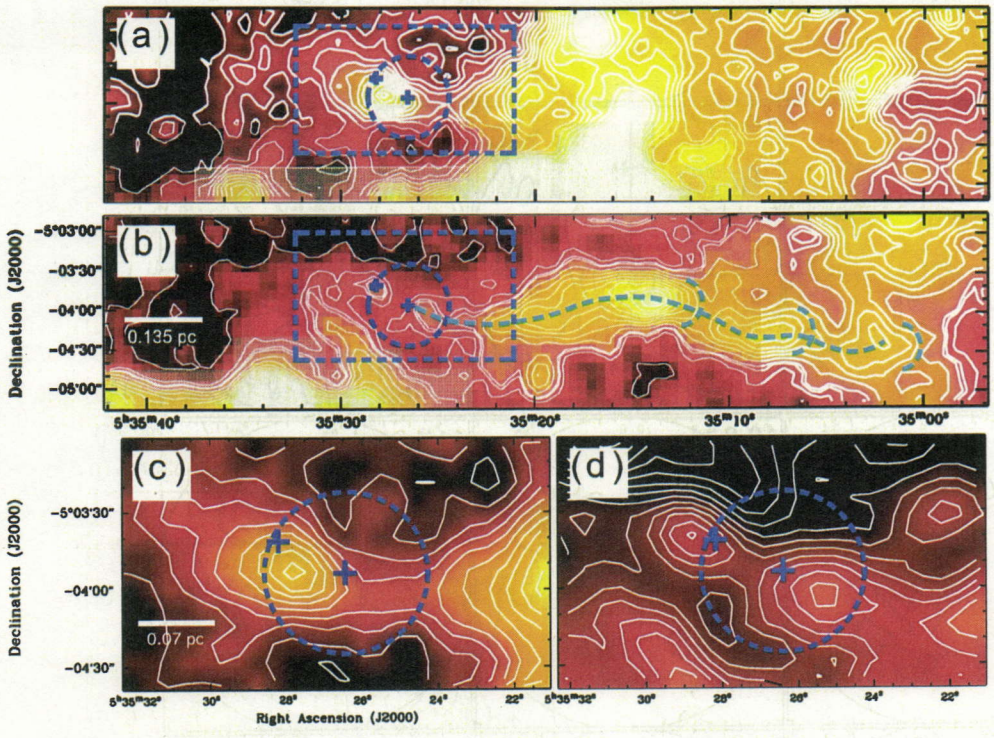

Fig. 5.— ^{12}CO(3-2) high-velocity blue and red-shifted emission taken with the ASTE telescope. (a) Blue shifted image in the velocity range of 4.6 $\leq$ $V_{\rm LSR}$ $\leq$ 8.9 kms^{-1} (b) Red shifted image in the velocity range of 13.2 $\leq$ $V_{\rm LSR}$ $\leq$ 17.5 kms^{-1}. (c) Blue shifted image in the velocity range of 6.7 $\leq$ $V_{\rm LSR}$ $\leq$ 8.9 kms^{-1}. (d) Red shifted image in the velocity range of 12.1 $\leq$ $V_{\rm LSR}$ $\leq$ 13.2 kms^{-1}. The velocity range of (c) and (d) are same as that of the CO(1–0) maps in Figure 3(a). A circle on the maps and o is the NMA primary beam. An open square in (a) and (b) are the mapping area of (c) and (d). Crosses indicate the position of the 3.3 mm dust emission detected with the NMA (i.e. the position of MMS 7 and MMS 7-NE, respectively). The hatched regions show the bipolar outflow from the source, MMS 9, located at south of MMS 7. Detailed description of the ASTE observations will be in the forthcoming paper. This figure was made using the KARMA software package (Goch 1995).

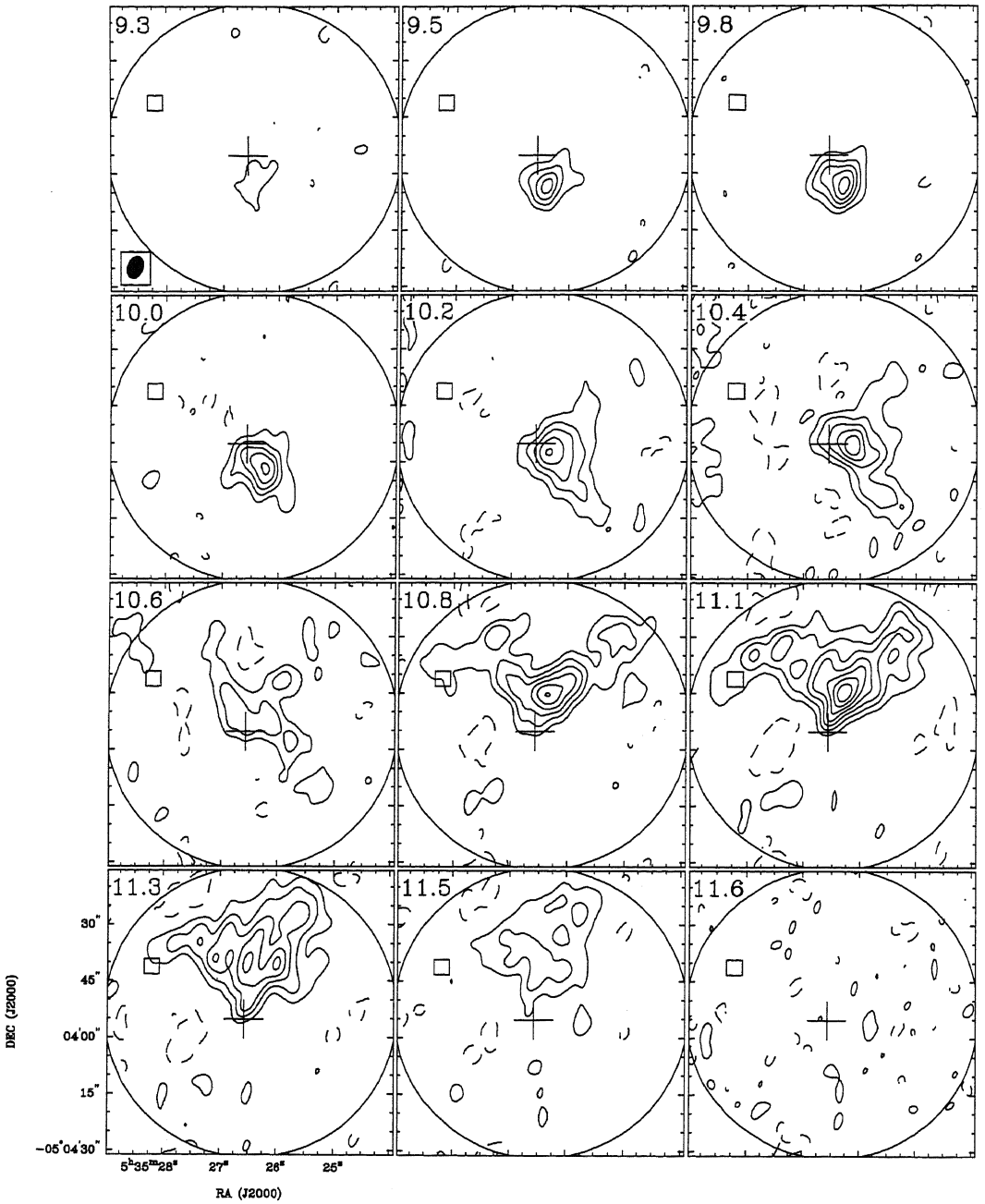

Fig. 6.— $H^{13}CO^+$(1-0) channel maps taken with the NMA. The central LSR velocity in the unit of km s^{-1} is noted at the upper left corner of each panel. The contour lines start at 2σ levels with intervals of 2σ (1σ = 0.1 Jy $beam^{-1}$). The open circles on the maps show the FWHM size of the primary beam. The filled ellipse at the bottom left-hand corner indicates the synthesized beam. The cross (center) and open box (north -west direction) indicate the position of 3.3 mm dust continuum, 8 μm and 24 μm mid infrared source, i.e. the positions of MMS 7 and MMS 7-NE, respectively.

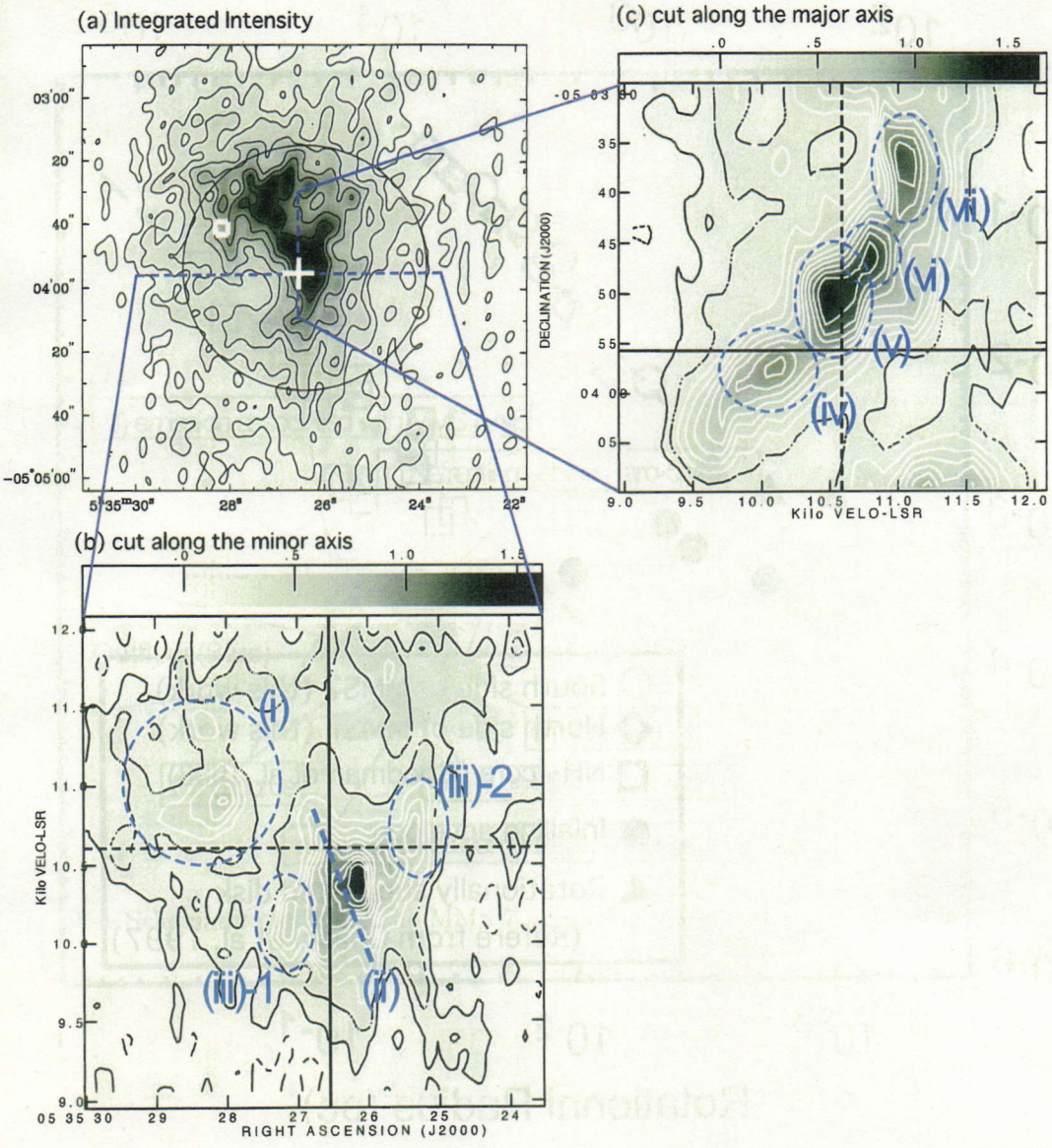

Fig. 7.— (a) Map of integrated intensity in $H^{13}CO^+$ with a velocity range of V_{LSR} = 9.3 to 11.9 km s^{-1}. (b)$H^{13}CO^+$(1-0) position-velocity maps cut along the minor axis (P.A.= 0°) and (c)major axis (P.A.= 90°) of the flattened disk. ! ! Solid lines and dashed lines in (a) and (b) are systemic velocity and position of 3.3 mm continuum peak (i.e. the position of protostar).

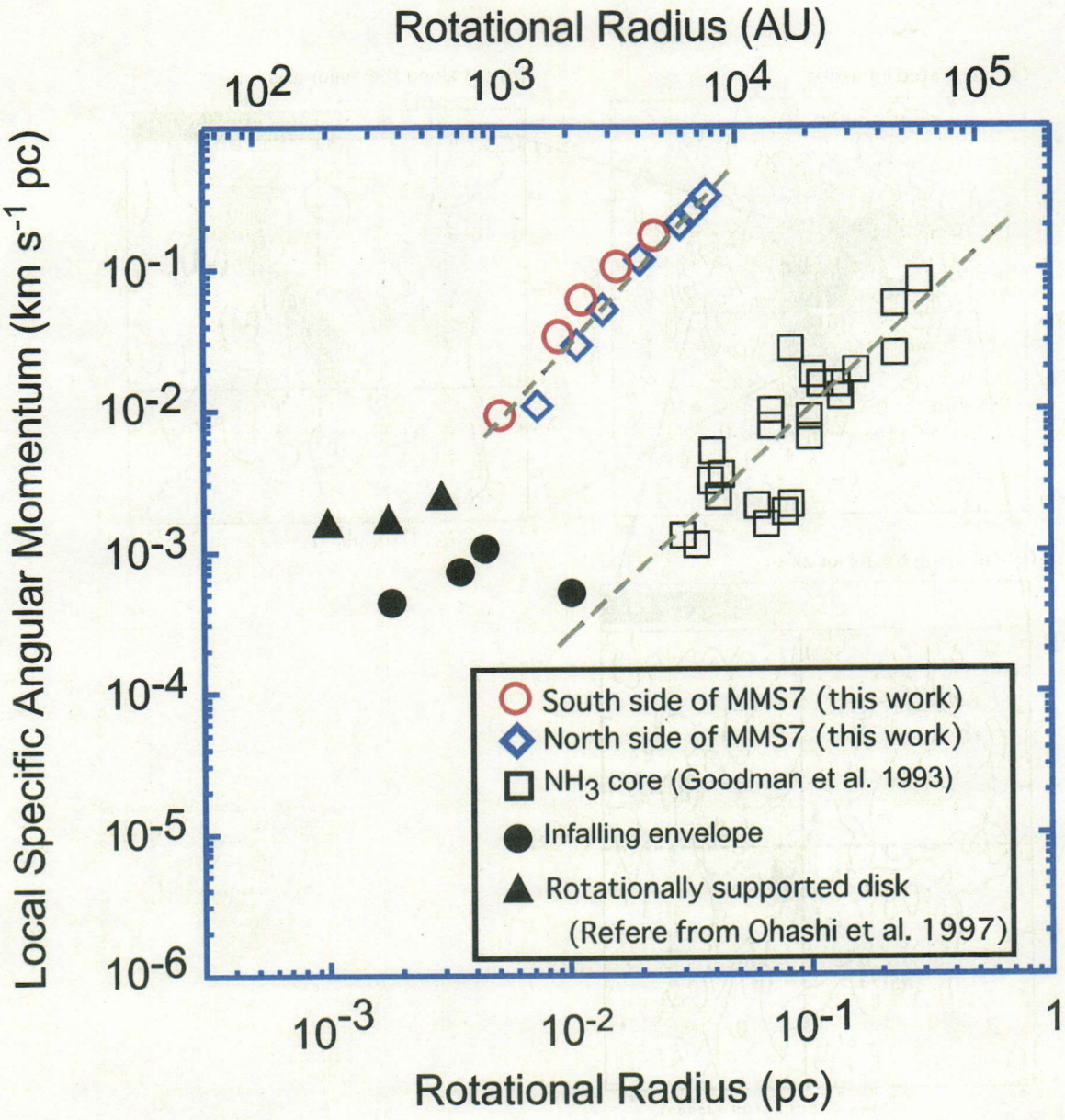

Fig. 8.— Local specific angular momentum in the MMS 7 flattened disk plotted as a function of the radius (red open circles and blue open squares). Open squares, filled circles, and filled triangles represent data from NH_3 cores (Goodman et al. 1993), infalling envelopes and rotationally supported disks in the Taurus (Ohashi et al. 1997), respectively. The dashed lines show power-law fittings with an index of 1.6 to the results of NH_3 cores in low-mass stars and an index of 1.9 to the results of the $H^{13}CO^+$ disk-like envelope in MMS 7, respectively.

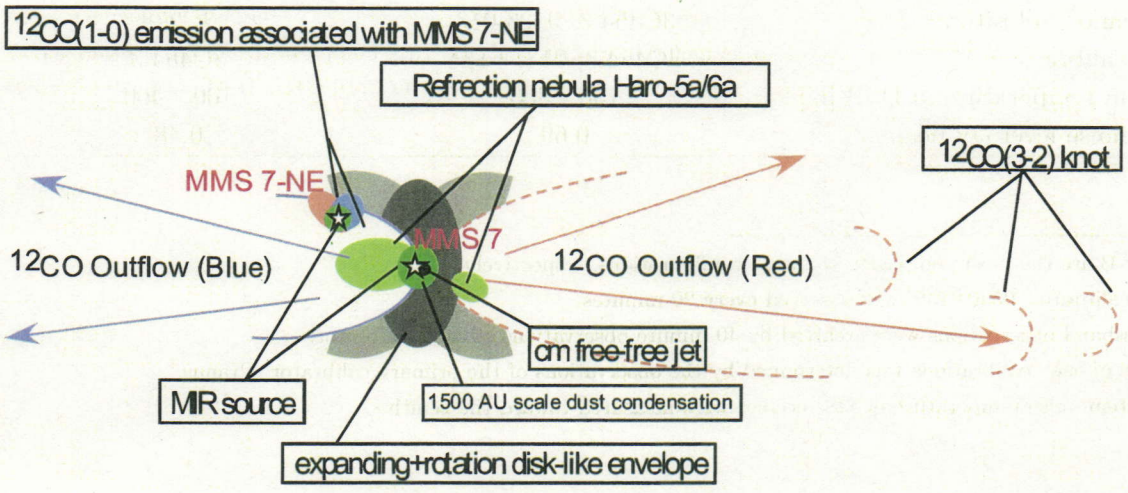

Fig. 9.— Schematic picture of the MMS 7 and MMS 7-NE region

Table 1: Parameters for the NMA Observations

	Molecular Line	
Parameter	$H^{13}CO^+$(1–0)	CO(1–0)
Configuration [a]	D, C and AB	D
Baseline [kλ]	2.9 – 115	6.3 – 27.4
Phase reference center (J2000)	R.A. = 05^h 35^m 26.4^s, Dec = -05° 03′ 53.4″	
Primary beam HPWB [arcsec]	77″	62″
Synthesized Beam HPBW [arcsec]	6″.77 × 4″.33 (P.A.=-21°.35)	6″.04 × 4″.74 (P.A.=-11°.42)
Velocity resotion [km s^{-1}]	0.11 km s^{-1}	0.08 km s^{-1}
Band width [MHz]	32	
Gain calibrator [b]	0531+135	
Passband calibrator [c]	3C454.3, 0423-013	3C273
Flux calibrator [d]	3C454.3, 0531+134	3C454.3
System temperature in DSB [K] [e]	150 - 300	100 - 400
Rms noise level [Jy beam^{-1}]	0.69	0.48

[a] D and AB are the most compact and sparse configurations, respectively.

[b] A gain calibrator, 0530+135, was observed every 20 minutes.

[c] The passband observations were archived by 40 minute observations of each calibrator.

[d] The flux of each calibrations was determined by the observations of the primary calibrator, Uranus.

[e] The system noise temperature of SIS receiver were measured toward the zenith.

Table 2: Parameters of the Figure 2(a),(b) and 2(c)

Parameter	Figure 2(a),(b)	Figure 2(c)
Baseline [kλ]	2.9 - 115	30 - 115
Weighting	Uniform	Uniform
Beamsize (HPBW) [arcsec]	2″.47 × 2″.04	1″.83 × 1″.60
P.A. of the beam [°]	-10.86	-1.79
Rms noise level [Jy beam^{-1}]	8.37e-04	1.23e-03
Total flux density [mJy] ($> 3\sigma$)	23.82	21.20
Deconbolution size [arcsec]	3.40(±0.185) × 2.68(±0.146)	2.86(±0.299) × 2.29(±0.239)
P.A. of the component [°]	170.621 ± 9.2	161.262 ± 18.464

Table 3: Physical Properties of the $H^{13}CO^+$ (1-0) Components

Component	Size [c] (AU)	N_{H_2} [d] ($\times 10^{22}$ cm^{-2})	M_{LTE} ($M_\odot$)
Disk-like envelope[a]	30000 × 21000	7.3 (13.0)	5.1 (9.1)[d]
MMS 7-NE[b]	2600 × 1800	2.4 (4.3)	6.6×10^{-2} (1.2×10^{-1})[e]

[a] We use a flux above 9 σ level in the 45 m and NMA combined map

[b] We assume that the $H^{13}CO^+$ gas extends similar to beamsize.

[c] Assuming that d=450 pc

[d] Derived from T_{ex} =26 K (50 K) and $X[H^{13}CO^+] = 1.4\times10^{-10}$(Chini et al. 1997, Johnstone et al. 2003)

[e] Derived from T_{ex} =20 K and $X[H^{13}CO^+] = 1.4\times10^{-10}$

Table 4: Physical Parameters of the Dispersing Core

Parameter	MMS 7[a]		DG Tau[b]
$M_{env}(M_\odot)$	5.1[c]	9.1[d]	0.03
P_{exp} ($M_\odot$ km s^{-1})	6.2	11.1	0.05
E_{exp} ($M_\odot$ km^2 s^{-2})	3.8	6.8	0.03
L_{exp} (10^{-3} $L_\odot$)	4.1	7.4	0.6

[a] Assuming that disk inclination is 80°

[b] Reffer from Kitamura et al. 1996 observed with the NMA data

[c] Derived from T_{ex} = 26 K (Chini et al. 1997)

[d] Derived from T_{ex} = 50 K (Johnstone et al. 2003)

Chapter III

Survey Observations of Large-Scale Molecular Outflows associated with Intermediate-mass Protostellar Candidates

This chapter will be submitted to The Astrophysical Journal as,

Millimeter- and Submillimeter-Wave Observations of the OMC-2/3 Region;

II. Survey Observations of Large-Scale Molecular Outflows associated with Intermediate-mass Protostellar Candidates

co-authored by

Ryohei Kawabe, Masao Saito, Shigehisa Takakuwa (NAOJ), Nobuhiko Kusakabe (SOKENDAI), Yoshito Shimajiri (Tokyo University), Motohide Tamura (NAOJ)

1. Introduction

CO molecular outflows are fairly common phenomena in star-forming regions (e.g. Arc et al. 2005, and Bachiller & Tafalla 1999 for reviews). CO outflows are considered to be directly associated with the main accretion phase in low-mass protostars, and usually adopted to identify protostars in dense cores. The geometry of the outflow is also a key to identify the near- and far-side of the flattened disk-like envelope around protostars, and hence dynamical infall toward the central protostar (e.g., L1551 IRS 5 in Ohashi et al. 1996 and Saito et al. 1996). In addition, it is important to consider the influence of outflows on natal cores. Recent works have revealed that outflows significantly interact with the natal core at the earliest evolutional stage of protostars (Takakuwa et al. 2003, Arce & Sargent 2006 in low-mass case, Takahashi et al. 2006 in intermediate-mass case). Physical nature of CO outflows has also been intensively studied so far for those associated with low-mass protostars, $\sim 1\ M_{\odot}$. In fact, the momentum rate of CO molecular outflows decreases from the Class 0 to Class I evolutional phase in the case of low-mass protostars. The interpretation is that the outflow activity reflects the corresponding decay in the mass accretion/infall rate (i.e, $F_{\rm CO} - L_{\rm bol}$ correlation; Bontemps et al. 1996). Similar correlations between the luminosity and the mechanical force (or Mass outflow rate) are also found in high-mass protostars, $M_{*} \gtrsim 8\ M_{\odot}$, (e.g. Shephard et al. 1996, Wu et al. 2005).

On the other hand, properties and evolutions of outflows associated with intermediate-mass protostar ($2 \lesssim M_{*} \lesssim 8\ M_{\odot}$), as well as their influence on the ambient gas, have not been well-understood. Then, a goal of the present study is to understand the evolution of outflow activities associated with intermediate-mass protostars. For these purposes, we have performed survey observations of outflows and jets toward one of the nearest intermediate-mass star-forming regions: the Orion Molecular Cloud -2/3 (OMC-2/3; d=450 pc; Chini et al. 1997, Genzel & Stutzki 1989). There are 28 millimeter- and 33 submillimeter dust condensations which are mostly identified as deeply embedded intermediate-mass protostars at Class 0/I phase (Chini et al. 1997, Lis et al. 1998, Nielbock et al. 2003). 3.6 cm free free-jets are also detected toward 7 of the embedded sources (Reipurth et al. 1999). Shock-excited H_2 knots, which trace a shock front of each flow, are associated with these embedded sources (Yu et al. 1997, 2000, and Stanke et al. 2002). Aso et al. (2000) and Williams et al. (2003) made mapping observations in the CO(1–0) emission and identified 9 CO outflows associated with the millimeter sources in the OMC-3 and the northern part of the OMC-2 regions.

In this chapter, we report results of our unbiased survey of molecular outflows in the submillimeter CO (3–2) emission, which selectively traces higher temperature (>33 K) regions with less contamination from cold ambient gas than that of the lower transitions, CO(1–0) and CO(2–1). We will also show results of the JHK_s deep images in OMC-2/3, which enable us to identify faint reflection nebulae, chain of knots, and optical jets. From these data, we will demonstrate structure and kinematics of outflows associated with the intermediat-mass protostars, and will discuss the properties and evolution of the outflow activities.

2. Observations and Data Reduction

2.1. CO(3–2) observations

The CO(3–2; 345.795990 GHz) data have been taken with the ASTE 10 m telescope (Atacama Submillimeter Telescope Experiment) located at the Pampa la Bola (latitude = 4800 m), Chile (Ezawa et al. 2004; Kohno et al. 2004). Observations were remotely made from an ASTE operation room at San Pedolo de Atacama, using the network observation system N-COSMOS3 developed by NAOJ (Kamazaki et al. 2005) during the period of 2005 September 2-4. The half-power beam-width of the ASTE telescope is 22″ (corresponding to 0.05 pc at a distance of the OMC-2/3 region). We used 345 GHz SIS heterodyne receiver, and the typical system noise temperature in DSB mode was 175 - 350 K, and the typical atomspheric opacity at 220 GHz was 0.05 during our observations. The temperature scale was determined by a chopper-wheel method, which provides us the antenna temperature corrected for the atmospheric attenuation. As a backend, we used four sets of 1024 channel auto correlators, which provide us a frequency resolution of 31.12 KHz, corresponding to 0.27 km s^{-1} at the CO(3–2) frequency. The On-The-Fly (OTF) mapping technique was employed to cover the whole OMC-2/3 region, 23′.0×13′.3 (corresponding to 3.1 × 1.8 pc at 450 pc). The telescope pointing was checked every two hours by 5-points scans of the point-like CO(3-2) emission from R Dor[R.A.=04^h 36^m 45.8^s, decl.=-62° 04′ 35.7″(J2000)]. The pointing errors were measured to be ranged from 1″.5 to 4″.0 during the observing run. We adopted the main beam efficiency coupled with DSB ratio of 0.55, which was measured by Sawada et al. (2007). After subtracting linear baselines, the data were convolved by a Gaussian-tapered Bessel function (Magnum, Emerson, & Greisen 2000) whose FWHM was 14″ and resampled onto a 7″ grid. Since the telescope beam is a Gaussian with a FWHM of 22 ″, the effective FWHM resolution is 26 ″. The "scanning effect" was minimized by combining scans along R.A. and decl., using the PLAIT algorithm developed by Emerson & Grave (1988). The typical rms noise level was 0.47 K in T_A^* (corresponding to 10^{-4} $M_\odot$ for one beam) with a velocity resolution of 1.08 km s^{-1}.

2.2. NIR observations

NIR images in the OMC-2/3 region were obtained on 2004 November with the near-infrared camera SIRIUS (Simultaneous Three-Color InfrarRed Imager for Unbaiased Survey) equipped in the 1.4 m Infrared Survey Facility (IRSF) telescope at South African Astronomical Observatory, in Sutherland. The camera is equipped with three 1024 × 1024 pixel HgCdTe (HAWAII) arrays. Two dichroic mirrors enable us to make simultaneous observations at the J ($\lambda_c = 1.25\mu$m), H (1.63μm), and K_s = (2.14μm) bands. Details of the camera are provided by Nagashima et al. (1999) and Nagayama et al. (2003). The image scale of the array is 0″.45 pixel^{-1}, providing a field of view of 7′.7×7′.7. Three different field centers, [1]: R.A.=5^h 35^m 22^s, decl.=-5° 00′ 14.8″, [2]: R.A.=5^h 35^m 22^s, decl.=-5° 6′ 44.9″, and [3] R.A.=5^h 35^m 22^s, decl=-5° 13′ 14.8″, were set to cover the entire OMC-2/3 region. We obtained a total exposure time of 900 seconds. Seeing conditions were ∼ 1″.0 ($FWHM$) in the J band. The limiting magunitude is 19.2 mag. at J band. We used the NOAO IRAF software package to reduce the data. We applied the standard procedures for near-infrared array image reduction, including dark current subtraction, sky subtraction, and flat-fielding (see Nakajima et al. 2005 for details of the SIRIUS image reductions).

3. RESULTS

Table 1 summarizes continuum sources in the OMC-2/3 region. We selected 43 objects associated with any of 1.3 mm- (from Chini et al. 1997 and Nielbock et al. 2003), 350 μm- (from Lis et al. 1998), or VLA-3.6 cm- sources * (from Reipurth et al. 1999) as a protostellar candidate. We note that these samples may also include starless sources. We also checked if a 24 μm source taken by SPITZER/MIPS associated with any of the 1.3 mm, 350 μm and 3.6 cm sources. Table 2 shows a summary of our outflow identification. Identification of outflows was made from analyses of CO(3–2) velocity channel maps, bipolarity (or morphology), line-profiles, and position-velocity (P-V) diagrams. We identified high-velocity blue- and red-shifted components with velocity shifts more than $\geq$ 1 km s^{-1} from the systemic velocity in each object. We additionally used our deep JHK_s images taken by IRSF/SIRIUS for the identification. The JHK_s images trace a reflection nebula and a chain of knots or jet-like features from protostars. We classified the identified outflows into three categories: "Clear", "Probable", and "Marginal" as follows;

Clear: There are "clear" bipolar collimated high-velocity components in the CO(3–2) channel maps. We also confirmed the 1.3 mm and 24 μm continuum sources at the center of the bipolarity as a driving source.

Probable: There are collimated monopolar- high-velocity components in the CO(3–2) channel maps, or possible bipolar outflows with confusion from ambient gas. We also confirmed any of 1.3 mm, 350μm, 24 μm or VLA- 3.6 cm source nearby high-velocity bipolar or monopolar collimated component.

Marginal: There is no clear evidence of collimated outflows in the channel maps. However, there is an extended NIR feature or less-collimated high-velocity CO(3–2) emission around either a 1.3 mm or 350 μm source.

Figure 1 shows distribution of the CO(3–2) high-velocity emission in OMC 2/3. We totally identified nine clear, five probable and six marginal outflows in the OMC-2/3 region. The driving sources of the nine clear outflows are SIMBA *a*, MMS 2, MMS 5, MMS 7, MMS 9, FIR 2, FIR 3, VLA 13, and FIR 6*b*. Among these, seven CO outflows associated with MMS 2, MMS 5, MMS 7, MMS 9, FIR 1, FIR 2, and FIR 3 have previously been found in CO(1–0) observations (Aso et al. 2000, Williams et al. 2003). The eight clearly and probably detected CO outflows associated with SIMBA *a*, SIMBA *c*, UD-1, VLA 9, VLA 13, FIR 6*b*, FIR 6*c*, and CSO 33 are newly identified in the present study.

Since there are 43 continuum sources as shown in Table 1, the detection rate of the associated clear and probable CO outflow is 33.3 % in the OMC-2/3 region. This result suggests that the outflow detection rate is significantly low in OMC-2/3 as compared to that in Taurus and high-mass star-forming regions, where the detection rate of the CO molecular outflow is almost 80 –100 % and 90 %, respectively (e.g. Bontemps et al. 1996, Hogerheijde et al. 1998 for low-mass case, Zhang et al. 2001 for high-mass case). However, in the case of our samples include many starless condensations. In fact, there are 18 1.3 mm and/(or) 350 μm sources (i.e., dusty condensations) without 24 μm counterparts (i.e., heating sources) in the OMC-2/3 region, which implies possible presence of prestellar dusty condensations. Furthermore, we have to consider

*We, here, selected only candidates of the free-free jets (i.e., we omitted candidates of the back ground objects from Reipurth et al. 1999).

the difference of sensitivity and contamination from ambient gas for the outflow identification, especially in the intermediate- to high-mass star-forming region. We consider that it is difficult to directly compare the detection rate in each region. In the following section, we will describe results of individual outflows.

3.1. Individual Molecular Outflows

In this section, we describe each outflow associated with the 1.3 mm continuum source. Here, we mainly use the source name based on 1.3 mm identification, If driving source has no 1.3 mm sources, we use the name based on 350 μm and/or VLA- 3.6 cm identifications.

3.1.1. SIMBA Region

Figure 2 and 3 shows two detected CO outflows in the SIMBA region. We newly detected a CO(3–2) outflow along the NE-SW direction associated with SIMBA *a* as shown in Figure 2 (*clearly identified outflow*). In SIMBA *c*, we identified CO (3–2) outflow (*probably identified outflow*). The blue-shifted components lie NW to SE direction which is also consistent with the brighter part of the NIR nebula denoted by [1] in Figure 3*a*. Although, we see a red-shifted component in the western part of SIMBA *c*, it is difficult to conclude whether this component is a part of outflow or structure of the molecular filament. In this region, we newly identified three 24 μm protostellar candidates (SP 053530-045848, 053528-045838 and 053531-045936) associated with the 1.3 mm continuum sources of SIMBA *a*, SIMBA *c* and SIMBA *e* as shown in Figure 2*b*.

3.1.2. OMC-3 Region

Figure 4 shows results of our outflow survey in the OMC-3 Region. There are 10 millimeter sources, MMS 1 to MMS 10, in this region, and at least six millimeter sources have a small ratio of $L_{bol}/L_{smm} < 200$, indicating class 0-type SEDs (Chini et al. 1997).

MMS 2; (*clear*)– We detected the CO(3–2) outflow along the east-west direction toward MMS 2 as shown in Figure 4*b*. The blue- and redshifted components are overlaid at both side, suggesting that the configuration of this flow is close to the plane of the sky. This east-west outflow has also been identified in the CO(1–0) emission (Williams et al. 2003, Aso et al. 2000). However, the previous CO(1–0) studies did not identify which sources among MMS 2 - 4 is the driving source of the east-west CO outflow. Our new CO (3–2) observations and the 24 μm SPITZER data clearly show that the driving source of this outflow is MMS 2 (i.e. brightest MIR source) rather than MMS 3 or MMS 4. There are jets and several knots in the western side as denoted by [3] and [4] in Figure 4*a* and a possible knot in the eastern side as denoted by [2]. These knots are already found in the previous results by Yu et al. (1997) and Tsujimoto et al. (2004).

MMS 5; (*clear*)– There is a compact east-west outflow with clear bipolarity toward MMS 5 as shown in Figure 4*b*. This east-west outflow has also been identified in the CO(1–0) emission (Williams et al. 2003, Aso et al. 2000). A 24 μm source (SP 053522-050115) is located at the center of the blue and red shifted lobe. Several knots are associated with this flow, denoted by [5]

in Figure 4*a* and also detected previous shock excited H_2 observations by Yu et al. (1997) and Stanke et al. (2002). The position-velocity diagram along the major axis shows a clear velocity gradient shown in Figure 9*a*. In addition, there appears a shell-like structure (denoted by a dashed curve in Figure 4b), although the origin of this structure is not clear.

MMS 6; (*marginal*?)– MMS 6 is the brightest 1.3 mm continuum source (Chini et al. 1997). We did not find any clear signature of CO outflows (see Figure 4), as already reported by the previous CO(1–0) observations (Williams et al. 2003, Matthews et al. 2005). The faint K_s emission is located at the northern and southern part of MMS 6. These sources correspond to two 24 μm sources of SP 053524-050130 and SP 053524-050140 and We consider that these two sources are protostars rather than knots from the protostar (Yu et al. 1997, Stanke et al. 2002, Williams et al. 2003). In addition, we detected the faint jet-like feature in the eastern part of the northern 24 μm source, SP 053523-050130, denoted by [6] in Figure 4*c*, suggesting that the jet associated with the northern source may be elongated to the east-west direction. There is extended high-velocity redshifted emission in the south-eastern part of MMS 6 as shown in Figure 4*b*, but the origin of this emission is less clear.

MMS 7; (*clear*)– Figure 5 shows the giant molecular outflow associated with MMS 7, which is elongated to the east-west direction and is associated with the brightest reflection nebula (Haro - 5a/6a; Haro 1953). This east-west outflow has also been identified in the CO(1–0) observations by Aso et al. (2000) and Williams et al. (2003). The velocity of this outflow is close to the systemic velocity of the cloud and hence the configuration of this outflow is nearly plane of the sky. The blue-shifted emission and a brighter NIR nebula are located at the eastern part. This result suggests that the outflow from MMS 7 is slightly inclined from the plane of the sky (i.e. the eastern part is located at the near side). Interferometric $H^{13}CO^+$(1–0) observations show that the dense gas and the outflow are significantly interacting with each other and that the disk-like envelope has a dispersing gas motion (Takahashi et al. 2006). In addition, there is an one-side optical jet at the western side (Reipurth 1997; HH 294) and a compact 3.6 cm free-free jet (Reipurth et al. 1999, 2004), both of which have roughly the same position angle as that of the CO(3–2) flow. We also detected faint knots along the western part of the CO outflow as denoted by [7] in Figure 5*a*. The connected trajectory of the CO redshifted emission peaks shows a wiggled structure over 0.9 pc in the west side, suggesting presence of a precessing motion.

MMS 9; (*clear*)–The prominent CO(3–2) bipolar outflow is elongated to the east-west direction as shown in Figure 6*b*. This outflow has already been identified in the previous CO(1–0) observations (Aso et al. 2000, Williams et al. 2003). The P-V diagram (see Figure 9*b*) shows a clear velocity gradient with the bipolarity. We clearly detected a jet-like feature from MMS 9 at the eastern side from the IRSF/SIRIUS observations (see [9] in Figure 6*a*). There appears a wiggled chain of knots as denoted by [10] and [11] in Figure 6*a* at the western side, which trace the trajectory of the CO(3–2) blue-shifted outflow (see two prominent CO knots denoted by [i] and [ii] in Figure 6*b*). The position-velocity diagram at the CO knots also shows a wide velocity width of approximately 10 km s^{-1} in blue-shifted component. We found a bright reflection nebula [12] in Figure 6*a* which is embedded in the red-shifted outflow from MMS 9. We detected another blueshifted CO(3–2) component (named "UD-1") along the NE-SW direction in MMS 9. We also detected a NIR knot at the terminal point of this CO blueshifted lobe, at the position 53″north-east of MMS 9 (see [8] in Figure 6*a*). Because of the complexity of this region, the driving source of this outflow is difficult to identify. MMS 9 (corresponds to SP 053526-050546) or SP 053522-050546 is a possible candidate of the driving source of "UD-1", both of which are on the stream line of H_2 knot. On the other hand, MMS 8 is unlikely to be associated with the

outflow, because this object is a starless core rather than a protostellar core (i.e. there is no 24 μm source).

3.1.3. OMC-2 Region

The OMC-2 region is found to contain an embedded cluster with approximately 100 stellar components (Lada & Lada 2003). There are also more than ten millimeter and submillimeter dust condensations (Chini et al. 1997, Lis et al. 1998).

VLA 9; (probable)– The large-scale blueshifted outflow is detected in Figure 6*b* toward the north-east direction from VLA9 or the 24 μm source of SP 053526-050758. This outflow seems to be interacting with the dense gas filament which contains the dust condensation of MMS 10 (Discussion will be in section 3.2). Then, the driving source of this outflow is likely to be VLA 9 rather than MMS 10, although previous studies have reported that the driving source of this outflow is MMS 10 (Williams et al. 2003, Aso et al. 2000). A NIR feature is also seen close to the position of VLA 9. Although there is contamination of another objects, the redshifted emission is seen at the south-west of the VLA 9.

FIR 1b; (marginal)– The faint redshifted CO(3–2) emission is located at the south-east of FIR 1*b* as shown in Figure 6*b*. A weak extended blueshitfted component is distributed at the northern-west of FIR 1*b*. Although there is no obvious protostellar candidate (i.e., 24 μm source) at the position of FIR 1*b*, previous BIMA observations also show bipolarity of the blue- and red-shifted components lying approximately along the north-south direction (Williams et al. 2003). There is no apparent outflow associated with FIR 1*a* and FIR 1*c*.

FIR 2; (clear)– There is a clear bipolar outflow associated with FIR 2, centered on the 24 μm source of SP 053524-050830, as shown in Figure 7*b*. This outflow has also been identified in the CO(1–0) map (Williams et al. 2003). The blueshifted emission is located at the south-west and the redshifted emission at the north-east of the protostar. The P-V diagram shows the bipolarity with a velocity width of 12 km s^{-1}.

The FIR 3 - 5 region contains many protostellar candidates. Previous observations found nine Mid-infrared sources (Nielbock et al. 2003). There are several bright reflection nebulae and NIR features in this region, indicating the extreme complexity.

FIR 3; (clear)– There is a prominent 24 μm source, SP 053528-050935, which is located at the position of the 1.3 mm source of FIR 3. This source may be composed of two sources (MIR 21/MIR 22) as identified by Nielbock et al. (2003). Both red- and blue-shifted CO(3–2) emission is seen along the north-east to south-west direction centered on FIR 3, as shown in Figure 7*b*. This outflow was also identified in the CO(1–0) and CO(2–1) emission (Williams et al. 2003, Wu et al. 2005). The configuration suggests that the axis of the outflow associated with FIR 3 is nearly plane of the sky. The P-V diagram shown in Figure 9*d* shows "butterfly-like velocity structure" centered on FIR 3, which also supports the configuration along the plane of the sky. Bright knots and jet-like features are seen at the north-east of FIR 3 in the JHK_s image (see Figure 7-[14]). The bright NIR jet-like feature associated with the 24 μm source of 053527-050923 (also identified MIR 20 by Nielbock et al. 2003) is located at 15″ north-west of FIR 3 (see Figure 7-[15]). We also detected extended CO(3–2) blueshifted emission along this NIR jet (Figure 7*b*).

FIR 4; (marginal?)– The strong millimeter source FIR 4 associated with a free-free jet is in

close neighborhood of SP 053527-051002. Although the CO line profile toward FIR 4 shows a broad wing, no clear bipolar CO outflow associated with FIR 4 is identified in the CO map. One possible reason of the negative-detection is that the outflow from FIR 3 is too strong and makes it difficult to extract the CO emission from FIR 4. We also detected a faint NIR nebula in the vicinity of VLA 12 and FIR 4 ([16] in Figure 7*c*).

FIR 5; (*no*)– A 24 μm source, SP 053527-051017 (corresponding to MIR 27 from Nielbock et al. 2003), is located at 10″ NW of FIR 5. This source is also bright in J and H-bands, suggesting presence of an evolved young star. There is no clear CO outflow around this region.

VLA 13; (*clear*)– There is a bright cone-shaped K_s reflection nebula centered on VLA 13 ([16] in Figure 7*a*). We detected the bipolar outflow along the north-south direction. The blue-shifted emission is located at the northern part and red-shifted emission southern part of VLA 13 and the distribution is well-correlated with the K_s reflection nebula. VLA 13 coincides with a bright 24 μm source, SP 053525-051031, as shown in Figure 7*b*.

FIR 6.– A "clear" bipolar outflow lies north-east to south-west centered on FIR 6*b*, which is associated with the 24 μm source, SP 053523-051205 (see Figure 8*b*). We see the velocity gradient in the position-velocity diagram cut along the CO outflow. We also detected the "probable" CO(3–2) bipolar outflow along the north-south direction centered on FIR 6*c*. There is "no" clear CO outflow toward FIR 6*a* and FIR 6*c*.

CSO 31 – 33.– We marginally detected the CO(3–2) high-velocity emission toward CSO 32 and probably detected CO(3–2) outflow toward CSO 33 (see Figure 8*b*), although it is difficult to distinguish whether the origin is the outflow or shocked gas from the eastern HII region, M 43. Specifically, a clear bipolarity is seen at the position of CSO 33 as well as the reflection nebula in the K_S band image (See Figure 8*a*).

3.2. Outflow - Dense core Interaction

We found possible evidence for interaction between outflows and ambient gas in the OMC-2/3 region. In Figure 10, we compare the distribution of the 850 μm dust continuum emission with the CO(3–2) high-velocity outflows. At least two dusty condensations in OMC 3 and one dusty condensation in OMC 2 are located at the terminal point of the CO outflow. In Figure 10*a*, millimeter source, MMS 10, seems to be compressed by the blue-shifted outflow from VLA 9. This dusty condensation has no MIR source and no signature of a protostar, suggesting that MMS 10 is a starless core. In Figure 10*b*, a dusty condensation is "pinched" between the red-shifted outflows from MMS 7 and MMS 9. This compressed core has neither signature of a central star and seems to be a starless dusty condensation. One of the strongest millimeter sources, FIR 4, is strongly compressed by a molecular outflow driven by FIR 3 as shown in Figure 10*c*. In addition, the 3.6 cm source (VLA 12) and a 24 μm source (SP 053527-051002), signs of the presence of protostars, are detected in the compressed dusty condensation of FIR 4. These results may imply that the outflow from FIR 3 triggered the star-formation at the inner part of FIR 4. (Detailed interpretation of the kinematics, time-scale and physical properties of FIR 4 will be the subject to the forthcoming paper.) Our results suggest that the outflows could affect the formation and evolution of dense gas in OMC-2/3. Recent 3D MHD simulations suggest that outflow-driven turbulence is important for the formation and evolution of embedded clusters (Li & Nakamura 2006).

3.3. Notable NIR sources

We newly found two interesting NIR objects in the OMC-2/3 region with the SIRIUS/IRSF as shown in Figure 11.

A NIR source (hereafter 053527-051150) is located at the $\sim$ 1.5′ south-east of VLA 13 as shown in Figure 11*a*. We can see a central bright star and surrounding reddened material which is elongated along the north-east to south-west direction with a size of 8″ (corresponding to 3600 AU) along the outflow cavity. The size of minor axis is $\sim$ 4″ (corresponding to 1800 AU). These result suggests that this source is a one of low-mass protostar candidates.

Another NIR source (hereafter 053532-05115) shown in Figure 11*b* is located at the 80″ NW of FIR 6b. We can clearly see a silhouette disk (there is a central obscuring region) and the NIR brighter cavity-like structure as is also see along NE-SW direction. Because the the size of dusty flattened envelope is expected to a few thousand AU, this object is also low-mass protostar candidate.

4. Data Analysis of the CO(3–2) Emission

Table 3 summarizes parameters categorized as CLEAR and PROBABLE detected outflows. Inclinations of the outflow toward SIMBA *a* and MMS 5 were estimated to be by the axis ratio of the associated dense envelope traced by the $H^{13}CO^+$(1–0) emission (Takahashi et al. in preparation). Since the outflow associated with MMS 7 and FIR 3 is nearly along the plane of the sky as seen in the CO and NIR data, we assume these outflow inclinations to be 80 °. For other objects which have a clear red- and (or) blue -shifted lobes, we adopted the inclination of 55 ° which is a median value of those of above objects. We consider that the typical error of the outflow inclinations of approximately ± 10°. The maximum size ($R_{\rm max}$) and maximum velocity ($V_{\rm max}$) of the CO(3–2) outflows are determined by eyeball based on the CO velocity channel maps and P-V diagrams with above 3 σ emission level. We measured the intensity of the CO(3–2) emission with brighter than 3 σ emission level. Assuming that the CO(3–2) high-velocity emission is optically thin and that the distribution of the excitation temperature and CO abundance are uniform, we estimated the LTE mass ($M_{\rm CO}$) as

$$M_{\rm LTE}\ [M_\odot] \ = \ \bar{\mu}\ m_{\rm H}\ X[{\rm CO}]\ \Omega_{\rm S}\ D^2 N_{\rm CO}, \tag{III.1}$$

where

$$N_{\rm CO}\ [{\rm cm}^{-2}] \ = \ \frac{8\pi\nu^3}{c^3} \times \frac{1}{(2J_l+3)A} \times \frac{Z(T_{\rm ex})}{\exp(-E_l/kT_{\rm ex})[1-\exp(h\nu/kT_{\rm ex})]} \times \frac{T_B^* \Delta V}{J(T_{\rm ex})}, \tag{III.2}$$

and

$$J(T) \ = \ \frac{h\nu/k}{\exp(h\nu/kT)-1}. \tag{III.3}$$

In the above expressions, $\bar{\mu}$ is the average molecular molecular weight of 2.33, $m_{\rm H}$ is the atomic mass, h is the Planck constant, k is Boltzmann's constant, c is the speed of light, ν is the

line frequency, $T_{\rm ex}$ is the excitation temperature of the CO transitions, Ω is a solid angle of each source, D is a distance to each source, N is the column density, $T_{\rm bg}$ is the background radiation temperature, A is the Einstein A-coefficient of the transition, Z is the partition function, E_l is the rotational energy level of the lower energy state. J_l is the rotational quantum number of the lower energy state, and T_B^* is the integrated line intensity. We, here, adopted $T_{\rm ex}$ of 60 K (Hogerheijde et al. 1998) and X[CO] of 10^{-4} (e.g., Frerking, Langer & Wilson 1982). If the inclination angle of the outflow is i, the maximum size and maximum velocity of the outflow are $R_{\rm max} = R_{\parallel}/\sin i$, and $V_{\rm max} = V_{\perp}/\cos i$, the after correction for the inclination, respectively. We obtained the outflow dynamical time, $t_d = R_{\rm max}/V_{\rm max}$, Mass Accretion rate, $\dot{M}_{\rm CO} = M_{\rm CO}/t_d$, Momentum, $P_{\rm CO} = M_{\rm CO} \times V_{\rm max}$, and Momentum rate, $F_{\rm CO} = P_{\rm CO}/t_d$ listed their values in Table 3 and 4.

5. DISCUSSION

5.1. Dependence of Outflow Properties on Mass of Driving Source

Figure 12 compares histograms of the CO outflow mass and momentum rate in low-, intermediate-, and high-mass protostellar candidates. Nine samples of Taurus sources are adopted as a low-mass protostellar candidates (Class 0 and Class I objects from Hogerheijde et al. 1998) which is estimated by the CO(3–2) observations using the JCMT with a spatial resolution of 14″. Five samples with a central luminosity of several $\times$ 10^4 $L_\odot$ are adopted as a high-mass proto-stellar candidates (from Wu et al. 2005) which is estimated by the CO(2–1) observations using the NRAO 12m telescope with a spatial resolution of 29 ″. The median value of the outflow momentum rate associated with the intermediate-mass objects in the OMC-2/3 region is between that of Taurus and high-mass samples. Because the OMC-2/3 region is three times more distant than Taurus, the observational sensitivity at OMC-2/3 is approximately 10 times less than that of Taurus The sensitivity difference causes the underestimation of the outflow mass and momentum for the more distant targets in OMC-2/3. We have to consider the detection limit of these parameters (and difficult to estimate these values) in high-mass samples. In spite of this effect, we revealed systematic increase in the outflow momentum rate from low- to high-mass samples.

In Table 4, we compare median values of the CO(3–2) outflow parameters between the Taurus and OMC-2/3 samples. These parameters are not corrected for the sensitivity difference caused by the difference of the distance. The median values of the mass, mass ejection rate and momentum rate of the CO outflows in the OMC-2/3 samples are typically more than one order of magnitude larger than that of low-mass counterparts. If the mass ejection rate of outflow is proportional to the mass accretion rate (Shu et al. 1988, Edwards et al. 1993) and that efficiency of the mass outflow to infall rate not depend the mass of the formed star, the significant mass outflow rate of the OMC-2/3 objects implies typically one-order of magnitude larger mass accretion rate than that of Taurus.

Figure 13 shows the outflow momentum rate as a function of the envelope masses derived from the 1.3 mm continuum fluxes. Previous low-mass studies suggest that the outflow momentum rate decreases with the protostellar evolution from Class 0 to Class I (Bontemps et al. 1996), as seen in the figure. Our data samples in OMC-2/3 denoted by grey diamonds in Figure 13 show the similar (or higher) outflow momentum rate to that in the low-mass Class 0 samples and the higher envelope mass than that of the low-mass counterpart. The dynamic range of the $F_{\rm CO}$ and $M_{\rm env}$ value in the OMC-2/3 sample is less than that of the low-mass sample. This result suggest

that the F_{CO} and M_{env} relation is quantitatively different between the low-luminosity objects in Bontemps et al. (1996) and our intermediate-mass samples in OMC -2/3.

Figure 14 shows the outflow momentum rate as a function of the centimeter luminosities from low- to intermediate-mass YSOs (Anglada et al. 1995, Hogerheijde et al. 1998, Reipurth et al. 1999, Saito et al. 2006 in private cominucation). Young low- and intermediate-mass stars cannot produce a detectable photo-ionized H II region. Then, the free-free emission from these objects mainly comes from shock-ionized gas produced when a stellar wind/jet collides against the surrounding high density material (Anglada 1995 for a review, Reipurth et al. 1995). In Figure 14, the centimeter luminosities in OMC-2/3 and Taurus are derived from 3.6 cm observations, and those in other 25 low- to intermediate-mass samples are derived from the 6 cm observations. Here, we considered that the flux densities at the 3.6 cm and 6.0 cm are quite similar [†] . There appears a positive correlation between F_{CO} and the centimeter luminosity in all the sample of OMC-2/3, Taurus, other 25 low- to intermediate-mass protostars. This result indicate a scaling law between the large-scale molecular outflow and ionized jets, irrespective of the mass of the formed stars. Curiel, Canto & Rodriguez (1987) and Curiel et al. (1989) explained this correlation as powerful stellar wind that produces the shock ionized gas. In this scenario, assuming that the stellar wind velocity is 200 km s^{-1} and the electron temperature of the ionized gas is 10^4 K, the momentum rate in the molecular outflow and the centimeter luminosity at 6 cm are related by

$$\left(\frac{F_{CO}}{M_{\odot}\mathrm{yr}^{-1}}\right) = \frac{10^{-3.5}}{\eta}\left(\frac{S_{\nu}d^2}{\mathrm{mJy\ kpc}^2}\right), \tag{III.4}$$

where $\eta = \Omega/4\pi$ is an efficiency factor of the fraction of the stellar wind that is shocked and produces the observed radio continuum. Anglada et al. (1995) and (1996) found a correlation of $F_{CO} = 10^{-2.6\pm0.5}(S_{\nu}d^2)^{1.1\pm0.4}$ ($r = 0.6$), consistent with an efficiency factor η of 0.1 (doted line in Figure 14). This positive correlation is consistent with our results in OMC-2/3 and Taurus data. ! !

5.2. Evolution of CO Outflows associated with Intermediate-mass Protostars

Figure 15 shows the CO outflow momentum plotted as a function of the 24 μm fluxes. The 24 μm emission traces warm dust emission with a temperature of 150 K (e.g. Rho et al. 2006). In the case of $L = 100\ L_{\odot}$ which is a typical bolometric luminosities of our OMC-2/3 objects, a radius with $T > 150$ K is calculated to be 75 AU along the disk axis and 250 AU along the cavity eroded by the outflow, based on the two-dimensional radiative transfer model by Nakazato et al. (2003). Therefore, the 24 μm emission mainly traces a circumstellar disk or an innermost envelope. Our result shows that the 24 μm flux has a positive correlation with the CO outflow momentum except for one object which is located at the top left area in Figure 15. Objects with the higher CO outflow momentum and 24 μm flux, MMS 2, MMS 7, VLA 9, FIR 3, and VLA 13, denoted by shaded area in Figure 15, are associated with a reflection nebula in the NIR image as shown in Figure 4, 5, 6 and 7, and a free-free jet traced by the 3.6 cm emission. The presence of the NIR nebula implies the formation of cavities along the outflow axis and the dissipation of

[†]One of the low-mass protostellar objects, L 1551 IRS 5, the flux density at 3.6 cm and expected flux density at 6 cm show quite similar values (Figure 3 in Rodriguez et al. 1998)

the dense-gas envelope, as already discussed in the case of MMS 7 (Takahashi et al. 2006). On the other hand, there is no clear reflection nebula and no free-free emission toward the sources with the smaller CO outflow momentum and 24 μm flux (SIMBA *a*, MMS 5, FIR 2 and FIR 6*b*). Therefore, the objects with more intense 24 μm flux and the 3.6 cm flux are likely to be more evolved, and Figure 15 suggests that the CO outflow momentum also increases as the protostellar evolution, as denoted by an arrow in Figure 15.

There is no obvious correlation between the core dissipation and their envelope mass estimated by the 1.3 mm continuum emission (Chini et al. 1997). This is inconsistent with the age and mass loss relation derived by Bontemps et al. (1996) shown in Figure 13. One possible explanations is that the OMC -2/3 samples are in the similar and earliest stage of the protostellar evolution, and hard to distinguish a decay of the mass loss processes quantitatively.

In summary, we have revealed a correlation between the CO outflow momenta (i.e., outflow evolution) and the dissipation of the circumstellar material associated with the intermediate-mass protostars.

5.3. Direction of the CO outflows

Figure 16 shows histograms of the outflow position angle (demonstrated by absolute values). The outflow position angles in OMC-3 are concentrated around $\pm 90°$ as shown in Figure 16*a* (and also shown in Figure 1). One of the possible explanations for this alignment is an effect of the magnetic field (—references—). The polarization pattern of the dust filament was measured at 850 μm taken with SCUBA/JCMT (Matthews et al. 2001) and 350μm taken with SHARC/CSO (Houde et al. 2004), and the polarization pattern is highly aligned along the filament, suggesting that the magnetic field is primarily perpendicular to the filament (P.A. = 40 - 75°). The axes of the magnetic field are not correlated with the direction of the outflows, so the magnetic field is unlikely to be the reason for the CO outflow alignment.

Another possible explanation for the alignment of the CO outflow in OMC-3 is large-scale angular momentum in the filament. Previous CS (1–0) observations found a north-south velocity gradient over the Ori A integrated-shaped filament, with a velocity difference up to 7 km s^{-1} (Tatematsu et al. 1993). We also detected similar trend of the velocity gradient toward several protostellar candidate in OMC-3. One of the sample, MMS 7, is shown in Figure 7*c* of Takahashi et al. (2006). The critical value of the magnetic flux that can support the rotational energy is approximately 170 μG in MMS7 [‡] , which is much larger than the magnetic field strengths of GMCs: i.e., on the order of a few 10 μG (e.g., Bourke et al. 2001). Therefore, we speculate that the fragmentation occurred at a super critical condition and each core keeps the original rotation motion along the north-south direction, then the outflow axes in OMC-3 could align along the direction perpendicular to the rotation of the core.

On the other hand, the distribution of the outflow position angles in OMC-2 seems random as shown in Figure 16*b*. Although the outflow direction associated with FIR6*b* at the southern part of OMC-2, P.A.$\sim$65°, is weakly correlated with the magnetic field (Houde et al. 2004), in the case of FIR 2, FIR 3, and VLA 13 the outflow axes are not correlated with the magnetic field.

[‡]We, here, adopted the rotational velocity, core mass and H_2 density in MMS 7 to be 2 km s^{-1}, 5.1 $M_\odot$ and 10^5 cm^{-3}, respectively.

One of the possible reasons for the random distribution is the star-forming environment. Previous studies suggest that OMC-2 is a cluster-forming region (Johnson et al. 1990) and contains MIR sources with a number density of 200 pc^{-2} toward the most complex region: FIR 3–5 (Nielbock et al. 2003). In addition, we also detected the different clustering of the dusty-core distribution (Detailed results will be the subject to the forthcoming paper.). These results imply that cluster formation in OMC-2 may break the initial angular momentum in the filament. Therefore, the axes of the outflows are not aligned with the velocity gradient in the filament. Figure 6 shows a typical cluster-forming region in OMC-2, which contains numerous jets and outflows whose directions are almost random. Furthermore, as mentioned in section 3.2, we found the interaction between the outflow and the dusty condensations toward the most complicated region.

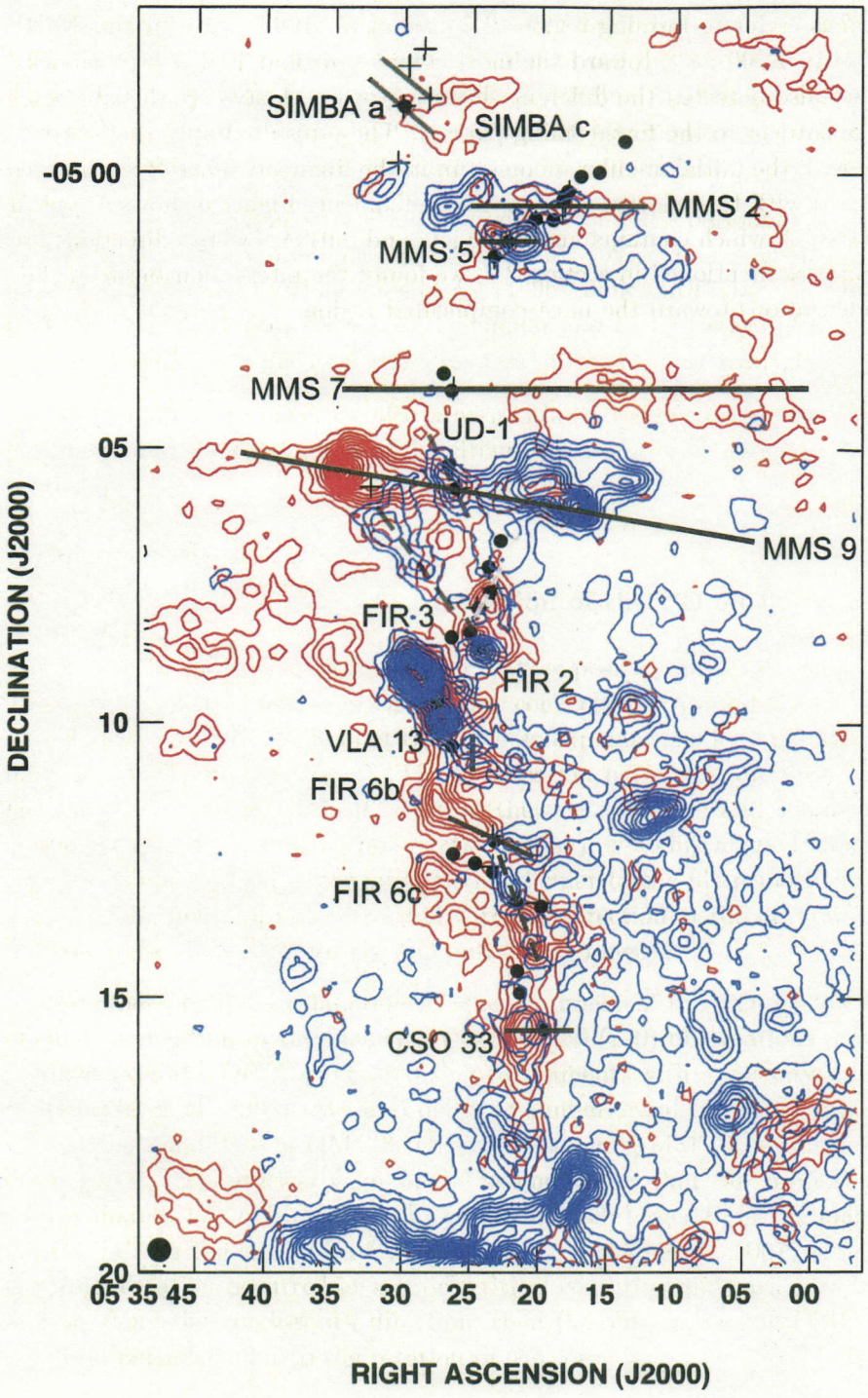

Fig. 1.— CO(3-2) integrated intensity map of the OMC-2/3 region. The blue and red contours show the blue- and red-shifted components in the velocity range of -6.2 to 7.8 km s^{-1} and 14.3 to 27.3 km s^{-1}, respectively. Contour intervals are 0.45 K starting at 0.45 K. The crosses and dots indicate position of 1300 μm and 350 μm sources, respectively (from Chini et al. 1997, Lis et al. 1998).

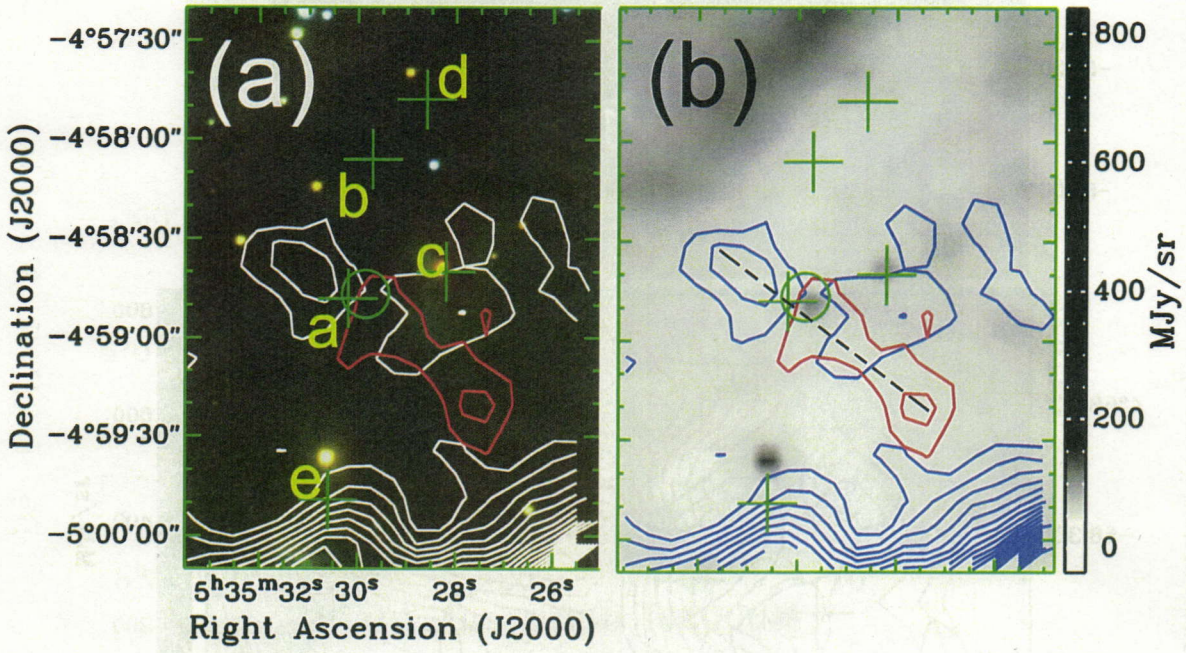

Fig. 2.— CO(3-2) integrated intensity map of the SIMBA region. (a) JHK_s image taken by the IRSF/SIRIUS. (b) Maps of the CO(3-2) high-velocity emission taken with the ASTE telescope superposed on the SPITZER/MIPS 24 μm image. The blue (white in Figure *a*) and red contours show the blue- and red-shifted components in the velocity range of 7.8 km s^{-1} $< V_{\rm LSR} <$ 8.9 km^{-1} and 15.4 km s^{-1} $< V_{\rm LSR} <$ 16.5 km^{-1}, respectively. Contour intervals are 1.13K km s^{-1} starting at 2.25K km s^{-1}. Solid line shows the clearly detected outflow. The crosses and open circles indicate position of 1300 μm and 350 μm sources, respectively (from Nielbock et al. 2003, Lis et al. 1998).

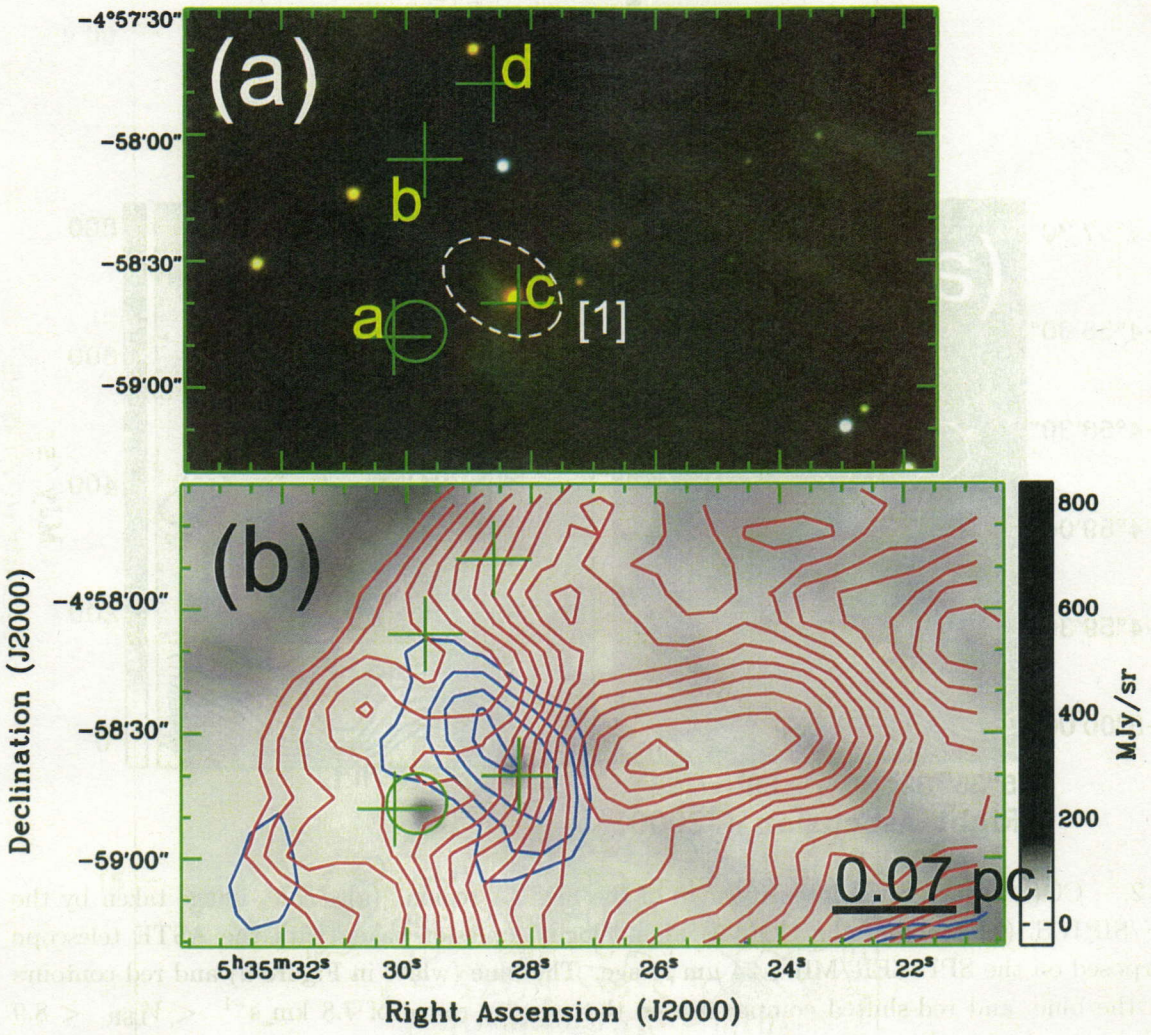

Fig. 3.— CO(3-2) integrated intensity map of the SIMBA region. (a) JHK_s image taken by the IRSF/SIRIUS. (b) Maps of the CO(3-2) high-velocity emission taken with the ASTE telescope superposed on the SPITZER/MIPS 24 μm image. The blue (white in Figure *a*) and red contours show the blue- and red-shifted components in the velocity range of 8.9 km s^{-1} $< V_{\rm LSR} <$ 10.1 km^{-1} and 13.5 km s^{-1} $< V_{\rm LSR} <$ 14.2 km^{-1}, respectively. Contour intervals are 1.50 K km s^{-1} starting at 10.00K km s^{-1}. Doted line shows the probably detected outflow. The crosses and open circles indicate position of 1300 μm and 350 μm sources, respectively (from Nielbock et al. 2003, Lis et al. 1998).

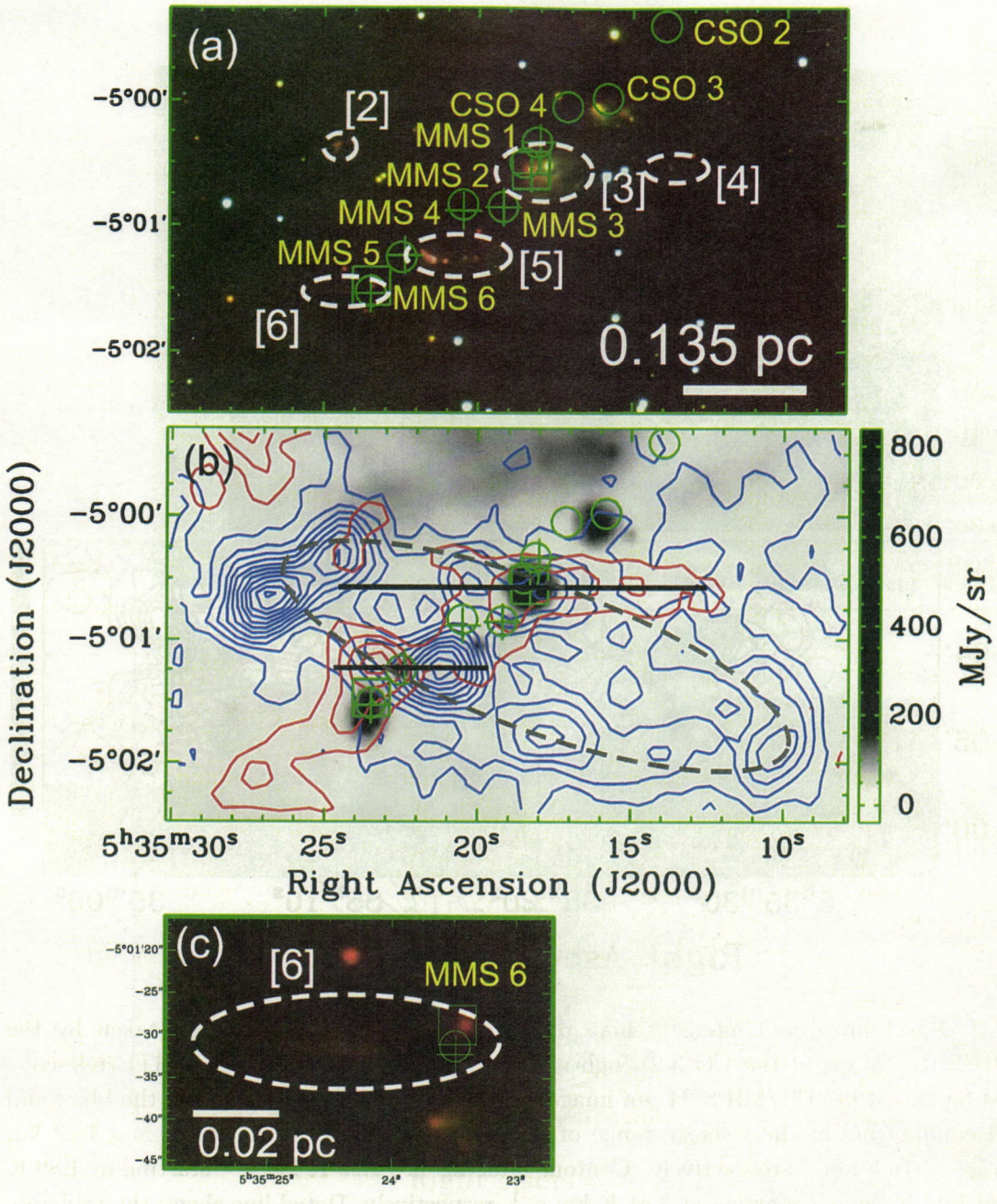

Fig. 4.— CO(3-2) integrated intensity map around the north-part of the integrated intensity filament (north of the OMC-3 region). (a) JHK_s image taken by the IRSF/SIRIUS. (b) Maps of the CO(3-2) high-velocity emission taken with the ASTE telescope superposed on the SPITZER/MIPS 24 μm image. The blue and red contours show the blue- and red-shifted components in the velocity range of 1.3 km s^{-1} $\leq V_{\rm LSR} \leq$ 6.7 km^{-1} and 14.3 km s^{-1} $\leq V_{\rm LSR} \leq$ 15.4 km^{-1}, respectively. Contour intervals are 2.4 K km s^{-1} starting at 3.6 K km s^{-1} and 1.46 K km s^{-1} starting at 2.19 K km s^{-1} , respectively. The crosses open circles and open squar indicate position of 1300 μm, 350 μm and 3.6 cm sources, respectively (from Chini et al. 1977, Lis et al. 1998, Reipurth et al. 1999). Solid- and doted line show the clearly and probably detected outflow, respectively.

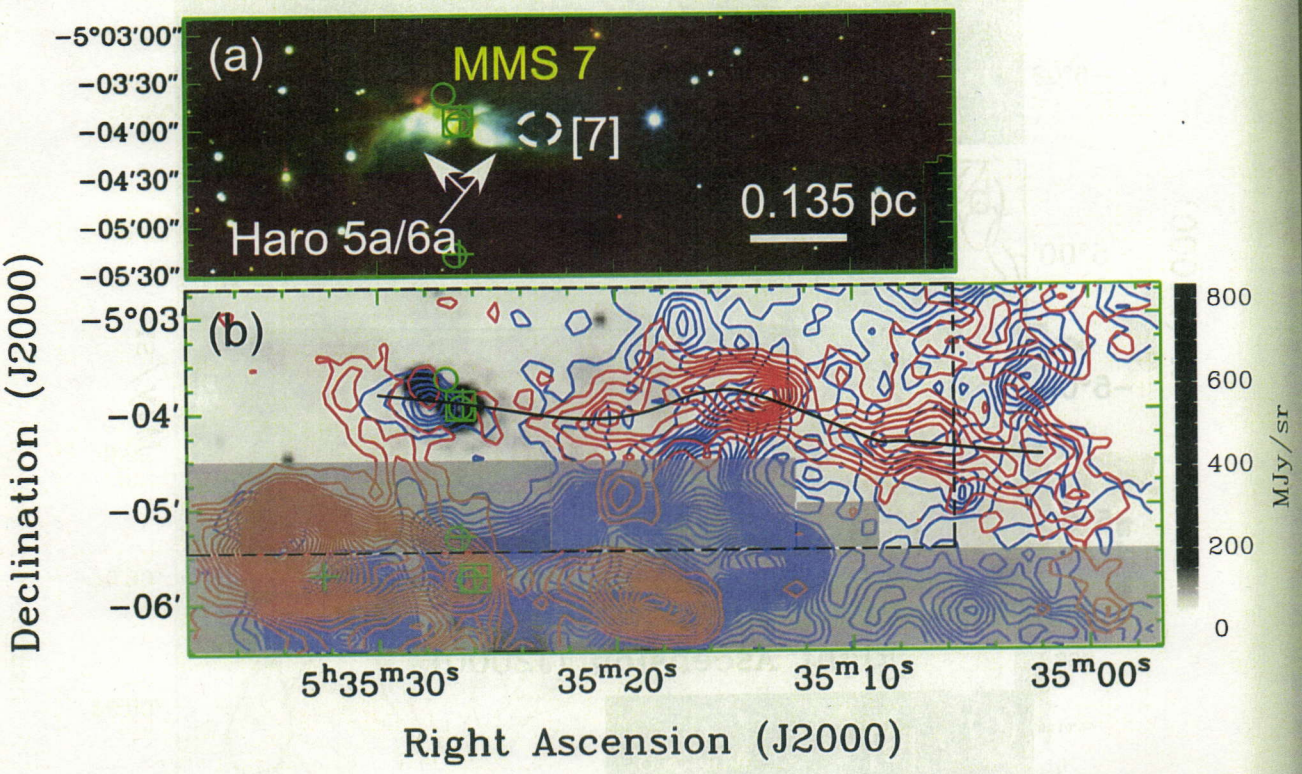

Fig. 5.— CO(3-2) integrated intensity map of the MMS 7. (a) JHK_s image taken by the IRSF/SIRIUS. (b) Maps of the CO(3-2) high-velocity emission taken with the ASTE telescope superposed on the SPITZER/MIPS 24 μm image. The blue and red contours show the blue- and red-shifted components in the velocity range of 6.7 km s^{-1} $\leq V_{\rm LSR}$ $\leq$ 7.8 km^{-1} and 14.3 km s^{-1} $\leq V_{\rm LSR} \leq$ 16.5 km^{-1}, respectively. Contour intervals are 1.26 K km s^{-1} starting at 1.89 K km s^{-1} and 1.74 K km s^{-1} starting at 2.61 K km s^{-1}, respectively. Doted line shows the probably detected outflow.

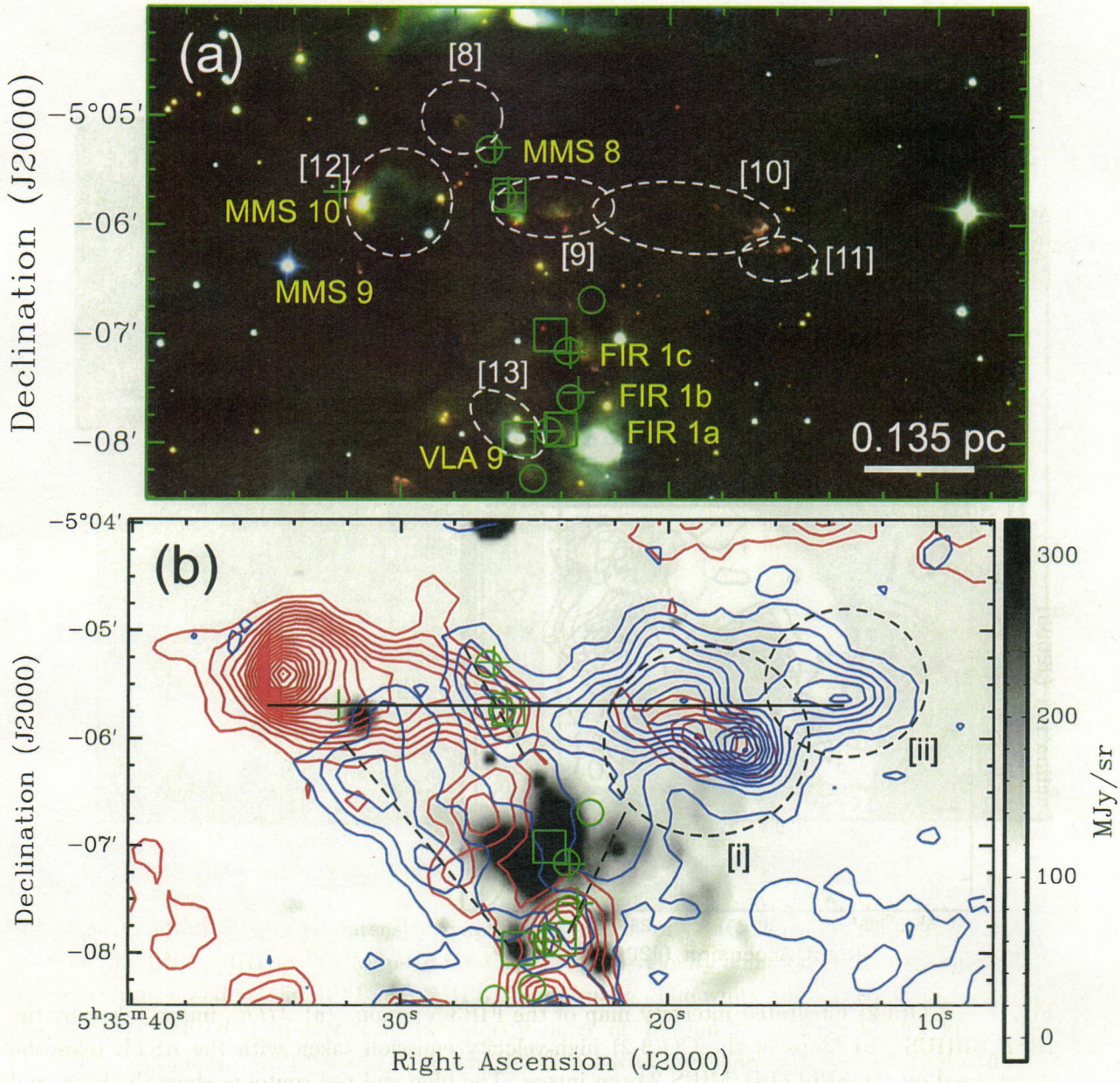

Fig. 6.— CO(3-2) integrated intensity map of the MMS 8- FIR1 region. (a) JHK_s image taken by the IRSF/SIRIUS. (b) Maps of the CO(3-2) high-velocity emission taken with the ASTE telescope superposed on the SPITZER/MIPS 24 μm image. The white and red contours show the blue- and red-shifted components in the velocity range of -1.9 km s^{-1} $\leq V_{\rm LSR}$ $\leq$ 6.7 km^{-1} and 14.3 km s^{-1} $\leq V_{\rm LSR} \leq$ 21.9 km^{-1}, respectively. Contour intervals are 6.90 km s^{-1} K starting at 4.14 km s^{-1} K and 4.62 km s^{-1} K starting at 7.70 km s^{-1} K, respectively. Solid- and doted line show the clearly and probably detected outflow, respectively.

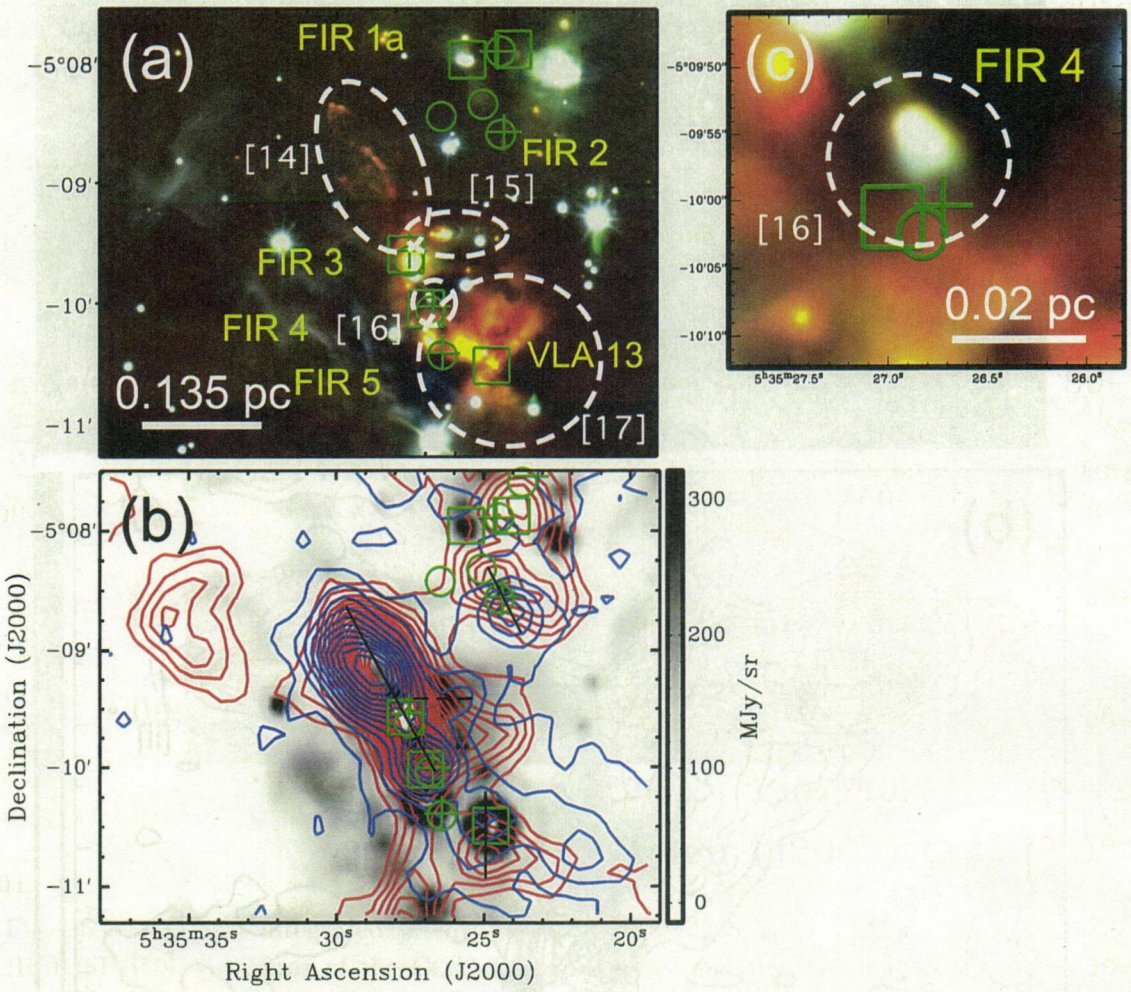

Fig. 7.— CO(3-2) integrated intensity map of the FIR3-5 region. (a) JHK_s image taken by the IRSF/SIRIUS. (b) Maps of the CO(3-2) high-velocity emission taken with the ASTE telescope superposed on the SPITZER/MIPS 24 μm image. The blue and red contours show the blue- and red-shifted components in the velocity range of -4.1 km s^{-1} $\leq V_{\rm LSR}$ $\leq$ 6.7 km^{-1} and 14.3 km s^{-1} $\leq$ $V_{\rm LSR}$ $\leq$ 21.9 km^{-1}, respectively. Blue- and red-contour intervals are 8.40 km s^{-1} K starting at 5.04 km s^{-1} K and 4.62 km s^{-1} K starting at 7.70 km s^{-1} K, respectively. Solid- and doted line show the clearly and probably detected outflow, respectively.

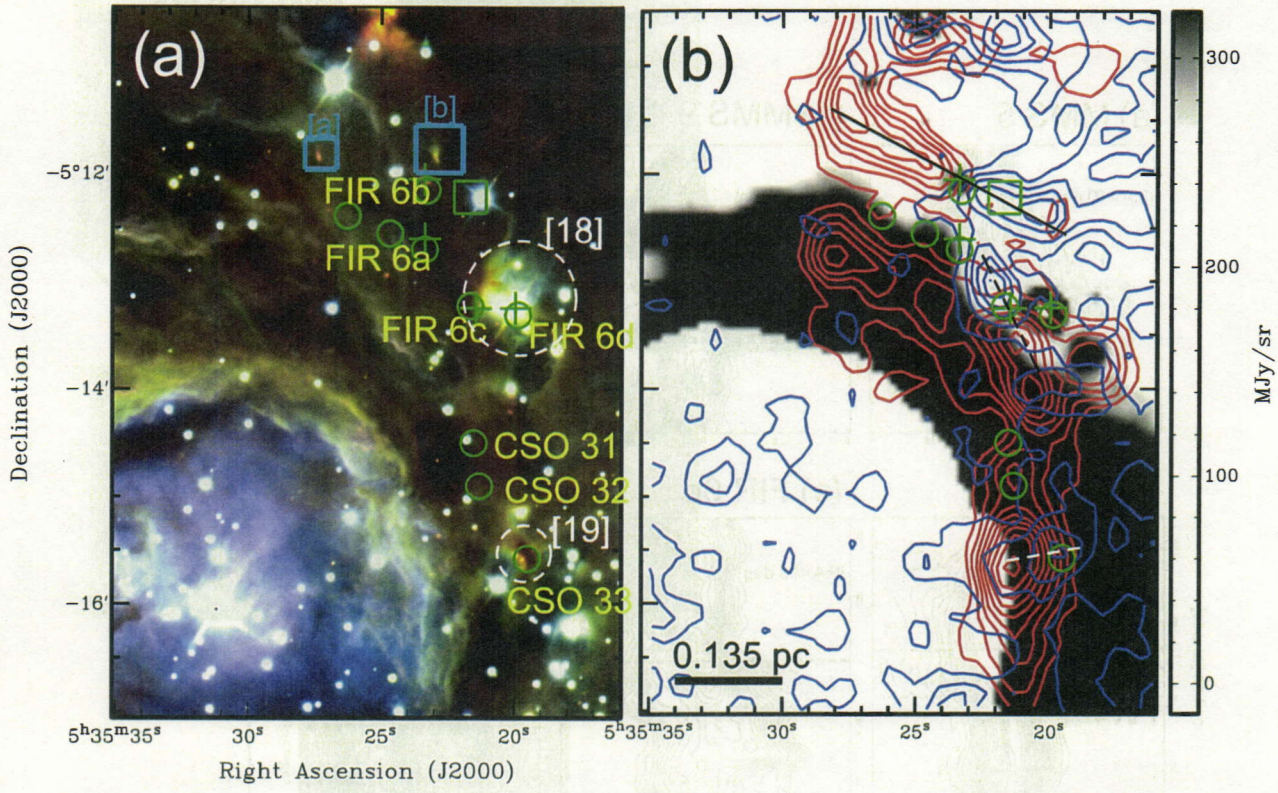

Fig. 8.— CO(3-2) integrated intensity map of the sourth of OMC-2 region. (a) JHK_s image taken by the IRSF/SIRIUS. (b) Maps of the CO(3-2) high-velocity emission taken with the ASTE telescope superposed on the SPITZER/MIPS 24 μm image. The white and red contours show the blue- and red-shifted components in the velocity range of -3.9 km s^{-1} $\leq V_{\rm LSR} \leq$ 6.7 km^{-1} and 14.3 km s^{-1} $\leq V_{\rm LSR} \leq$ 21.9 km^{-1}, respectively. Contour intervals are 4.65 km s^{-1} K starting at 4.65 km s^{-1} K and 4.62 km s^{-1} K starting at 4.62 km s^{-1} K, respectively. Solid- and doted line show the clearly and probably detected outflow, respectively.

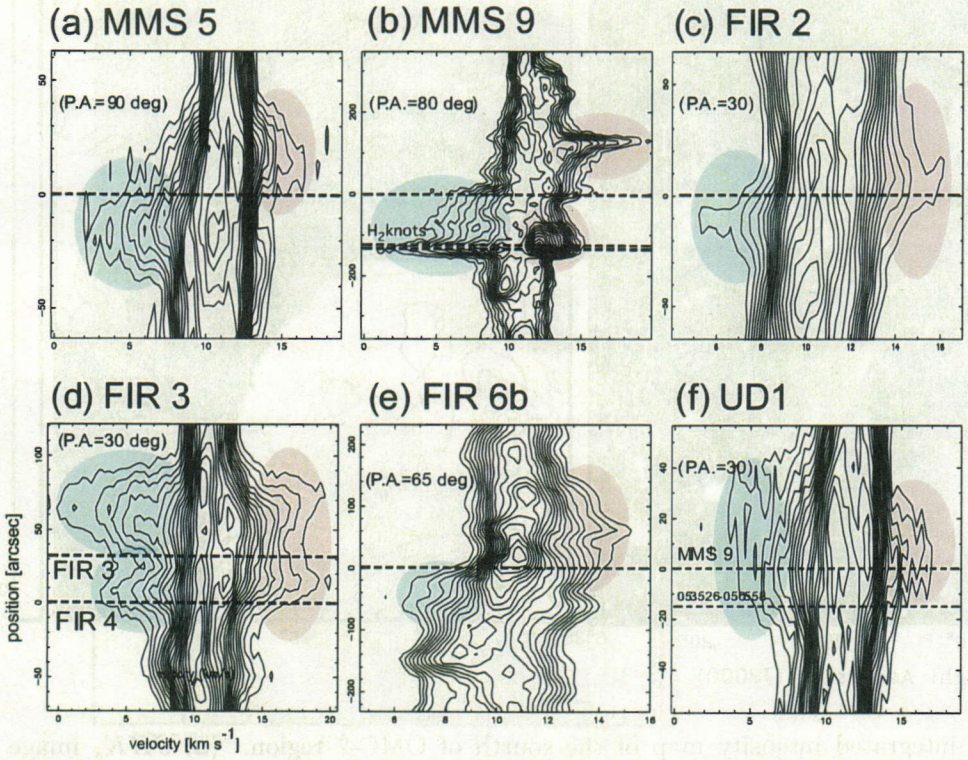

Fig. 9.— Position-velocity diagrams along the major axis toward Clear bipolar outflows in OMC-2/3. The contour starting level and increment are 10% level of the peak intensity in each maps and 5%, respectively.

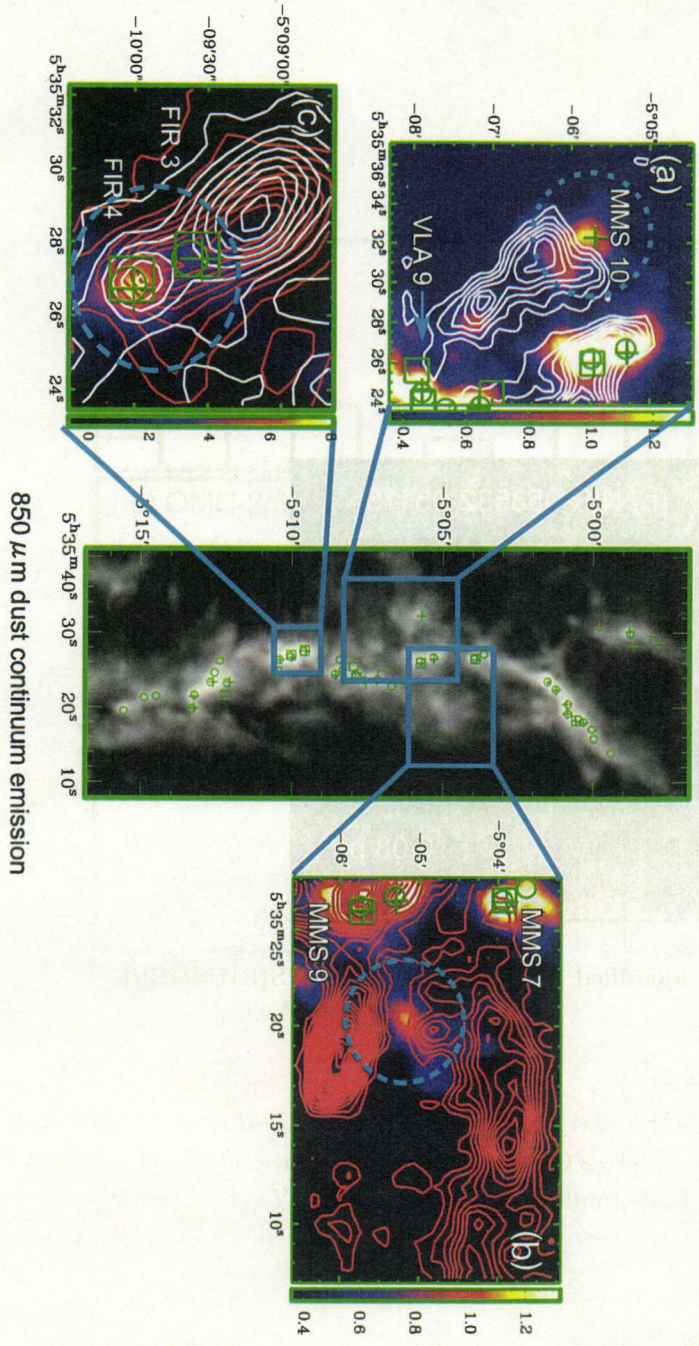

Fig. 10.— Maps of the CO(3–2) high-velocity emission taken with ASTE telescope superposed on the 850μm dust continuum emission taken by Johnstone et al. 2003.

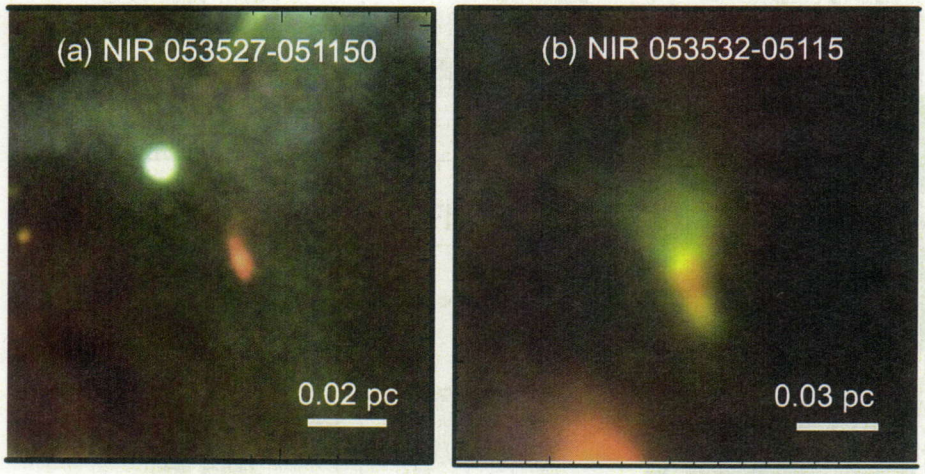

Fig. 11.— The JHK's image of the newly identified NIR features taken by SIRIUS/IRSF

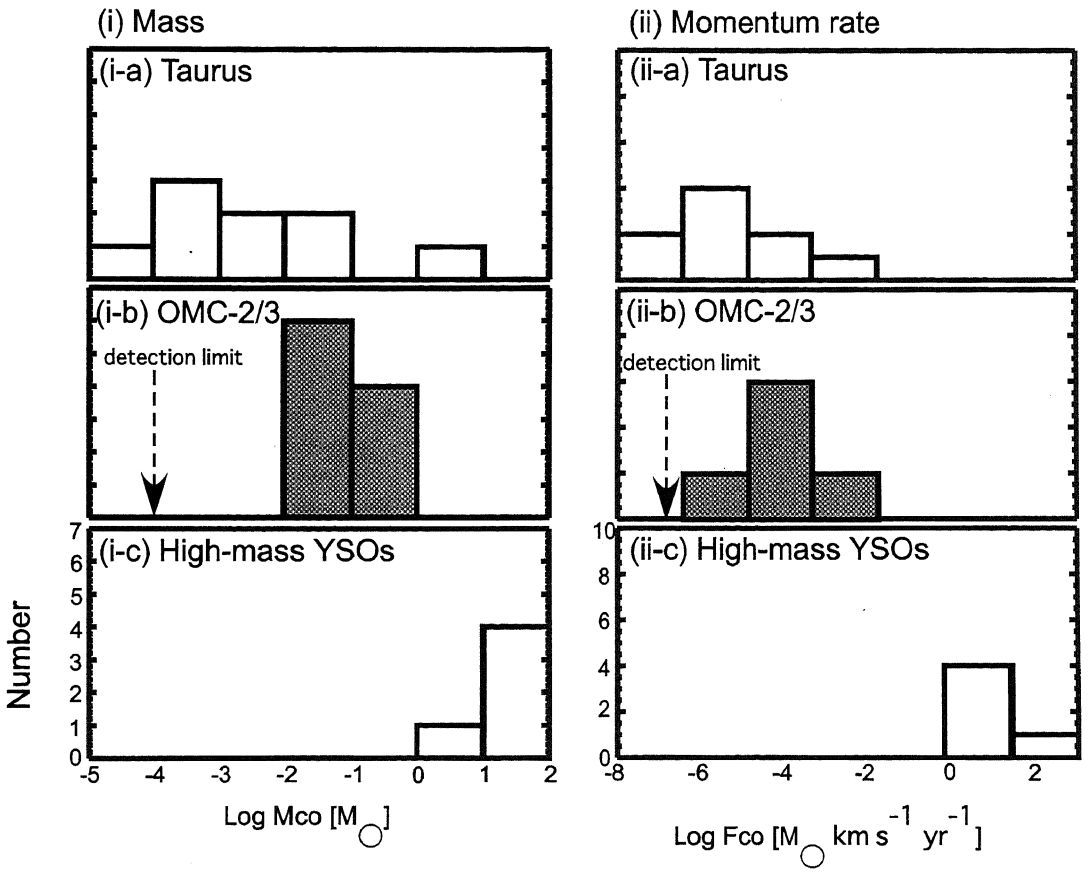

Fig. 12.— Distribution of outflow momentum rate toward (a):Taurus, (b):OMC-2/3, and (c):high-mass samples. Nine samples of low-mass YSO's are reffered from Hogerheijde et al. (1998). Five samples of hihg-mass YSO's with the central lluminosity of several $\times$ 10^4 $L_{\odot}$ are reffered from Wu et al. (2005).

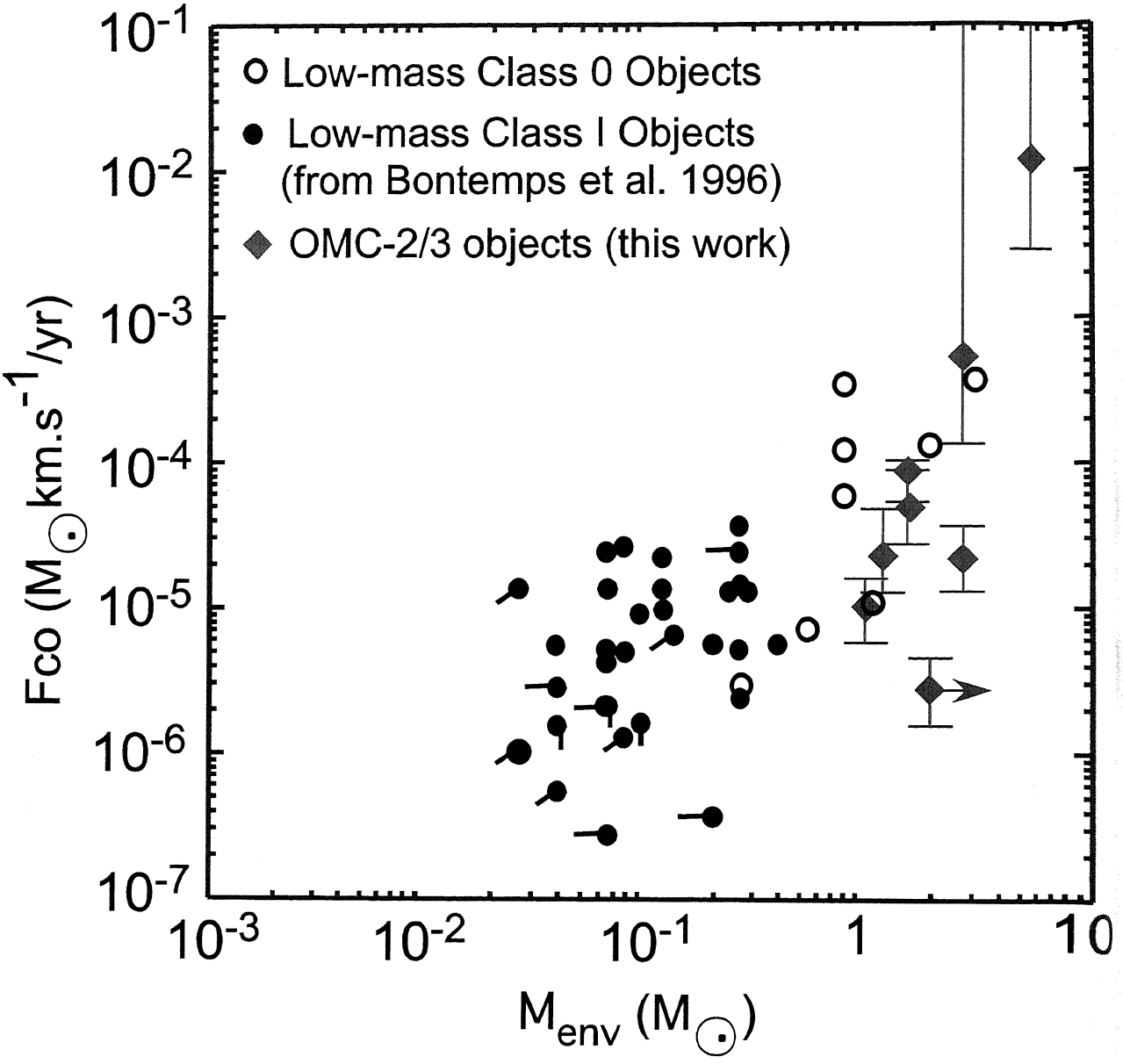

Fig. 13.— The CO outflow momentum rate plotted as a function of the mass of dust condensations. OMC-2/3 data were denoted by red filled triangles. The envelope mass of these condensations were derived from 1.3 mm total flux (Chini et al. 1997). We, here, assumed that a dust temperature of 20K, a mass opacity of 1, and gas-to-dust ration of 100, respectively. Open circles and filled circles represent data from low-mass Class 0 and Class I objects (Bontemps et al. 1998). Envelope masses in Bontemps et al. (1998) were derived from 1.3 mm maps over a region typically $\sim$1′ (corresponding to $\sim 10^4$ AU at d=160 pc).

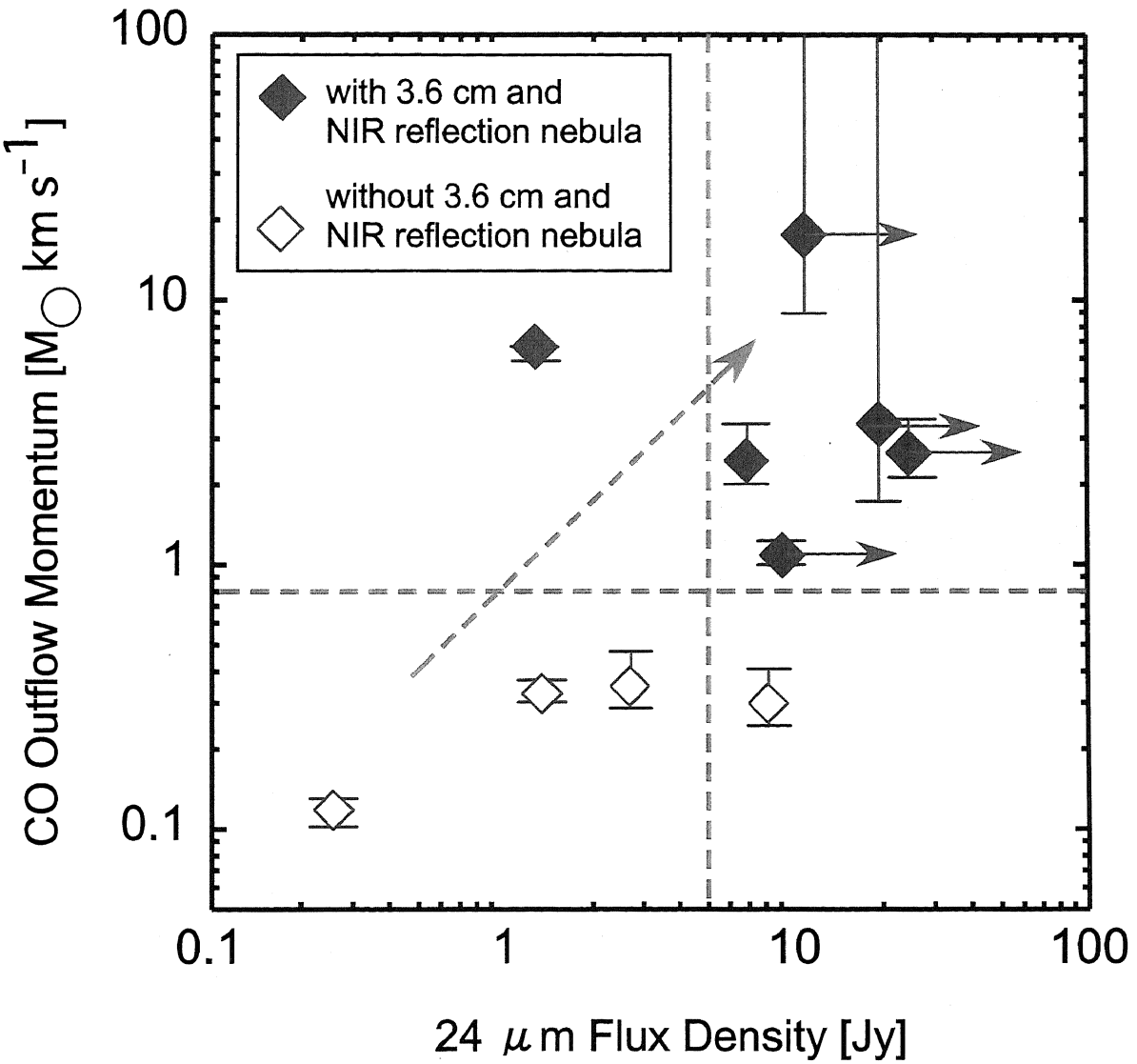

Fig. 14.— The outflow momentum rates derived by CO data plotted as a function of the centimeter luminosities. Blue and black circles show the data in OMC-2/3 and Taurus, respectively. Centimeter luminosities of these sources are masured from the 3.6 cm VLA observations. Taurus data were refered from Hogerheijde et al. (1998) and Saito et al. 2006 in private communication. Red circles show the data of other low- to intermediate mass protostars (Anglada et al. 1995). Centimeter luminosities of these sources are masured from the 6.0 cm VLA observations. Doted line shows the best fit by Anglada et al. (1995).

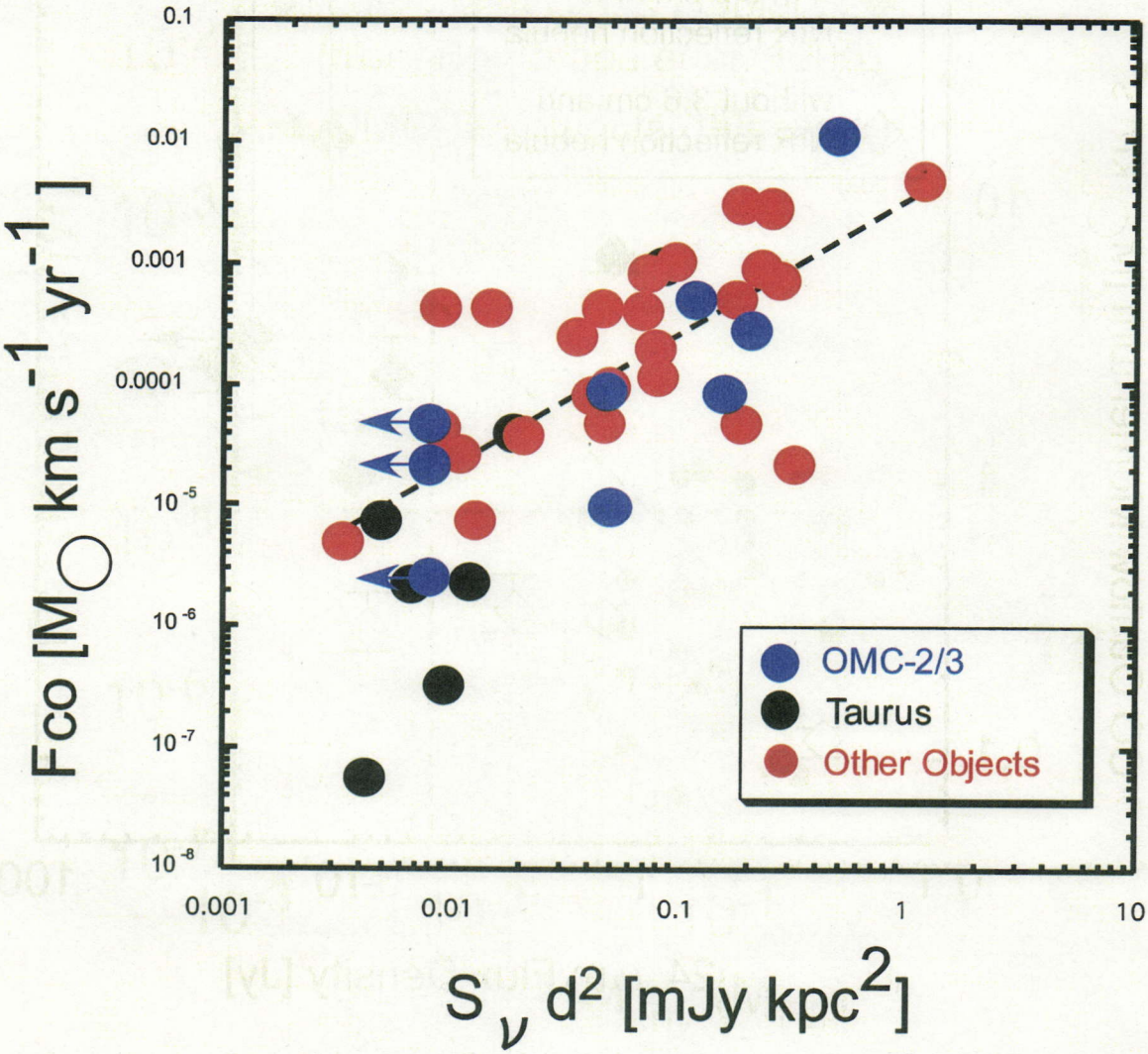

Fig. 15.— The outflow momentum derived by CO(3–2) emission plotted as a function of the 24 μm peak flux taken with the Spitzer/MIPS. Filled and open circles show presence and absence of the 3.6 cm continuum emission, respectively.

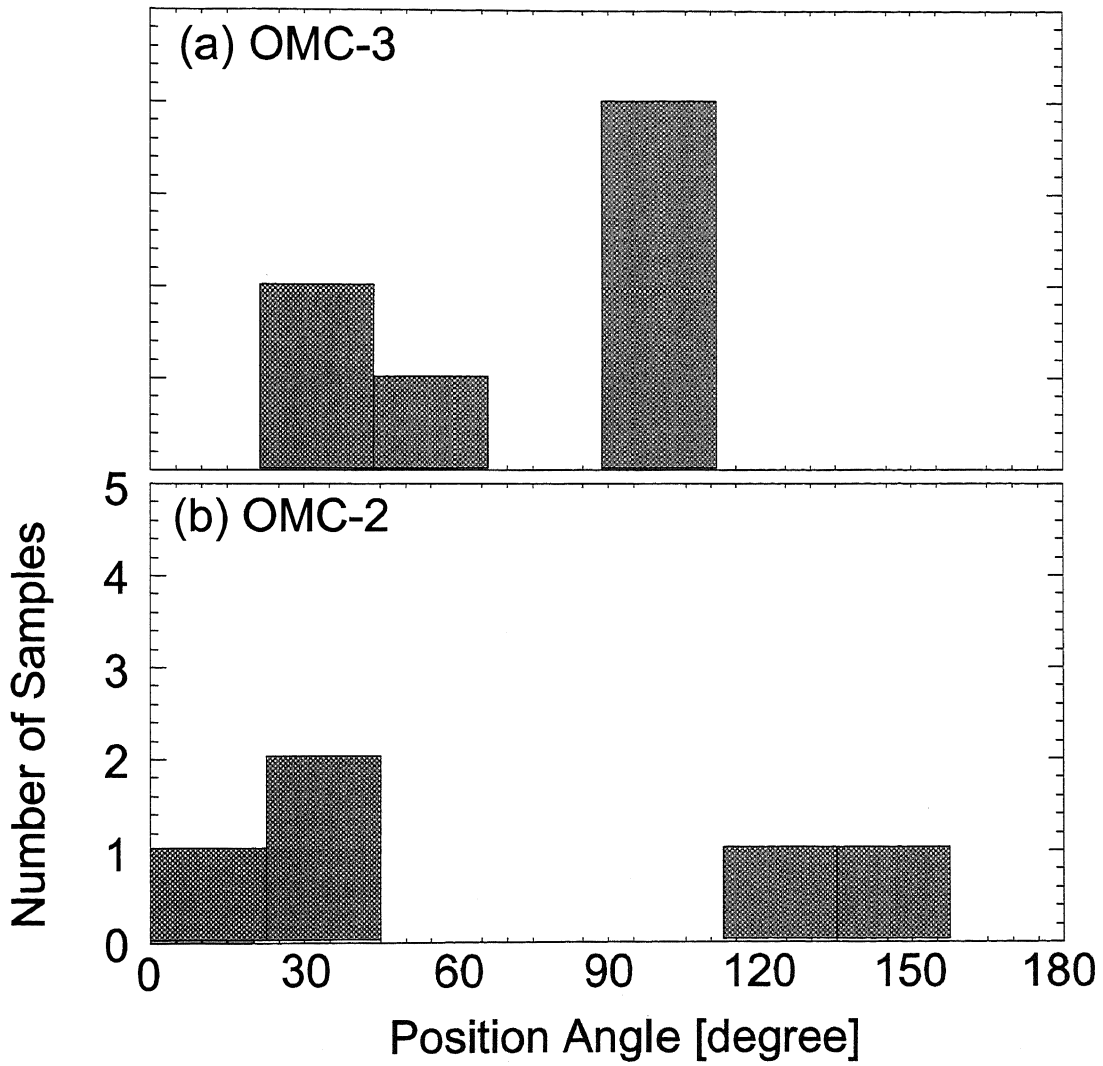

Fig. 16.— Distribution of the outflow position angles.

Table 1. Centimeter and sub millimeter continuum sources in the OMC-2/3 region

ID	R.A. (J2000)	Dec. (J2000)	1300 μm[a]	350 μm[b]	3.6 cm[c]	24 μm[d]	Comments
1	05 35 30.2	-04 58 48.0	SIMBA *a*	CSO 1	—	053530-045848	
2	05 35 29.7	-04 58 06.0	SIMBA *b*	—	—	—	
3	05 35 28.2	-04 58 40.0	SIMBA *c*	—	—	053528-045838	
4	05 35 28.6	-04 57 48.0	SIMBA *d*	—	—	—	
5	05 35 30.6	-04 59 49.0	SIMBA *e*	—	—	—	A bright 24 μm source (SP 053531-045936) is located at $\sim 15''$ north of the dust cond
6	05 35 35.1	-04 59 24.5	—	CSO 2	—	—	
7	05 35 15.8	-04 59 58.7	—	CSO 3	—	053516-050003	Binary
8					—	053515-050009	
9	05 35 17.1	-05 00 02.8	—	CSO 4	—	—	
10	05 35 18.0	-05 00 19.8	MMS 1	CSO 5	—	—	
11	05 35 18.3	-05 00 34.8	MMS 2	CSO 6	VLA 1	053518-050034	Binary (from Nielbock et al. 2003)
12	05 35 19.2	-05 00 51.2	MMS 3	CSO 7	—	053519-050051	
13	05 35 20.5	-05 00 53.0	MMS 4	CSO 8	—	—	A faint 24 μm source (SP 053520-050103) is located at $\sim 15''$ SW of MMS 4
14	05 35 22.4	-05 01 14.1	MMS 5	CSO 9	—	053522-050115	
15	05 35 23.5	-05 01 32.2	MMS 6	CSO 10	VLA 3	053524-050130	Multiple system ?
16					—	053524-050140	
17	05 35 27.2	-05 03 38.5		CSO 11	—	—	
18	05 35 26.4	-05 03 53.4	MMS 7	CSO 12	VLA 4	053527-050355	A bright reflection nebula, Haro- 5a/6a (from Haro 1953).
19	05 35 26.5	-05 05 17.4	MMS 8	CSO 13	—	—	
20	05 35 26.0	-05 05 42.4	MMS 9	CSO 14	VLA 5	053526-050546	Extended 24 μm source. Binary or disk like structure ?
21	05 35 32.3	-05 05 41.8	MMS 10	—	—		Another 24 μm source (SP 053532-050545) is located at the $\sim 10''$ SW from MMS 10
22	05 35 25.6	-05 07 57.4	—	—	VLA 9	053526-050758	Located at the edge of the OMC-2 dust filament.
23	05 35 22.9	-05 06 41.2	—	CSO 15	—	—	
24	05 35 23.7	-05 07 10.2	FIR 1*c*	CSO 16	VLA 7	—	Extended 24 μm cm source.
25	05 35 23.4	-05 07 32.2	FIR 1*b*	CSO 17	—	—	
26	05 35 24.6	-05 07 53.3	FIR 1*a*	CSO 18	VLA 8	053524-050753	Faint 24 μm source.
27	05 35 24.7	-05 12 33.3	—	CSO 19	—	—	
28	05 35 24.3	-05 08 33.3	FIR 2	CSO 20	—	053524-050831	
29	05 35 26.5	-05 08 25.4	—	CSO 21	—	—	
30	05 35 27.5	-05 09 32.5	FIR 3	CSO 22	VLA 11	053528-050935	A 24 μm source (SP 053527-050923) is located at $\sim 10''$ NW from FIR 3.
31	05 35 26.7	-05 10 00.4	FIR 4	CSO 23	VLA 12	053527-051002	Mm/sub-mm and 24 μm sources do not coincide with the cm source.
32	05 35 24.8	-05 10 29.5	—	—	VLA 13	053525-051031	Bright cone-like NIR feature.
33	05 35 26.4	-05 10 23.4	FIR 5	CSO 24	—	053527-051017	A bright 24 μm source located at $\sim 10''$ NE from FIR 5.
34	05 35 26.3	-05 12 23.4	—	CSO 26	—	—	

Table 1—Continued

ID	R.A. (J2000)	Dec. (J2000)	1300 μm[a]	350 μm[b]	3.6 cm[c]	24 μm[d]	Comments
35	05 35 24.7	-05 12 33.3	—	CSO 27	—	—	
36	05 35 23.4	-05 12 36.2	FIR 6*a*	CSO 28	—	—	
37	05 35 21.7	-05 12 13.1	—	—	VLA 14	—	
38	05 35 23.4	-05 12 03.2	FIR 6*b*	CSO 25	—	053523-051205	
39	05 35 21.5	-05 13 15.1	FIR 6*c*	CSO 29	—	—	
40	05 35 20.0	-05 13 14.9	FIR 6*d*	CSO 30	—	053520-051314	
41	05 35 21.5	-05 14 30.1	No obs.	CSO 31	—	—	
42	05 35 21.3	-05 14 54.0	No obs.	CSO 32	—	—	
43	05 35 19.5	-05 15 34.9	No obs.	CSO 33	—	053520-051533	Extended 24 μm source ?

[a]Millimeter source names in the column are from Chini et al. (1997) and Nielbock et al. (2003).

[b]Sub-mm source names in the column are from Lis et al. (1998).

[c]Centimeter source names in the column are from Reipurth et al. (1999).

[d]We identified 24 μm sources using the archive data taken by SPITZER/MIPS with the IRAF apphot package .

Table 2. IDENTIFICATION OF THE CO(3-2) OUTFLOWS

ID	Object name[a]	Identification	Map	Wing Profile	NIR features	Comments
1	SIMBA *a*	C	BR	No		
2	SIMBA *b*	No	No	No		
3	SIMBA *c*	P	BR?	No	[1]	Faint reflection nebula, monopolar flow ?
4	SIMBA *d*	No	No	No		
5	SIMBA *e*	No	No	No		
6	CSO 2	M	BR	No		No Gaussian line profile, May trace a part of motion of large scale cloud gas
7,8	CSO 3	No	No	No		
9	CSO 4	No	No	No		
10	MMS 1	No	No	BR		
11	MMS 2	C	BR	BR	[2], [3], [4]	Corresponding to "flow B"[b] , nearly plane of the sky
12	MMS 3	No	BR	BR		
13	MMS 4	No	BR	B		
14	MMS 5	C	BR	BR	[5]	Corresponding to "flow C"[b] , H_2 chain of knots
15,16	MMS 6	M ?	R	No	[6]	Faint jet like feature in the NIR image associated with SP 053524-050130
17	CSO 11	No	B	No		
18	MMS 7	C	BR	BR	[7]	Corresponding to "flow F"[b] , nearly plane of the sky
19	MMS 8	No	BR	B		
—	UD -1	P	—	B	[8]	The driving source candidate is SP 053526-050545 (i.e. MMS 9) or SP 053526-050558
20	MMS 9	C	BR	BR	[9], [10], [11]	Corresponding to "flow H"[b]
21	MMS 10	No	No	No		
22	VLA 9	P	B	No	[13]	Monopolar flow, no mm/sub-mm counterparts
23	CSO 15	No	No	B		
24	FIR 1*c*	No	B	B		
25	FIR 1*b*	M	R	R		
26	FIR 1*a*	No	R	R		
28	FIR 2	C	BR	BR		
30	FIR 3	C	BR	BR	[14]	"Butterfly-like" velocity structure
—	MIR 20	M	—	B	[15]	There is 24 μm source, SP 053527-050923, and no mm/submm and cm sources, Bright NIR jet
31	FIR 4	M ?	BR	BR	[16]	Faint reflection nebula ?
32	VLA 13	C	BR	BR	[17]	Bright NIR feature
33	FIR 5	No	BR	R		
34	CSO 26	No	No	No		
35	CSO 27	No	No	No		
36	FIR 6*a*	No	No	R		

Table 2—Continued

ID	Object name[a]	Identification	Map	Wing Profile	NIR features	Comments
37	VLA 14	No	B	B		
38	FIR 6*b*	C	BR	R		
39	FIR 6c	P	BR	R		
40	FIR 6*d*	No	No	R	[18]	
41	CSO 31	No	No	No		
42	CSO 32	M ?	R	R		Difficult to distinguish the origin of emission outflow and shock from HII region
43	CSO 33	P	B	R	[19]	Difficult able to distinguish the origin of emission outflow and shock from HII region

[a]Object names from Chini et al. (1997), Nielbock et al. (2003), Lis et al. (1998) and Reipurth et al. (1999)

[b]Flows were identified in the 2.12 μm $v = 1$–0 $s(1)$ H_2 line emission (Yu et al. 1997)

Table 3. CO(3-2) OUTFLOW PARAMETERS

ID	Object name[a]	inclination[b] (deg)	P.A. (deg)	V_{max}[c] (km s^{-1})	R_{max}[c] (pc)	M_{CO}[d] ($M_\odot$)	t_d[e] (yr)	$\dot{M}_{CO}$[e] ($M_\odot$ yr^{-1})	F_{CO}[e] ($M_\odot$ km s^{-1} yr^{-}
				Blue lobe					
1	SIMBA *a*	30	50	4.7	1.2E-01	2.2E-02	4.2E+04	5.1E-07	2.8E-06
11	MMS 2	30	90	9.9	6.2E-01	9.5E-02	1.1E+05	8.9E-07	1.0E-05
14	MMS 5	30	-90	9.7	8.4E-02	3.0E-02	1.5E+03	2.0E-06	2.3E-05
18	MMS 7	80	90	6.0	2.2E-01	9.9E-02	6.3E+03	1.8E-05	5.4E-04
20	MMS 9	40	-100	15.6	1.0E+00	3.3E-01	7.6E+04	4.4E-06	8.9E-05
22	VLA 9	—	40	9.4	3.7E-01	1.5E-01	2.7E+04	5.6E-06	9.2E-05
28	FIR 2	—	-150	10.0	1.0E-01	2.0E-02	6.9E+03	2.9E-06	5.0E-05
30	FIR 3	80	30	20.7	1.9E-01	1.6E-01	1.5E+03	1.1E-04	1.2E-02
32	VLA 13	—	0	6.6	8.4E-02	2.3E-01	8.7E+03	2.6E-05	3.0E-04
38	FIR 6*b*	—	-115	9.0	1.7E-01	1.9E-02	1.3E+04	1.5E-06	2.3E-05
				Red lobe					
1	SIMBA *a*	30	50	4.0	1.4E-01	7.7E-03	5.7E+04	1.3E-07	6.2E-07
11	MMS 2	30	90	5.3	2.4E-01	5.3E-02	7.5E+04	7.0E-07	4.3E-06
14	MMS 5	30	-90	10.9	1.0E-01	1.9E-02	1.6E+04	1.2E-06	1.5E-05
18	MMS 7	80	90	8.0	9.8E-01	2.4E-01	2.1E+04	1.1E-05	5.3E-04
20	MMS 9	40	-100	14.7	7.1E-01	3.3E-01	5.6E+04	5.9E-06	1.1E-04
22	VLA 9	—	40	—	—	—	—	—	—
28	FIR 2	—	-150	9.5	6.8E-02	2.3E-02	4.9E+03	4.7E-06	7.8E-05
30	FIR 3	80	30	12.8	1.7E-01	8.5E-02	2.3E+03	8.4E-05	6.0E-03
32	VLA 13	—	0	6.3	6.8E-02	7.0E-02	7.3E+03	9.6E-06	1.1E-04
38	FIR 6*b*	—	-115	7.2	3.2E-01	1.5E-01	3.0E+04	4.9E-06	6.2E-05

[a]Object names in the column are from Chini et al. (1997), Lis et al. (1998), Nielbock et al. (2003) and Reipurth et al. (1999).

[b]Inclinations of SIMBA *a*, MMS 2 and MMS 5 were derived from the ratio of major and minor axis of dense envelope (Takah et al. in prep.), and incrinations of MMS 7 and FIR 3 were assumed nearly plane of the sky (i.e., 80°), and that of other objects w adopted a median value (i.e., 55 °).

[c]Not corrected for inclination.

[d]Assuming T_{ex} = 60 K (Hogerheijde et al. 1998) and X[CO]=10^{-4} (Frerking, Langer & Wilson 1982).

[e]Each parameter was derived from considering assumed inclination angle.

Table 4: MEDIAN OF CO(3-2) OUTFLOW PARAMETERS associated with the OMC-2/3 and Taurus protostars[a]

	OMC-2/3	Taurus[a]
M_{CO} ($M_\odot$)	7.7E-02	1.0E-03
$\dot{M}_{CO}$ ($M_\odot$ yr^{-1})	5.8E-06	4.4E-07
F_{CO} ($M_\odot$ km s^{-1} yr^{-1})	1.0E-04	3.2E-06

[a]Refereed from Hogerheijde et al. (1998).

Chapter IV

NMA survey of $H^{13}CO^+(1–0)$ and Dust Continuum Emission around Intermediate-mass Protostars in the Orion Molecular Cloud -2 and -3 Regions

1. Introduction

Study of the formation and evolution of intermediate-mass protostars ($2 \leq M_* \leq 8\ M_\odot$) will allow us to understand whether the low-mass star-formation scenario is applicable to more massive star-formation. Although there are many millimeter and infrared observations of Herbig Ae/Be stars (e.g., Hillenbrand 1995, Fuente et al. 2002), evolution of protostellar phase of intermediate-mass protostars are still unclear. In order to understand the formation and evolution of intermediate-mass protostars, it is important to directly investigate the accretion and dissipation (or destruction) processes of dense gas envelopes around intermediate-mass protostars. For these purposes, we have performed multi-wavelength and multi-line survey observations toward intermediate-mass pre- and proto-stellar candidates in the Orion Molecular Cloud -2/3 region (OMC-2/3; $D\sim$ 450 pc; Chini et al. 1997). The OMC-2/3 region is one of the best target to investigate evolution of intermediate-mass protostars systematically, because all of the sources are in the same distance and under the similar (chemical) environment.

In this chapter, we will show the results of NMA survey observations toward 12 intermediate-mass pre- and proto-stellar candidates in OMC-2/3 in the $H^{13}CO^+$ emission and 3.3 mm continuum emission. The $H^{13}CO^+$ (1–0) molecular line is one of the most appropriate tracers of cold dense gas ($n \sim 10^5$ cm^{-3}) as discussed in Chapter 2. For example, results of $H^{13}CO^+$(1-0) observations of dense envelopes in the Taurus Molecular Cloud complex have suggested that the dense gas traced by the $H^{13}CO^+$ emission dissipates as protostars evolve from Class 0 to Class I (Saito et al. 2001).

2. The Sample

For our survey, we selected 23 dust condensations along the northern part of the OMC-integrate shaped filament, which are discovered by the observations of the 1.3 mm continuum emission taken with the IRAM 30 m telescope and the Swedish-ESO Submillimeter Telescope; SEST (Chini et al. 1997, Nielbock et al. 2003). These sources corresponding to a part of objects of 43 sources mentioned Chapter III (see Table III-1). In this thesis, the author will show results of 12 embedded sources of them, i.e., all the OMC-3 samples and FIR 2 in the OMC-2 region. My collaborator is working on other 11 samples as mentioned in Section 3.1. These samples have a bolometric luminosity of 55 - 157 $L_\odot$ and mass of dust condensations of 8 – 36 $M_\odot$ (Chini et al. 1997), which are typically more than one order of magnitude larger than low-mass counterparts, suggesting the formation of A0 like star at the zero-age main sequence (ZAMS). The OMC-2/3 region is one of the best targets to conduct a systematic survey of intermediate-mass protostars, because all of the sources are in the same distance and under the similar (chemical) environment. The observed sources are listed in Table 1.

3. Observations and Data Reductions

3.1. NMA Observations

We have observed the $H^{13}CO^+$ (J=1–0; 86.754 GHz) emission and the 3.3 mm continuum emission toward 23 millimeter sources in the OMC-2/3 region identified by Chini et al. (1997)

and Nielbock et al. (2003) with the six-elements NMA from 2004 November to 2006 May. For all sources in our samples, field center was set to be the 13 peak positions of the 1.3 mm dust emission. The field center is denoted by blue and red circles in Figure I-3. Since the sources with red circles in Figure I-3 have been observed by the other collaborator, in this thesis the author only demonstrates the data of the eight field of views denoted by the blue circles in Figure I-3. * The NMA observational parameters are summarized in Table 2. Since the minimum projected baseline length of the $H^{13}CO^+$(1–0) observations was approximately 3.0 kλ, our observations were insensitive to structures more extended than 57″ (0.13 pc) at the 10% level (Wilner and Welch 1994). The overall flux uncertainty was estimated to be $\sim$ 15 percent. After the calibrations, we made final images only from the data taken under good weather conditions. We have CLEANed the $H^{13}CO^+$ images with a natural weighting by using Astronomical Image Processing System (AIPS) developed at NRAO

The 3.3 mm continuum data with the D, C, and AB configurations was obtained simultaneously with the $H^{13}CO^+$ data by using a digital spectral correlator UWBC (Okumura et al. 2000), which has 128 frequency channels and a 1024 MHz bandwidth per baseline. Both the lower (87 $\pm$ 0.512 GHz) and upper (99 $\pm$ 0.512 GHz) sidebands were obtained simultaneously with a phase-switching technique. To obtain a higher signal-to-noise ratio, the data of both sidebands were added and averaged (effective frequency = 92.754330 GHz). We have CLEANed the continuum data with a uniform weighting. Table 2 and 3 provide a list of the relevant observational parameters for the $H^{13}CO^+$ emission and continuum emission.

3.2. The 45 m Telescope Observations

Single-dish mapping observations in the $H^{13}CO^+$ (1-0) line were also conducted with the 5×5 SIS array receiver BEARS equipped in the 45-m telescope on 2005 January and April. Observational parameters of the 45 m telescope are summarized in Table 4. We observed the 190″ × 190″ area (corresponding to 0.43 pc×0.43 pc) centered on the SIMBA a, MMS6, MMS 7 and MMS 10 with a grid spacing of 8″.2. The temperature scale was determined by a chopper-wheel method, which provides us the antenna temperature corrected for the atmospheric attenuation. As a backend, we used an auto correlator with a frequency resolution of 31.12 kHz, corresponding to 0.11 km s^{-1} at the $H^{13}CO^+$ frequency. We applied scaling factors to correct for variations of the gain and the DSB ratio in each beam, which were measured by the Nobeyama Radio Observatory and the typical value was $\sim$1.5.

3.3. Archive Data: Spitzer/MIPS in OMC-2/3

We have also fetched archived 24 μm data obtained by infrared camera MIPS (Multiband Imaging Photometer) equipped in the 0.85 m infrared space telescope Spitzer (formerly SIRTF, the Space Infrared Telescope Facility). The field of view and spatial resolution of the 24 μm band are 5′.4 × 5′.4 (covering the entire region of OMC-2/3) and 5.8″, respectively. We identified 24 μm sources along the OMC filament using the IRAF apphoto package, although emissions from

*Detailed results and discussion of the other fields of view (denoted by red circles) will be the subject to a Master thesis by Y. Shimajiri (University of Tokyo, Japan).

several sources are saturated and the position of those sources cannot be well-determined. Hence, we consider that the positional fitting to the 24 μm sources contains errors on the order of the pixel size, $\sim 2''.45$. Table 5 summarizes the identified 24 μm sources associated with the 1.3 mm sources.

4. Results and Analyses

4.1. Continuum Emission taken with the NMA

Figure 3(b) - 11(b) show 3.3 mm continuum emission observed with the NMA toward our target sources. We have detected the intense 3.3 mm continuum emission toward the eight 1.3 mm sources, SIMBA a, MMS 1, MMS 2, MMS 5, MMS 6, MMS 7, MMS 9 and FIR 2. The expected flux density from the free-free emission at this wavelength is less than 5 % based on the 3.6 cm flux density of 0.15 to 0.79 mJy in the case of the optically thick free-free emission (Reipurth et al. 1999), indicating that the origin of the 3.3 mm continuum emission is mostly the thermal dust emission. Then, we will neglect the free-free contamination to the 3.3 mm continuum flux in following section. We estimated the total mass of the gas and dust associated with the 3.3 mm continuum emission as follows,

$$M_{\rm H_2} = \frac{F_\lambda d^2}{\kappa_\lambda B_\lambda(T_{\rm dust})}, \qquad \text{(IV.1)}$$

where κ_λ is the mass-absorption coefficient of dust grains of 0.037 cm^2 g^{-1} (λ / 400 μm)$^{-\beta}$ (Ohashi et al. 1996). The values of β was determined by the flux densities at 350 μm and 1300 μm (Chini et al. 1997, Lis et al. 1998) with a power law fitting, $F_\nu \propto \nu^{(2+\beta)}$. The dust temperature, $T_{\rm dust}$, was referred from previous studies (Chini et al. 1997, Cesaroni et al. 1989). B_λ is the Planck function, F_λ is the total flux density of the continuum emission, and d is the distance to the object, 450 pc in OMC-2/3 (Genzel & Stutzki 1989). We summarize peak positions of the 3.3 mm sources, total fluxes, dust temperatures and mass of the dusty envelopes in Table 7. We note that several detected 3.3 mm sources taken with the NMA appear to be shifted from the 1.3 mm sources by a few arcsec. However, these offsets can be explained by the positional error of the 1.3 mm observations ($\pm$ 5$''$) by Chini et al. (1997).

4.2. Line Profiles taken with the 45 m Telescope and Physical Properties of the Dusty Condensations

Figure 1 shows $H^{13}CO^+$(1–0) spectra taken with the 45 m telescope toward the 11 peak positions of the 3.3 mm continuum emission observed with the NMA in the OMC-3 region [†] . We fitted multiple-Gaussians to the $H^{13}CO^+$ (1–0) spectra and obtained the systemic velocity in $V_{\rm LSR}$, peak brightness temperature in T_B, and the FWHM velocity width for each velocity component. We also estimated the virial mass of the dusty condensations in the 1.3 mm continuum emission, using the following formula,

[†]We did not observe the $H^{13}CO^+$ line at FIR 2.

$$M_{\rm vir} = \frac{5RC_{\rm eff}^2}{G}, \tag{IV.2}$$

where

$$C_{\rm eff}^2 = \frac{\Delta v_{\rm obs}^2}{8ln2} + kT_k\left(\frac{1}{m} - \frac{1}{m_{\rm obs}}.\right) \tag{IV.3}$$

$M_{\rm vir}$ is a virial mass, R is a radius (geometrical mean) of the 1.3 mm dust condensations (Chini et al. 1997, Nielbock et al. 2003), $C_{\rm eff}$ is a effective sound speed of gas with a mean molecular weight m of 2.33, $\Delta v_{\rm obs}$ is a observed $H^{13}CO^+$ line width measured at the peak position of the dust condensation. In the case of multiple velocity components in the $H^{13}CO^+$ profile, we adopted the velocity component which is also seen in the NMA $H^{13}CO^+$ observations and hence is likely to be associated with the protostar. T_k is a kinetic temperature of gas. G and k is a gravitational- and Boltzmann-constant, respectively. We adopted the kinetic temperature, T_k, estimated by the SED. Table 6 provides a list of above parameters.

Based on the derived physical parameters, we investigated physical properties of dust condensations detected in the 1.3 mm observations. Figure 2 shows the derived virial mass plotted as a function of the mass estimated from the 1.3 mm continuum emissions (Chini et al. 1997). The virial mass of all cores except for MMS 7 (see Figure 2) is smaller than (or simillar to) the mass derived from the dust emissions, suggesting that the dust condensations detected by 1.3 mm emission are gravitationally bound. Hence, these cores are likely to be in the course of star formation. On the other hand, one of the dusty condensations, MMS7, shows a relation of $M_{\rm vir} > M_{\rm dust}$, suggesting gravitationally unbound. This is because our observational results shown in Chapter 2 suggest that MMS 7 is in later evolutionary phase of the protostellar core and that dense gas is already being dissipated. In addition, there is no obvious difference of the $M_{\rm vir} - M_{\rm dust}$ relation, regardless of the presence or absence of the 3.3 mm compact continuum source taken with the NMA.

4.3. $H^{13}CO^+$ (1–0) Envelopes taken with the NMA

We detected the $H^{13}CO^+$(1–0) emission with the NMA toward all the 1.3 mm sources. Specifically, ten out of twelve 1.3 mm sources, SIMBA a, MMS 1, MMS2, MMS 3, MMS5, MMS6, MMS 7, MMS 8, MMS 10, and FIR 2, are accompanied with a significant $H^{13}CO^+$ emission. Table 8 summarizes physical properties of the $H^{13}CO^+$(1–0) emission taken with the NMA. The total flux densities and sizes of the $H^{13}CO^+$ emission were measured above 3σ level. Assuming that the $H^{13}CO^+$ emission is optically thin and the distribution of the excitation temperature is uniform, we estimated the LTE mass following eq. (2) in Chaprter II. We adopted $T_{\rm ex}$ = 20 K which is a similar to the large-scale temperature in OMC derived from NH_3 and dust emissions (Cesaroni et al 1994, Chini et al. 1997), and the $H^{13}CO^+$ abundance of 1.4×10^{-10}, which is derived from the comparison between the estimated $H^{13}CO^+$ column density and the $C^{18}O$ column density (Chini et al. 1997).

4.4. Individual Source

In this section, we will describe nature of individual sources except for MMS 7 (See in Chapter 2).

4.4.1. SIMBA a

The OMC-3 SIMBA complex was identified from the 1.2 mm single-dish observations by Nielbock et al. (2003). This complex has also been identified by previous CS(1–0) and $H^{13}CO^+$ observations, and the mass of this complex is estimated to be 140 $M_\odot$ by CS (1–0) observations (Tatematsu et al. 1993, Aso et al. 2000). The SIMBA complex contains five dust condensations. One of the brightest 1.2 mm sources, "SIMBA a", has also been identified by submillimeter dust-continuum observations as CSO 1 (Lis et al. 1998, Johnstone & Bally 1999). The dust temperature and estimated mass are 11 K and 24 $M_\odot$ (Nielbock et al. 2003). A 0.1 pc scale outflow was detected by our submillimeter CO(3-2) observations with ASTE for the first time.

The 3.3 mm dust continuum emission is detected roughly 5″ south-west of the 1.2 mm peak position as shown in Figure 3*b*. The peak position of the 3.3 mm dust emission coincides with that of the 24 μm Spitzer source within the positional error, suggesting a presence of the heating source. We newly detected a CO(1–0) outflow with a size scale of 0.1 pc centered on the 3.3 mm dust continuum peak from our NMA observations (See Figure 3*a*). The velocity range of the wing component in the CO(1–0) emission [$V_{\rm LSR}$ = 9.8 – 11.4 km s^{-1} in blue, 13.8 – 15.2 km s^{-1} in red] is almost same as that of the previously detected CO (3–2) emission [$V_{\rm LSR}$ = 7.8 – 10.0 km s^{-1} in blue, 14.3 – 16.5 km s^{-1} in red] observed with ASTE (See Figure 2 in Chapter 3).

The $H^{13}CO^+$ spectrum taken with the 45 m telescope toward SIMBA a has a double-peaked profile (See Figure 1*a*), suggesting the presence of the overlaying two components along the line of sight with a systemic velocity of 11.8 and 12.7 km s^{-1}. Figure 3*a* and *c* show a total integrated intensity map of the $H^{13}CO^+$ emission from each component toward SIMBA a, over the velocity range of $V_{\rm LSR}$ = 12.2 – 13.8 and 11.4 km s^{-1} – 12.1 km s^{-1}, respectively. The $H^{13}CO^+$ emission shown in Figure 3*a* (hereafter called core(1)) has a condensed structure, whose peak position coincides with the 3.3 mm dust emission. On the other hand, the $H^{13}CO^+$ emission shown in Figure 3*c* is less centrally condensed (hereafter called core (2)) at the 3.3 mm peak position. Furthermore, the velocity width (in FWHM) of the $H^{13}CO^+$ emission toward core (1), 1.13 km s^{-1}, is larger than that toward core (2), 0.53 km s^{-1}. These results imply that the 3.3 mm dust emission associated with the $H^{13}CO^+$ core (1) is already forming a star, where $H^{13}CO^+$ core (2) is not associated with the compact 3.3 mm source. We interpret these results as that the core (1) is a protostellar core with a protostar, and core (2) is a pre-stellar core without any siguniture of a heating source. Core (1) has an elongated disk-like structure which is approximately perpendicular to the CO outflow axis. The mass and size of the $H^{13}CO^+$ emission toward this protostellar core are 1.65 $M_\odot$, 16600 × 8600 AU with a position angle of - 25°, respectively. On the other hand, core (2) shown in Figure 3*c* has relatively extended structure with a mass of 0.57 $M_\odot$ and a size of 11300 × 4500 AU scale.

Figure 12*a* shows a P-V diagram of SIMBA a along the major axis. We see a $H^{13}CO^+$ emission originated from Core(1) and Core(2), respectively. Two bright blue- and redshifted $H^{13}CO^+$ peaks are seen in core(1), possibly indicating the rotating motion. Figure 12*b* shows a P-V diagram along the minor axis. The peak position of the $H^{13}CO^+$ emission originated from

Core (1) is located at the 3.3 mm emission peak with a velocity range of 13.2 – 13.3 km s^{-1}. The core has a maximum velocity width ($\sim$ 1 km s^{-1}) at the 3.3 mm position. We did not detect clear radial motion such as accretion or dissipation in core(1). In addition, in core (2), we did not detect clear rotating motion along the major axis.

4.4.2. MMS 1

MMS 1 is located at the most northern part of the OMC-3 region (Chini et al. 1997). This source is also detected by 350 μm continuum observations as CSO 5. The mass and bolometric luminosity of the dust condensation are 18 $M_{\odot}$ and < 55 $L_{\odot}$, respectively (Chini et al. 1997). The bolometric luminosity to submillimeter flux ratio is $L_{\rm bol}/L_{\rm smm} < 61$, suggesting class 0-type SED (Andre et al. 1993). There is no infrared source nor any signature of CO outflow/jet in this region.

The peak position of the 3.3 mm dust emission with the NMA is roughly 3″-north shifted from the 1.3 mm peak position as shown in Figure 4*b*. The mass of the 3.3 mm dust condensation is 0.54 – 1.96 $M_{\odot}$, and the 3.3 mm emission is elongated with a positional angle of 45°. Figure 4*a* shows the $H^{13}CO^{+}$ total intensity map with a velocity range of 11.1 – 12.2 km s^{-1}. The peak position of the $H^{13}CO^{+}$ emission shifts North-West from the 3.3 mm emission peak. On the other hand, the $H^{13}CO^{+}$ emission taken with the 45 m telescope has a double-peaked line profile at MMS 1 (See Figure 1*b*) with a systemic velocities of 10.8 and 11.5 km s^{-1}, respectively. We consider that the component with a systemic velocity of 10.8 km s^{-1} is originated from MMS 2, located at 20″ South-East from MMS 1. The component with a systemic velocity of 11.5 km s^{-1} is likely to be associated with MMS 1.

Figure 13 shows a P-V diagram of MMS 1 along the major axis of the $H^{13}CO^{+}$ envelope. We detected two $H^{13}CO^{+}$ components with a velocity range of 10.1 –11.0 km s^{-1} and 11.1 – 12.3 km s^{-1}. The former component is likely to be contamination from MMS 2 as mentioned above. The latter component, associated with the 3.3 mm source of MMS 1, show a velocity gradient (denoted by blue dashed line in Figure 13) centered on the 3.3 mm emission peak, possibly suggesting a rotation of the envelope.

4.4.3. MMS 2

The millimeter source MMS 2 is also identified as a 350 μm source CSO 6 (Chini et al. 1997, Lis et al. 1998). This source contains a MIR binary system. The projected separation of the two components is 570 AU with a position angle of 45 °, and this binary system is surrounded by extended emission at 10.4 μm (Nielbock et al. 2003). The NIR color show a large excess of $H - K \sim 4$ and the spectral index suggests that both components are Class I (Tsujimoto et al. 2002, Nielbock et al. 2003). MMS 2 also coincides with the X-ray source (source 8; Tsuboi et al. 2001). The X-ray spectrum shows evidence of two different sources, which consists of soft X-ray emission as T Tauri stars and hard X-ray emission characteristic for outflow/jet, (Tsuboi et al. 2001, Tsujimoto et al. 2004). Jet-like features, knots and an 1 pc scale outflow were detected in our CO(3–2) observations, previous CO(1–0) and JHK (or K_s) observations (Yu et al. 1997, Aso et al. 2001, Stanke et al. 2000, Williams et al. 2003, Tsujimoto 2004). There is also free-free jet traced by the 3.6 cm VLA source at MMS 2 (Reipurth et al. 1999, Tsujimoto et al. 2004).

The 3.3 mm source taken with the NMA and 24 μm Spitzer source [‡] coincide with the 1.3 mm peak position as shown in Figure 5*b*. The $H^{13}CO^+$ emission taken with the 45 m telescope has a double-peaked line profile at MMS 2 with a systemic velocity of 10.7 and 11.4 km s^{-1}, respectively (See Figure 1*c*). Since the stronger peak at V_{LSR} = 11.4 km s^{-1} has a same systemic velocity as that of MMS 3 (see next subsection), there seems to be contamination to the $H^{13}CO^+$ emission from MMS 3. The weaker peak at V_{LSR} = 10.7 km s^{-1} is associated with the millimeter source MMS 2. Figure 5*a* shows a total intensity map of the $H^{13}CO^+$ emission toward MMS 2, over the velocity range of V_{LSR} = 10.5 – 11.1 km s^{-1}. The $H^{13}CO^+$ emission is elongated to the north-south direction, which is perpendicular to the associated outflow direction. The mass and size of the $H^{13}CO^+$ envelope are 0.95 $M_\odot$ and 13200 × 6600 AU with a position angle 0°, respectively. The peak position of the $H^{13}CO^+$ emission is located at a few arcsec east from the 3.3 mm dust position.

Figure 14*a* shows a P-V diagram of MMS 2 along major axis. The main $H^{13}CO^+$ emission is centered on the 3.3 mm continuum emission. There is no clear velocity gradient in the $H^{13}CO^+$ envelope around MMS 2. Figure 14*b* shows a P-V diagram along the minor axis. Two kinds of $H^{13}CO^+$ components are seen in the P-V diagram; one is the main $H^{13}CO^+$ envelope associated with the 3.3 mm emission around the systemic velocity of 10.7 km s^{-1}, and the other not associated with the 3.3 mm emission in the velocity range of 10.0 –10.4 km s^{-1} and 11.3 – 11.8 km s^{-1}, respectively (denoted by two dashed circles in Figure 14*b*). The latter components show the same velocity gradient as that of the CO(3–2) outflow (i.e., red- and blueshifted components locate in west and east, respectively), suggesting that the dense gas is being dispersed by the CO outflow.

4.4.4. MMS 3 and MMS 4

Millimeter source MMS 3 and MMS 4 are also identified as 350 μm sources of CSO 7 and CSO 8, respectively (Lis et al. 1998). The mass and bolometric luminosity of MMS 4 are 11 $M_\odot$ and < 56 $L_\odot$, respectively (Chini et al. 1997). MMS 3 has also been detected by previous $H^{13}CO^+$ (1–0) and CS (2–1) observations with the 45 m telescope (Tatematsu et al. 1993, Aso et al. 2000). The mass of this complex is 30.8 $M_\odot$ derived from the $H^{13}CO^+$ (1–0) observations (Aso et al. 2000). There is a X-ray source in this region, which coincides with MMS 3 (X-ray source 10, identified by Tsuboi et al. 2001). MMS 3 and MMS 4 are not associated with VLA -3.6 cm emission and any signature of CO outflow/jet.

There is no obvious 3.3 mm emission toward MMS 3 and MMS 4 as shown in Figure 6*b*. We did not detect the 3.3 mm compact sources in this region. On the other hand, there is a faint 24 μm source at the position of the 1.3 mm and X-ray source (i.e., MMS 3), suggesting the possible presence of a protostar (also reported Tsuboi et al. 2001, Tsujimoto et al. 2002). MMS 3 is peculiar in the sense that there is a 24 μm and 1.3 mm source without high-density material traced by the 3.3 mm emission. Figure 6*a* shows a total intensity map of the $H^{13}CO^+$ emission in the MMS 3/4 region over the velocity range of 10.2 – 12.4 km s^{-1}. In contrast to the 3.3 mm emission, there is significant $H^{13}CO^+$ emission with a size and mass of 13200 × 10600 AU and 4.15 $M_\odot$, respectively. The peak position of the $H^{13}CO^+$ emission is roughly 5″ South-East from the 1.3 mm peak position. Figure 1*d* show the $H^{13}CO^+$ line profile taken with the 45 m telescope. We see a double-peaked line profile at the MMS 3 position (within 18″ radius) with a systemic

[‡]Because of the lack of the spatial resolution, the binary system is not resolved in 24 μm.

velocities of 10.8 and 11.5 km s^{-1}, respectively.

Figure 15 shows a P-V diagram along the major axis of the $H^{13}CO^+$ clump. In the P-V diagram, we found a strong component with a systemic velocity of 11.5 km s^{-1}, which is also seen in the 45-m line profile. This component is associated with the 1.3 mm (and 24 μm, X-ray) source. There are two other velocity components in the P-V diagram, Core (1) and Core (3).

4.4.5. MMS 5

MMS 5 is the third strongest 1.3 mm continuum source in the OMC-3 region. Previous near- and mid-infrared observations at a wavelength of 2 – 17.8 μm did not detect any heating source in the central region (Nielbock et al. 2003). MMS 5 has a 0.1 pc scale CO bipolar outflow along the east-west direction, and chain of knots along the the outflow (See Chapter 2 in this thesis, Yu et al. 1997, Aso et al. 2000, Williams et al. 2003, Stanke et al. 2002).

Figure 7*b* shows a distribution of the 3.3 mm continuum emission. The peak position of the 3.3 mm continuum emission is located at 2″ east of the 1.3 mm peak position. Further we found a 24 μm mid-infrared source from the Spitzer deep observations for the first time. The peak position of the 24 μm source coincides with the 3.3 mm continuum peak position, suggesting the presence of the protostar of MMS 5. Figure 7*a* shows a total-integrated intensity map of the $H^{13}CO^+$ emission in MMS 5 over the velocity range of 10.4 – 12.0 km s^{-1}, overlaid by the CO(3–2) high-velocity image taken with ASTE (i.e., CO bipolar outflow). The $H^{13}CO^+$ envelope has an elongated structure with a position angle of 0°, which is perpendicular to the large-scale outflow and chain of knots with a position angle of 90°. The mass and size of this envelope are 1.50 $M_\odot$ and 10600 × 5300 AU with a position angle of 0°, respectively.

Figure 16*a* shows a P-V diagram of MMS 5 along the major axis. There is a velocity gradient along the disk-like envelope (denoted by the blue-doted line), suggesting the rigid rotation. Figure 16*b* shows a P-V diagram along the minor axis. There appears two kinds of $H^{13}CO^+$ component; one is the central $H^{13}CO^+$ envelope associated with the 3.3 mm emission around the systemic velocity of 11.3 km s^{-1}, and the other in the velocity around 10.5 and 11.8 km s^{-1}, respectively (denoted by two dashed circles in Figure 16*b*). These components exhibit a velocity gradient along the minor axis. This velocity gradient same sense to that of the CO outflow, which suggests the expanding gas motion along the outflow axis. We also detected a velocity gradient along the minor axis in the disk-like envelope (denoted by blue dashed line), which has a same velocity gradient of the CO outflow. This velocity gradient can interprete that the expanding gas motion along the outflow axis or infalling motion along the disk-like envelope.

4.4.6. MMS 6

MMS 6 is the strongest 1.3 mm continuum source in the OMC-2/3 region. The mass and bolometric luminosity of MMS 6 are 36 $M_\odot$ and < 60 $L_\odot$, respectively, and the submillimeter to bolometoric luminosity ratio is $L_{\rm bol}/L_{\rm smm} < 61$, suggesting Class-0 type SED (Chini et al. 1997). We did not detect any clear CO(3–2) outflow, as reported by previous CO(1–0) observations (Williams et al. 2003, Matthews et al. 2005).

Figure 8*b* shows a 3.3 mm dust continuum image, which is slightly elongated along the

NW-SE direction. The peak position of the 3.3 mm emission coincides with the 1.3 mm peak position with a size of 1200 × 1000 AU. Figure 8*a* shows the $H^{13}CO^+$ total-integrated intensity map with a velocity range of 10.9 - 12.1 km s^{-1}. The peak position of the $H^{13}CO^+$ emission shifts approximately 3″ South-West from the millimeter continuum peak.

We have also performed 2 mm dust-continuum observations with the NMA extended configuration (see Figure 8*c*). The higher-resolution continuum image has revealed that MMS 6 contains multiple continuum peaks, that is, the brightest source, MMS 6-main, and at least 7 faint dust condensations (a-g in Fig 8*c*). The typical separation of these dust condensations is $\sim$ 1000 AU, which is one order of magnitude smaller than that in previously defined "proto-clusters" (e.g. NGC2068 in Motte et al. 2001). MMS 6 main dominates the most of the continuum flux with a flux ratio of $(F_{\rm main}/F_{\rm core\ a-g})$, > 5. On the other hand, we detected three 8 μm MIR sources taken with SPITZER/IRAC in MMS 6 (MIR-N, M, S; open green circles in Figure 8*c*). [§] . There is no sign of molecular outflows associated with any of the dust condensations from our CO observations with the NMA and ASTE, although radio jets (VLA- 3.6 cm) and faint optical jet feature (JHK_s image) are detected toward MIR-N (see Chapter III).

MMS 6-main (most intense) and MIR-N (i.e., norther part of 8μm source) are particularly interesting starless and protostellar sources, respectively. The size, mass, and the average density of MMS 6-main are estimated to be 900 AU, 1.26 - 3.42 $M_\odot$, and (2.30 - 6.25) × 10^7 cm^{-3}, respectively assuming β=0.4 –1, T_d=20 K. Although the gas mass in MMS 6-main is one order of magnitude higher than that in low-mass proto-cluster (e.g. ρ-Oph E; Belloche et al. 2001) and the density is 2-3 orders of magnitude higher than that of typical low-mass dense cores, No 24 μm source taken with the SPITZER, which should trace an inner hot dust ($T_{\rm dust} \sim$ 50 K), is detected toward MMS 6-main. On the other hand, our NMA observations have detected the $C^{34}S$ (3–2) emission only at the position of MIR-N (see color image in Figure 8*d*), whereas there is no detectable $C^{34}S$ counterpart toward MMS 6-main. There is also a 3.6 cm free-free jet associated with MIR-N (open square in Figure 8*d*; Reipurth et al. 1999). These results may suggest that MMS6-main is a cold and massive starless core while MIR-N is a forming stellar member with warm molecular gas. In other words, these NMA results imply that MMS 6 is a mixture of starless cores and protostars at different evolutionary stages in the on-going cluster-forming region, that is, a "proto-cluster".

4.4.7. MMS 8 and MMS 9

The millimeter sources MMS 8 and MMS 9 are located at the most southern part of the OMC-3 region. MMS 8 and MMS 9 are also identified as 350 μm sources of CSO 13 and CSO 14 (Lis et al. 1998). The masses and bolometric luminosities of MMS 8 and MMS 9 are 9 $M_\odot$ and 10 $M_\odot$, and $<$ 178 $L_\odot$ and $<$ 145 $L_\odot$, respectively (Chini et al. 1997). Extended $H^{13}CO^+$ emission is detected toward MMS 8 and MMS 9 with a mass of 21 $M_\odot$ in the previous 45 m observations (from Aso et al. 2000). There is no infrared source nor outflow/jet toward MMS 8. On the other hand, a 1 pc-scale giant CO outflow is detected toward MMS 9 from our CO(3–2) and previous CO(1–0) observations (Aso et al. 2000, Williams et al. 2003; see Chapter 3). VLA-3.6 cm continuum emission (i.e., radio jet) is also detected at MMS 9.

[§]Because of the lack of the spatial resolution, there appears only two 24 μm counterparts. In the higher-resolution 8μm image, three 8 μm sources (two bright and one faint source) have been revealed.

Figure 9*b* shows the 3.3 mm continuum emission taken with the NMA in the MMS8/9 region. The 3.3 mm continuum emission above 3 σ level did not detect toward MMS 8. We detected 3.3 mm continuum emission at MMS 9 which is elongated along the NW-SE direction, and the peak position roughly coincides with the 1.3 mm peak position. Figure 9*a* shows a total-integrated intensity map of the $H^{13}CO^+$ emission in the MMS8/9 region over the velocity range of 10.9 – 12.0 km s^{-1}. Significant $H^{13}CO^+$ emission is located between the MMS 8 and MMS 9 position. MMS 9 is not associated with the significant $H^{13}CO^+$ emission at the position of the dust peak. The dense-gas envelope around MMS 9 is likely to be already disrupted by the associated molecular outflow.

4.4.8. MMS 10

The millimeter source MMS 10 is out of the main OMC filament and locates ~2′ east of MMS 9. This source is also detected in the millimeter CS and $H^{13}CO^+$ lines by previous 45 m observations (Tatematsu et al. 1993, Aso et al. 2000). There is no infrared nor VLA-centimeter source at the position of MMS 10. Our CO(3–2) observations did not find any sign of the associated molecular outflow either.

Extended weak 3.3 mm emission with a mass of $< 0.21 - 0.59\ M_\odot$ is detected at the position of the 1.3 mm peak of MMS 10 as shown in Figure 9*b*. (We did not detected 3 .3 mm dust continuum emission above 3 σ level.) The $H^{13}CO^+$ line profile shows a single Gaussian at MMS 10 (See Figure 1*k*) with a systemic velocity of 12.1 km s^{-1}. Figure 10*a* shows a total-integrated intensity map of the $H^{13}CO^+$ emission in MMS 10 over the velocity range of 11.5 – 12.7 km s^{-1}. The $H^{13}CO^+$ emission shows a centrally-condensed structure with a size and mass of 6700 × 3500 AU and 0.55 $M_\odot$, respectively. There is no 3.3 mm compact component associated with the $H^{13}CO^+$ emission, and the 3.3 mm emission is located roughly 8″ North-West of the $H^{13}CO^+$ emission. MMS 10 is likely to be a prestellar core, because there is no signature of heating sources, and outflow/jets.

4.4.9. FIR 2

Millimeter source FIR 2 is located at the northern part of the OMC-2 region (Chini et al. 1997). This source is also identified by the 350 μm observations as CSO 20 (Lis et al. 1998). The mass and bolometric luminosity of the dust condensation are 8 $M_\odot$ and $< 157\ L_\odot$, respectively (Chini et al. 1997). A mid-infrared source was detected at FIR 2 (Nielbock et al. 2003). There is no 2MASS source toward this mid-infrared source, suggesting the embedded nature of the source. There is a CO outflow with a size of 0.1 pc in this region along the NE-SW direction (See Chapter III, Aso et al. 2000, Williams et al. 2003), but no 3.6 cm VLA source is detected.

Figure 11*b* shows distribution of the 3.3 mm continuum emission. The peak position of the 3.3 mm continuum emission roughly coincides with the 1.3 mm peak position. This 3.3 mm continuum emission also coincides with the Spitzer 24 μm emission, suggesting the presence of the heating source. Figure 11*a* shows a total-integrated intensity map of the $H^{13}CO^+$ emission in FIR 2 over the velocity range of 10.1 – 12.6 km s^{-1}, overlaid on the CO(3–2) outflow map taken with ASTE. The peak position of the $H^{13}CO^+$ emission roughly coincides with the 3.3 mm continuum position. The mass and size of dense gas in the $H^{13}CO^+$ emission is 1.67 $M_\odot$ and 15000 × 3100

AU, respectively. At the north-eastern part of FIR2, the $H^{13}CO^+$ emission shows a "cone-shaped" structure. This "one-side" cone-shaped structure seems to delineates the rim of the red-shifted outflow.

Figure 17*a* shows a P-V diagram of FIR 2 along the major axis. There is no well-defined velocity gradient in the $H^{13}CO^+$ emission. Figure 17*b* shows a P-V diagram along the minor axis. Two kinds of $H^{13}CO^+$ components are seen. One is the main envelope component associated with the 3.3 mm emission around the systemic velocity of 11.9 km s^{-1}, and the other without the 3.3 mm emission in the velocity range of 12.1 –12.5 km s^{-1} (denoted by a dashed circle in Figure 17*b*). In the former one, we detected a sign of a velocity gradient perpendicular to the associated outflow. This velocity gradient shows an opposite sense to that of the CO outflow, suggesting the expanding-gas motion along the flattened envelope (same as MMS 7 in Chapter 2). The latter component has the same velocity gradient as that of the CO(3–2) outflow (i.e., red-shifted component lying north-east), suggesting the dispersing gas entrained by CO outflow.

5. Discussion

5.1. Distribution of the $H^{13}CO^+$(1–0) and 3.3 mm continuum emission

We use the term "envelope" as a circumstellar gas detected in the $H^{13}CO^+$(1–0) emission with the NMA. In the following discussion, we except MMS 6, because this object is protocluster candidate and have peculiar physical properties.

We detected the $H^{13}CO^+$(1–0) envelope toward all of our targets. 24 μm and 3.3 mm compact sources, implying presence of the heating source (i.e., protostellar candidate), are associated with the 6/12 samples, SIMBA a(1), MMS 2, MMS 5, MMS 7, MMS 9 and FIR 2. The other 4/12 samples, SIMBA a(2), MMS 4, MMS 8, and MMS 10, are neither associated with the 24 μm nor 3.3 mm compact sources, implying the absence of the heating source (i.e., prestellar candidate). We also detected two other types of sources; MMS 1 is associated with the 3.3 mm emission but no 24 μm source, whereas MMS 3 is associated with the 24 μm source [¶] but no 3.3 mm emission. We classified these sources as "transient" objects from pre-stellar to proto stellar phase.

The total mass, average density, and the spatial extent of the detected $H^{13}CO^+$ envelopes are 0.57 – 4.15 $M_\odot$, (7.2–51) $\times$ 10^4 cm^{-3} and several $\times$ 0.01 pc, respectively. We did not detect obvious difference of these parameters between pre- and proto-stellar samples (see vertical axis in Figure 18). On the other hand, we detected the 3.3 mm compact continuum source toward 8/12 samples, which has average densities and spatial extents of (3.14 – 49.3) $\times$ 10^6 cm^{-3} and (1–3) $\times$ 10^3 AU, respectively. The 3.3 mm continuum emission traces innermost region with a 2-3 order of magnitude larger density and one-order of magnitude smaller size scale of the surrounding $H^{13}CO^+$ envelope. These results suggest that the average density of several $\times$ 10^6 cm^{-3} are required to form a seed of intermediate-mass protostars.

[¶]We have detected just longer-wave length than the 24 μm continuum emission

5.2. $H^{13}CO^+$ Depletion ?

Our $H^{13}CO^+$ maps taken with the NMA (Fig. 3 - 11) show that in most sources the peak position of the $H^{13}CO^+$ emission does not coincide with (i.e., shifts a few arcsec from) the peak position of the 3.3 mm emission. One interpretation to explain this offset is depletion of HCO^+ at the center of the dusty condensations. In Figure 18, we compare the mass of the dusty condensations observed in the 3.3 mm emission to the mass of dense gas observed in the $H^{13}CO^+$ emission. Black and red plots indicate protostellar and prestellar samples, that is, with or without the 24 μm and 3.3 mm source, respectively. We classified MMS 1 and MMS 3 as "transient" objects, plotted as blue circles in Figure 18. If the $H^{13}CO^+$ abundance were constant over the entire sample, these plots should show a linear correlation, since both the $H^{13}CO^+$ and the 3.3 mm emission is likely to be optically thin. However, there is a significant scatter in these plots, and the $H^{13}CO^+$ to 3.3 mm mass ratio varies more than one order of magnitude. The $H^{13}CO^+$ intensities do not change much from prestellar to protostellar sources, while only in the protostellar sources the 3.3 mm emission is present. These results suggest that there is a variation of the $H^{13}CO^+$ abundance, and the $H^{13}CO^+$ abundance decreases in the protostellar sources.

The depletion of $H^{13}CO^+$ can proceed in the condition of lower gas temperature than the sublimation temperature of CO (< 20 K), and/or high densities of $n \geq 10^6$ cm^{-3} (e.g., Di Francesco et al. 2007, for a review). In the case of low-mass star-forming regions, observational studies of CO and isotopic lines toward prestellar cores have revealed significant depletions of CO at the innermost region with a factors of 100 – 1000 (Caselli et al. 1999, Ohashi et al. 1999, Bergin et al. 2002). The kinematic temperature of the dusty condensations in our sample is approximately 20 K at a size of roughly 0.2 pc (Cesaroni et al. 1994). This kinematic temperature is similar to the CO sublimation temperature. In addition, the average densities in the 3.3 mm sources are high with (3.13 – 49.3) $\times$ 10^6 cm^{-3}, implying the favorable condition for the depletion of CO. On the other hand, in our protostellar samples there are heating sources as seen in the 24 μm emission, so the evaporation of CO from grain surfaces could proceed in the protostellar samples, which contradicts with our results in Figure 18. Hence, hereafter, we consider the effect of the heating from the central source. The typical bolometric luminosity of 100 $L_\odot$ suggests that the region warmer than 20 K is at most 2500 AU in radius. We, here, assume the temperature distribution of $T(r) \propto r^{-0.5}$, and $T = 35$ K at 800 AU (from two-dimensional axisymmetric calculation in the case of 100 $L_\odot$, T.Nakazato private communication). This size is similar to the typical NMA spatial resolution of 2300 AU (corresponding to 5″), which cannot explain the $H^{13}CO^+$ depletion. We also considered effect of the optical depth. The optically thick dust emission absorb the background $H^{13}CO^+$ emission. However, average density where the optically depth at 3.3 mm becomes $\sim$1, 5.8 $\times 10^9$ cm^{-3} [‖] , is much larger than the observed 3.3 mm dust densities of (3.14 –49.3) $\times 10^6$ cm^{-3}. This result imply that the 3.3 mm dust emission in OMC-2/3 is optically thin and not affect an absorption of the $H^{13}CO^+$ emission. In summary, It is too controversial to fully explain the offset of the peak position of the $H^{13}CO^+$ and 3.3 mm dust emission.

[‖]We, here, assumed that the mass-absorption coefficient of dust grains of 0.0037 cm^2 g^{-1} (λ/ 400 μm)$^{-\beta}$ (from Ohashii et al. 1996), dust opacity $\beta \sim 1$ and size of the dusty envelope of 2000 AU.

5.3. Kinematics in the Dense-Gas Envelopes traced by the $H^{13}CO^+$ Emission

Results of the kinematics in the $H^{13}CO^+$ envelope are summarized in Table 9. Velocity gradients along the major axis, implying rotating motion, are detected toward 5/12 samples. These samples cover the whole evolutionary stage from prestellar to later protostellar evolutionary stage (see in Chapter V). We estimated the average angular momentum at the radius of the $H^{13}CO^+$ envelope as follows,

$$\Omega = R_{\rm FWHM} \times \Delta V_{\rm FWHM} \ \ [\rm pc\ km\ s^{-1}], \tag{IV.4}$$

where $R_{\rm FWHM}$ is the FWHM radius of the $H^{13}CO^+$ envelope and $\Delta V_{\rm FWHM}$ is the velocity width caused by the rotating motion. Figure 19 shows local specific angular momentum plotted as a function of the envelope radius. Our samples are plotted as green circles in Figure 19. The average angular momenta in our OMC -2/3 samples are typically one order of magnitude larger than those of low-mass counterpart. In our sample there is no obvious difference of the angular momentum between the sources with and without the 3.3 mm and 24 μ sources (i.e., presence of heating source). In addition, we also plotted specific angular momenta of Herbig Ae/Be samples (i.e., rotationally supported disks) as orange circles (Mannings et al. 2000, Fuente et al. 2006). Although sample number is limited, estimated specific angular momenta are also one-order of magnitude larger than those of low-mass counterparts. These results imply that intermediate-mass protostars are formed from cores with a larger angular momentum than the low-mass counterparts and produce rotationally supported disk with a large angular momentum, although there are observational biases.

Along the minor axis in the $H^{13}CO^+$ envelopes, we detected the gas dispersing motion toward 4/12 samples. Furthermore, a half of these samples has dispersing gas motion not only along the outflow axis but also along the flattened disk-like envelope. In the OMC-2/3 region, the outflow momentum derived by our CO(3–2) observations is typically one order of magnitude larger than that of low-mass counterparts (See Chapter III), which could explain the ubiquitous dispersing motion in our samples. Our results suggest that the dense gas dissipation is one of the essential phenomena in the evolutionary process of a intermediate-mass protostar.

On the other hand, there is no clear evidence of dynamical mass accretion found toward the central protostar in the $H^{13}CO^+$ emission. There are three possible interpretations to explain the absence of the dynamical accretion; (i) no accreting motion in dense gas, (ii) because of the $H^{13}CO^+$ emission do not trace the kinematics inner envelope ($\leq$ a few $\times$ 10^3 AU), and (iii) because the NMA spatial resolution is not enough to resolve the infalling envelopes (i.e., insufficient spatial resolution). It is difficult to consider the possibility of (i), because the presence of the molecular outflow and the MIR sources (i.e., presence of the heating source) implies the existence of the mass accretion. We consider that the combination of (ii) and (iii) is plausible. Most of the $H^{13}CO^+$ peaks do not coincide with the 3.3 mm emission peaks as mentioned above. This result implies that the $H^{13}CO^+$ emission cannot trace the kinematics at the innermost region associated with the protostars. On the assumption that the speed of the expansion of the mass infalling radius is an effective sound speed C_s, the expected infalling radius is $C_s \times \tau_{dyn}$. We, here, assume that the time scale of dynamical accretion is roughly consistent with the outflow dynamical time-scale. The estimated mass infall radii are listed in Table 9. The estimated mass infall radius is comparable to (or smaller than) the NMA beam size of $\sim$ 2300 AU (corresponding to 5″), suggesting that the absence of the infallling motion is likely to be due to the observational artifact. In summary, the

$H^{13}CO^+$ emission is one of appropriate tracers of the outer cold dense-gas envelope, and we mainly succeeded to detect the rotating and dispersing motion with a size scale of 1000 - 10000 AU.

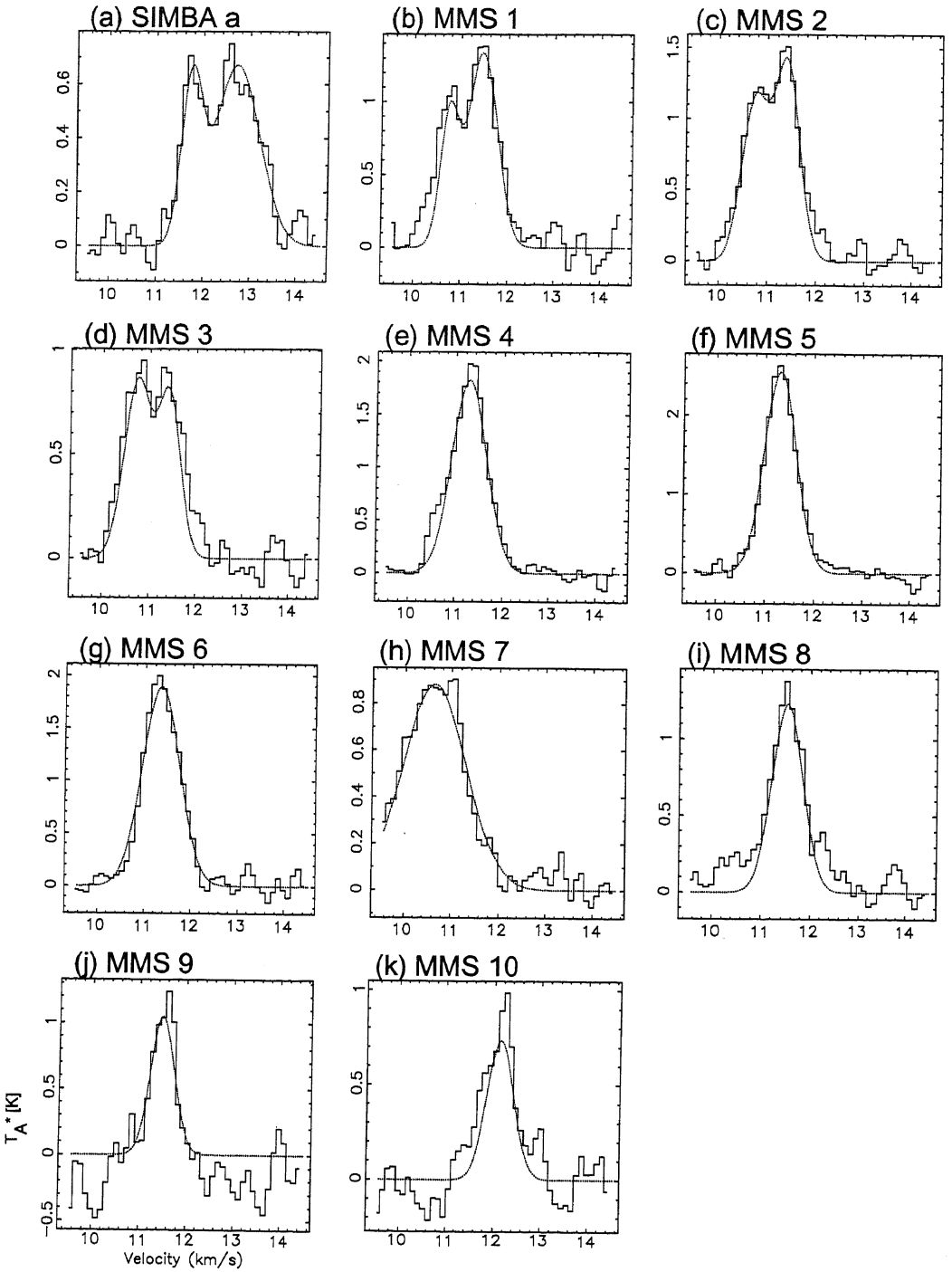

Fig. 1.— $H^{13}CO^+$ (1–0) spectra toward 11 dust condensations (i.e., the peak position of 3.3 mm dust emission taken by the NMA) with the 45 m telescope with 18.5 ″ beam in FWHM. Gaussian fittings shown in the doted lines.

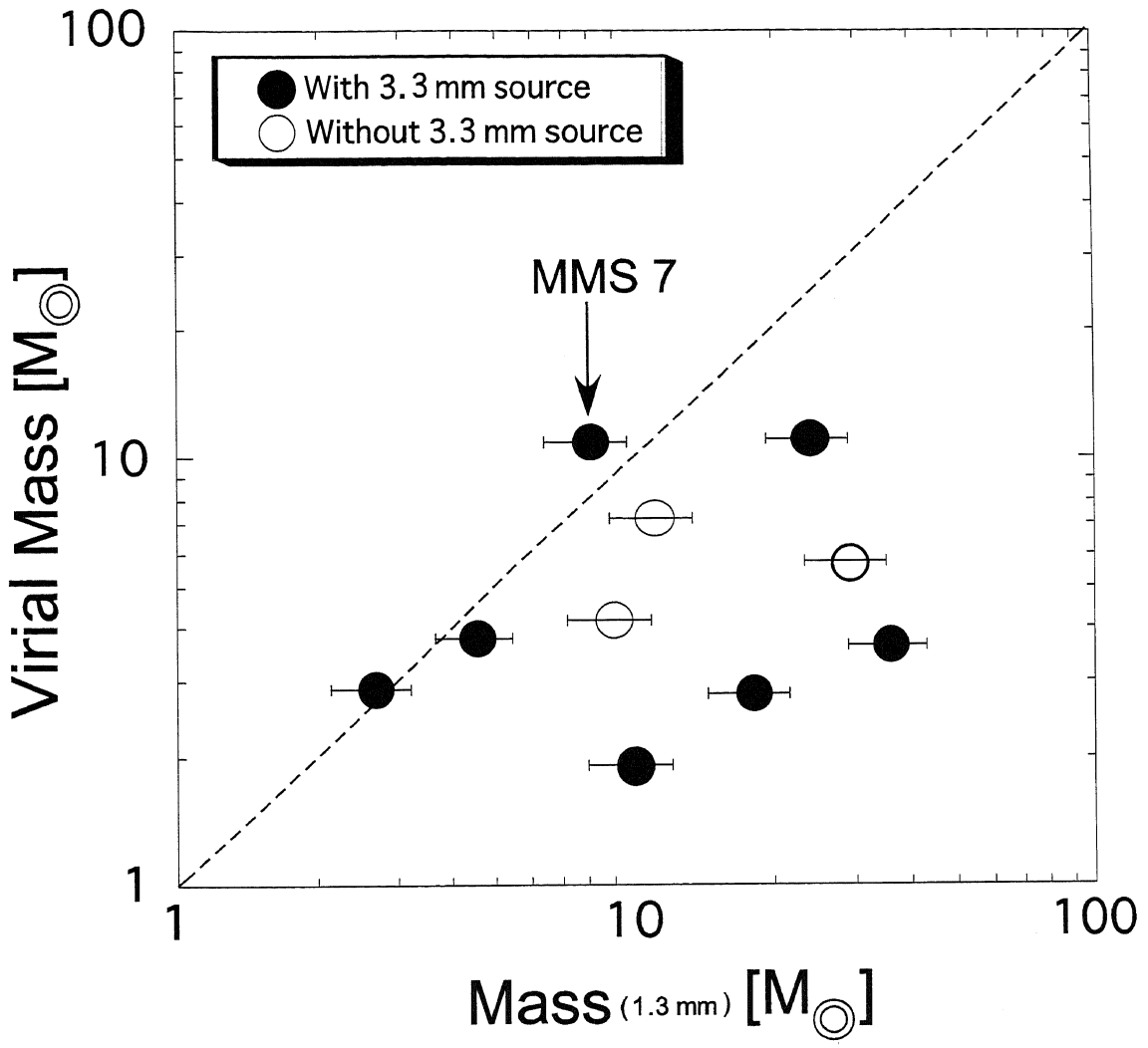

Fig. 2.— Virial masses shown in Table 5 plotted as a function of the dust masses derived by the 1.3 mm emission (Chini et al. 1997). Filled and open circles show the associated and not associated 3.3 mm compact continuum source taken with the NMA, respectively. Dust masses of MMS 1, MMS 4, MMS 6, MMS 7, MMS 8, and MMS 9 are referred from the derived mass by Table 3 of Chini et al. (1997). Dust masses of MMS 2, MMS 5 and MMS 10 are derived assuming that the peak flux density and the deconvolution size of Table 1 of Chini et al. (1997). We also assumed the mass opacities and dust temperature of the value in Table 6. Error bars of the dust mass are caused by the flux absolute error of ~20 %. We consider that the error of virial masses can neglect in this plot, although it is difficult to estimate the error bars of virial masses. There is no plot of MM 3 in this figure, because MMS 3 has no Gaussian shaped structure and we could not obtain correct value.

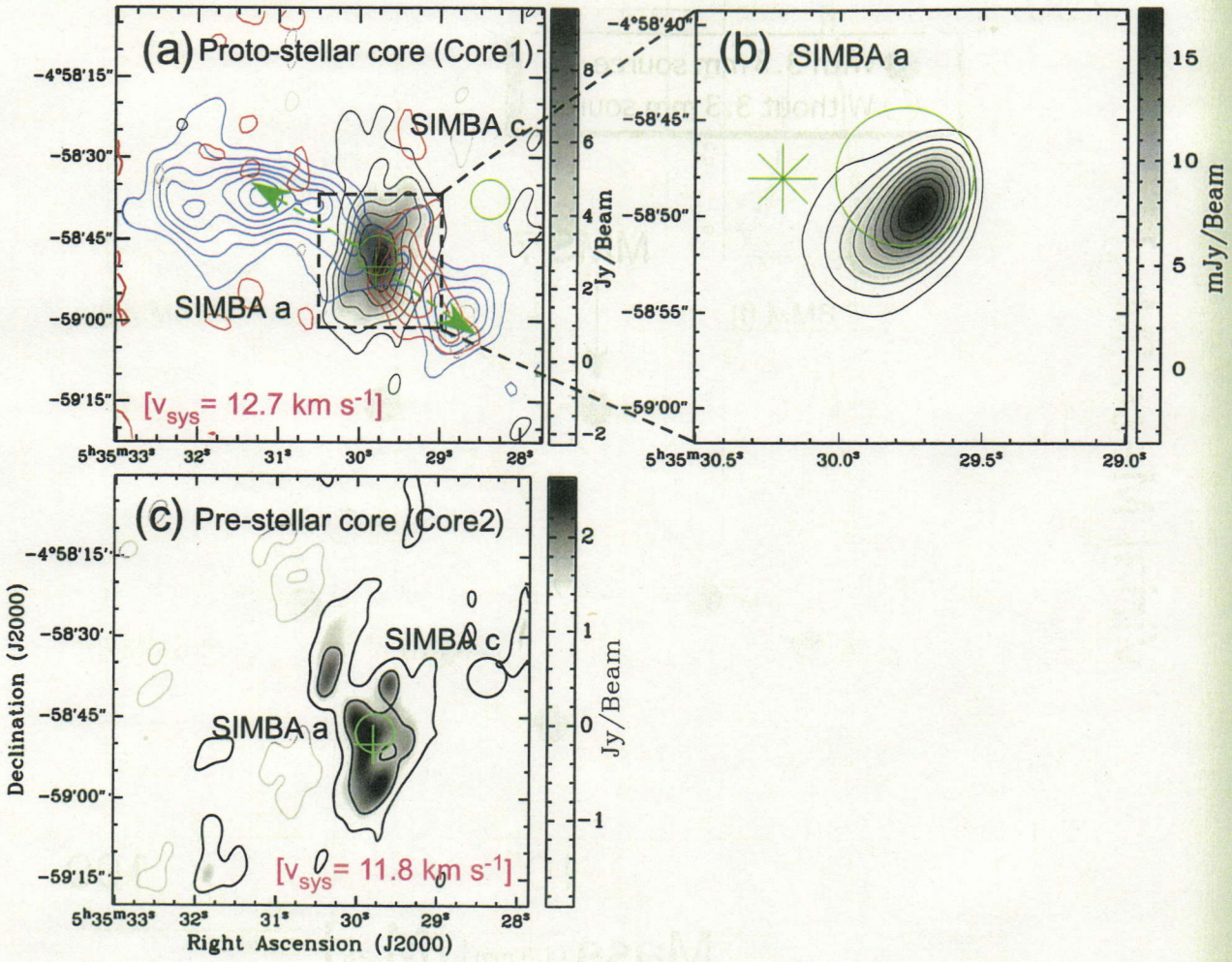

Fig. 3.— (a) NMA total intensity map of the $H^{13}CO^+$ emission toward SIMBA a in integrated from 12.2 – 13.8 km s^{-1}. The contour lines start at ±1.45 km s^{-1} with intervals of 1.45 Jy km s^{-1}. Blue and red contours show the CO(1–0) outflows with the NMA, integrated from 9.8 – 11.4 km s^{-1} and 13.8 – 15.2 km s^{-1}, respectively. The contour lines start at ±3σ levels with intervals of 3σ (1σ level of blue and red contours are 0.644 and 0.345 Jy $beam^{-1}$, respectively). Green arrow show the axis of the CO(1–0) outflow. (b) NMA 3.3 mm dust continuum emission The contour lines start at ± 0.003 Jy $beam^{-1}$ with intervals of 0.0015 Jy $beam^{-1}$. (c) NMA total intensity map of the $H^{13}CO^+$ emission in integrated from 11.4 – 12.1 km s^{-1}. The contour lines start at ± 0.88 Jy km s^{-1} levels with intervals of 0.88 Jy km s^{-1}. Crosses, asterisk and circles show the position of 3.3 mm with the NMA, 1.3mm with the SEST and MIR sources, respectively (Nielboke et al. 2003).

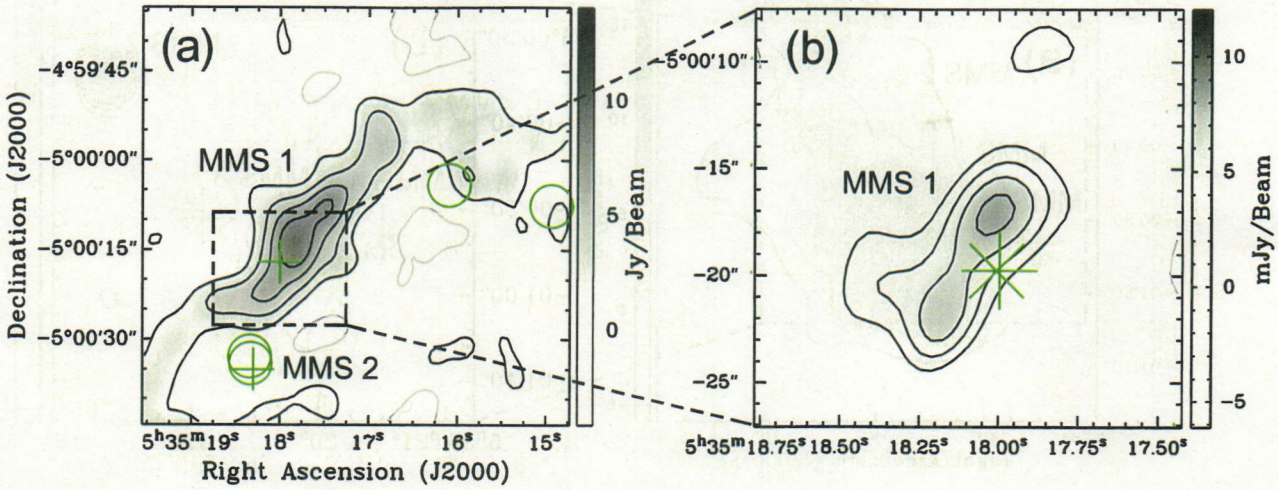

Fig. 4.— (a) NMA total intensity map of the $H^{13}CO^+$ emission toward MMS 1 in integrated from 11.1 – 12.2 km s^{-1}. The contour lines start at ±1.87 Jy km s^{-1} with intervals of 1.87 Jy km s^{-1}. (b) NMA 3.3 mm dust continuum emission The contour lines start at ± 0.003 Jy $beam^{-1}$ with intervals of 0.0045 Jy $beam^{-1}$. Crosses, asterisk and circles show the position of 3.3 mm with the NMA, 1.3mm with the IRAM 30 m and MIR sources, respectively (Chini et al. 1997).

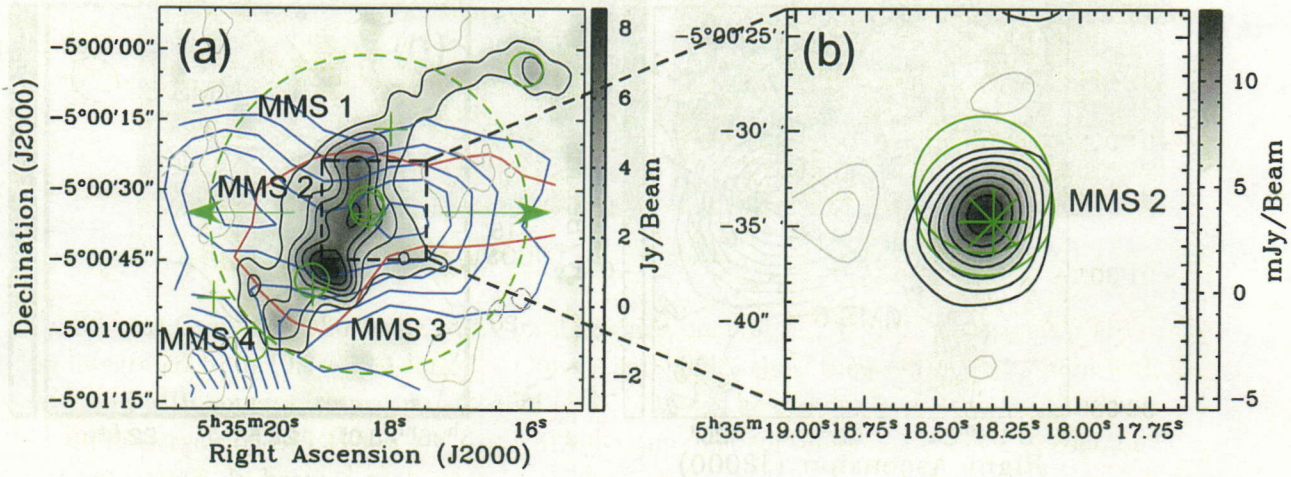

Fig. 5.— (a) Gray scale shows the NMA total intensity map of the $H^{13}CO^+$ emission toward MMS 2 in integrated from 10.5 – 11.1 km s^{-1}. The contour lines start at ± 1.33 Jy km s^{-1} with intervals of 0.99 Jy km s^{-1}. Blue and red contours show the CO(3–2) outflows with ASTE, integrated from 6.7 – 7.8 km s^{-1} and 14.3 – 16.5 km s^{-1}, respectively. Green circle and arrows show the NMA FOV and outflow axis, respectively. (b) NMA 3.3 mm dust continuum emission The contour lines start at ± 0.003 Jy $beam^{-1}$ with intervals of 0.0015 Jy $beam^{-1}$. Crosses, asterisk and circles show the position of 3.3 mm with the NMA, 1.3mm with the IRAM 30 m and MIR sources, respectively (Chini et al. 1997).

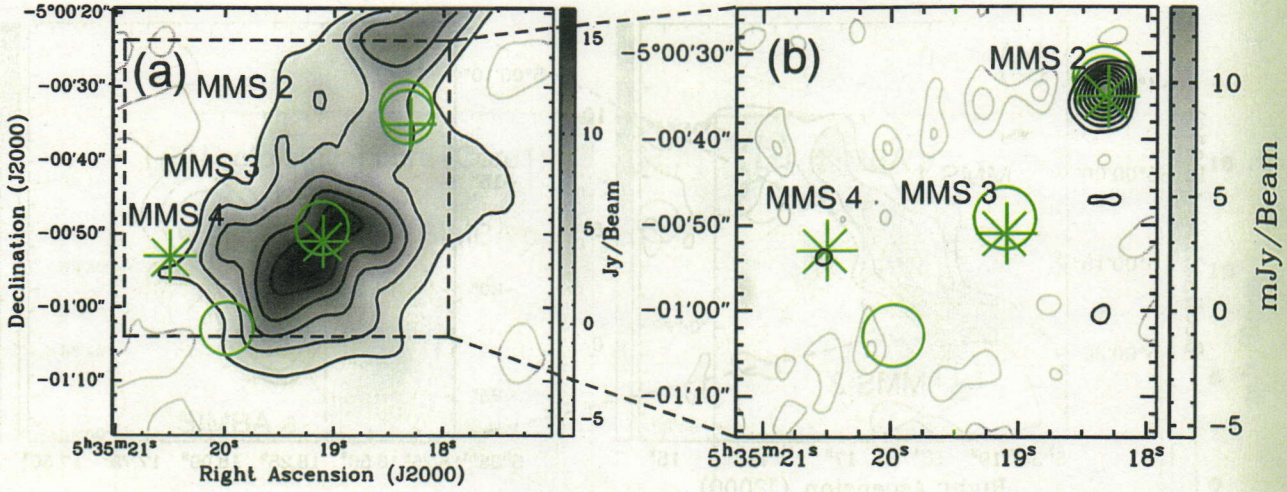

Fig. 6.— (a) NMA total intensity map of the $H^{13}CO^+$ emission toward MMS 3and MMS 4 in integrated from 10.2 – 12.4 km s^{-1}. The contour lines start at ± 2.70 Jy km s^{-1} with intervals of 2.70 Jy km s^{-1}. (b) NMA 3.3 mm dust continuum emission The contour lines start at ± 0.003 Jy $beam^{-1}$ with intervals of 0.0015 Jy $beam^{-1}$. Crosses, asterisk and circles show the position of 3.3 mm with the NMA, 1.3mm with the IRAM 30 m (from Chini et al. 1997) and MIR sources (position of the 10μ source referred from Nielbock et al. 2003), respectively.

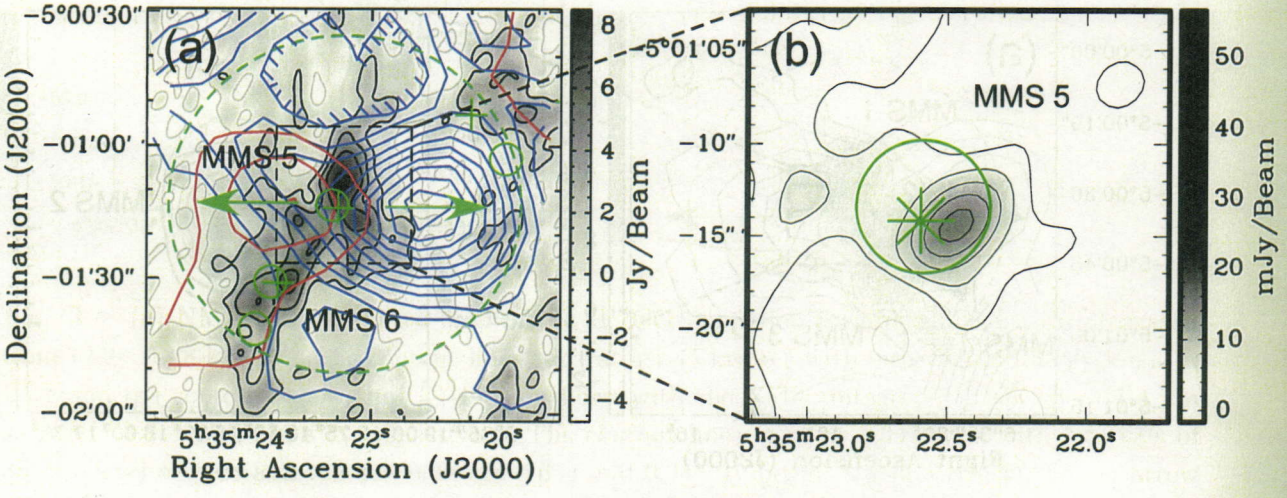

Fig. 7.— (a) Gray scale shows the NMA total intensity map of the $H^{13}CO^+$ emission toward MMS 5 in integrated from 10.4 – 12.0 km s^{-1}. The contour lines start at ± 2.38 Jy km s^{-1} with intervals of 2.38 Jy km s^{-1}. Blue and red contours show the CO(3–2) outflows with ASTE, integrated from 6.7 – 7.8 km s^{-1} and 14.3 – 16.5 km s^{-1}, respectively. Green circle and arrows show the NMA FOV and outflow axis, respectively. (b) NMA 3.3 mm dust continuum emission The contour lines start at ± 0.003 Jy $beam^{-1}$ with intervals of 0.003 Jy $beam^{-1}$. Crosses, asterisk and circles show the position of 3.3 mm source with the NMA, 1.3 mm with the IRAM 30 m and MIR sources, respectively (Chini et al. 1997).

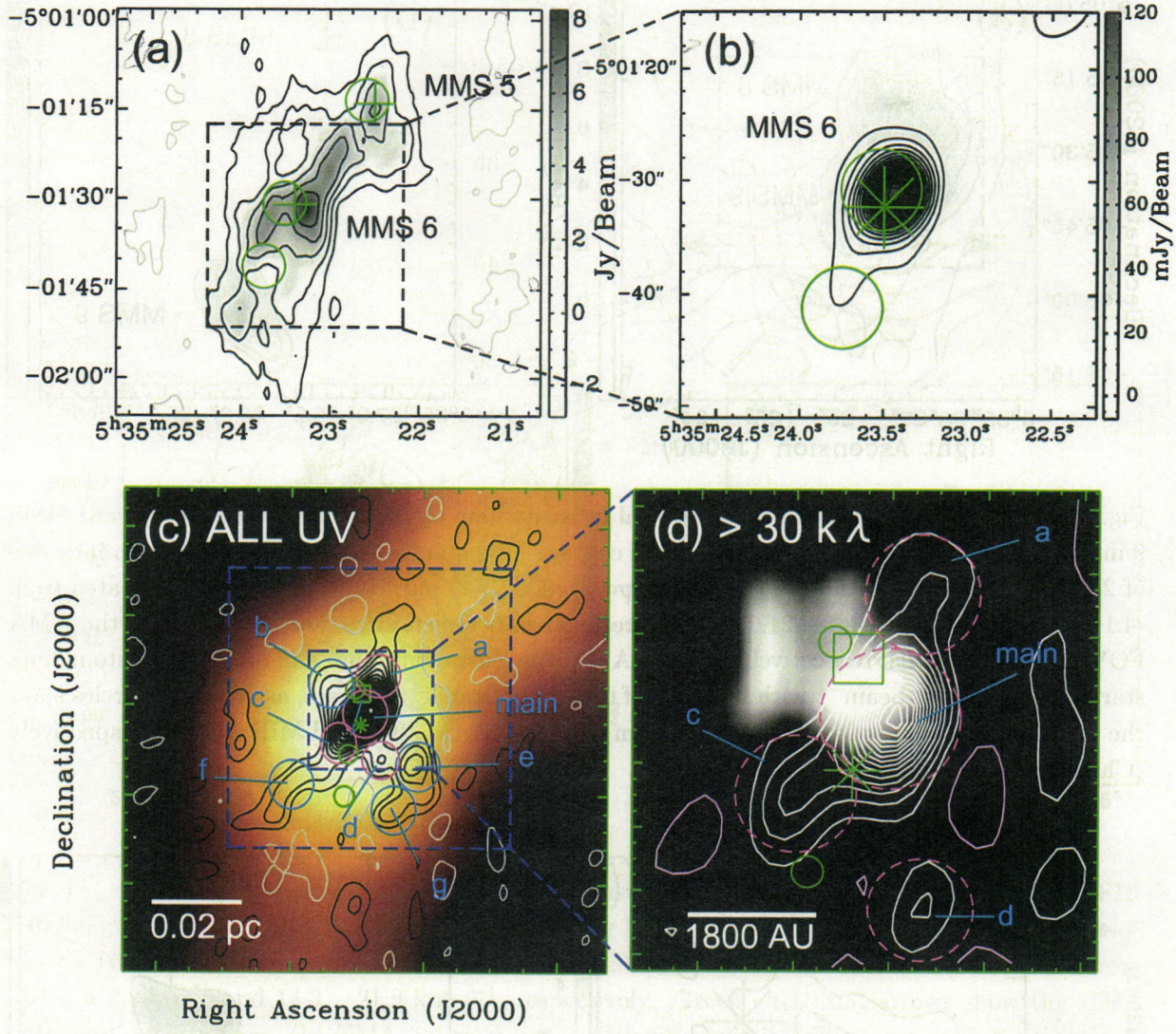

Fig. 8.— (a) Gray scale shows the NMA total intensity map of the $H^{13}CO^+$ emission toward MMS 6 in integrated from 10.9 – 12.1 km s^{-1}. Crosses and circles show the position of 3.3 mm with the NMA and MIR sources, respectively (Chini et al. 1997). The contour lines start at ± 1.36 Jy km s^{-1} with intervals of 1.36 Jy km s^{-1}. (b) NMA 3.3 mm dust continuum emission The contour lines start at ± 0.006 Jy $beam^{-1}$ with intervals of 0.006 Jy $beam^{-1}$. The Asterisk shows the position of 1.3 mm source taken with IRAM 30 m. (c) 2 mm dust continuum emission with th NMA in contour superposed on the 850 *mu*m image in color scale (Johnstone et al. 2003). Dashed large square shows the magnified region in Figure 8*b*. Open green square indicate the position of 3.6 cm (free-free jet). (d) 2 mm dust continuum map made only from the visibility data with the projected *uv* distance larger than 30 kλ in contour superposed on the $C^{34}S$ (3–2) emission in grey scale. Open circles in Figure *c* and *d* show the position of 8 *mu*m position. The north and south sources corresponding to the 24 *mu*m bright source, and middle one is the newly detected faint MIR source in 8*mu*m taken by Spitzer/IRAC.

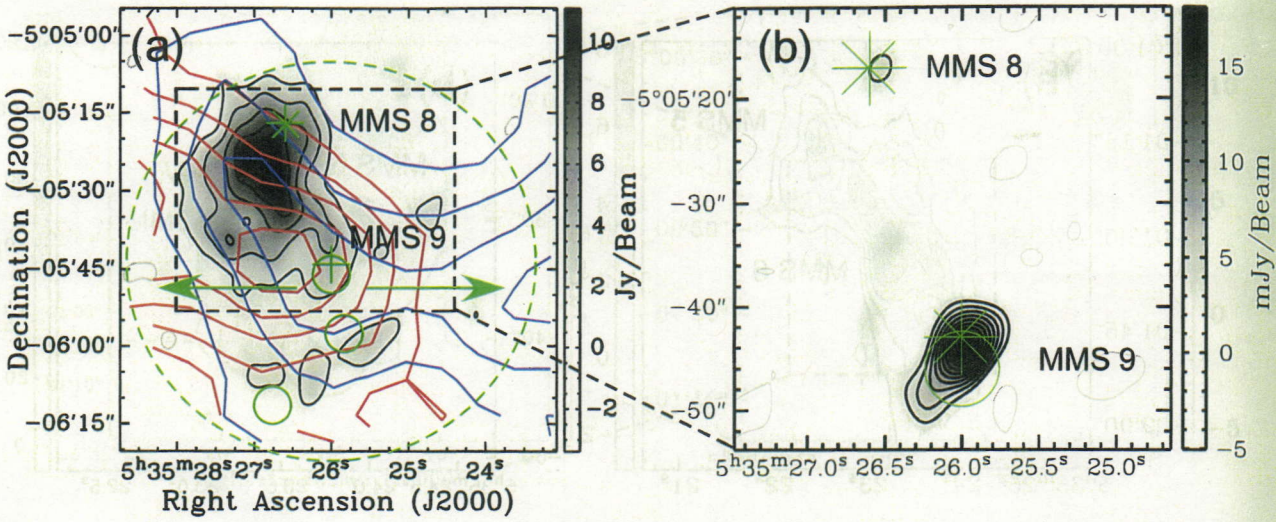

Fig. 9.— (a) Gray scale shows the NMA total intensity map of the $H^{13}CO^+$ emission toward MMS 9 in integrated from 10.9 – 12.0 km s^{-1}. The contour lines start at ± 2.24 Jy km s^{-1} with intervals of 2.24 Jy km s^{-1}. Blue and red contours show the CO(3–2) outflows with ASTE, integrated from -4.1 – 6.7 km s^{-1} and 14.3 – 21.9 km s^{-1}, respectively. Green circle and arrows show the NMA FOV and outflow axis, respectively. (b) NMA 3.3 mm dust continuum emission The contour lines start at ± 0.0045 Jy $beam^{-1}$ with intervals of 0.0045 Jy $beam^{-1}$. Crosses, asterisk and circles show the position of 3.3 mm with the NMA, 1.3mm with the IRAM 30 m and MIR sources, respectively (Chini et al. 1997).

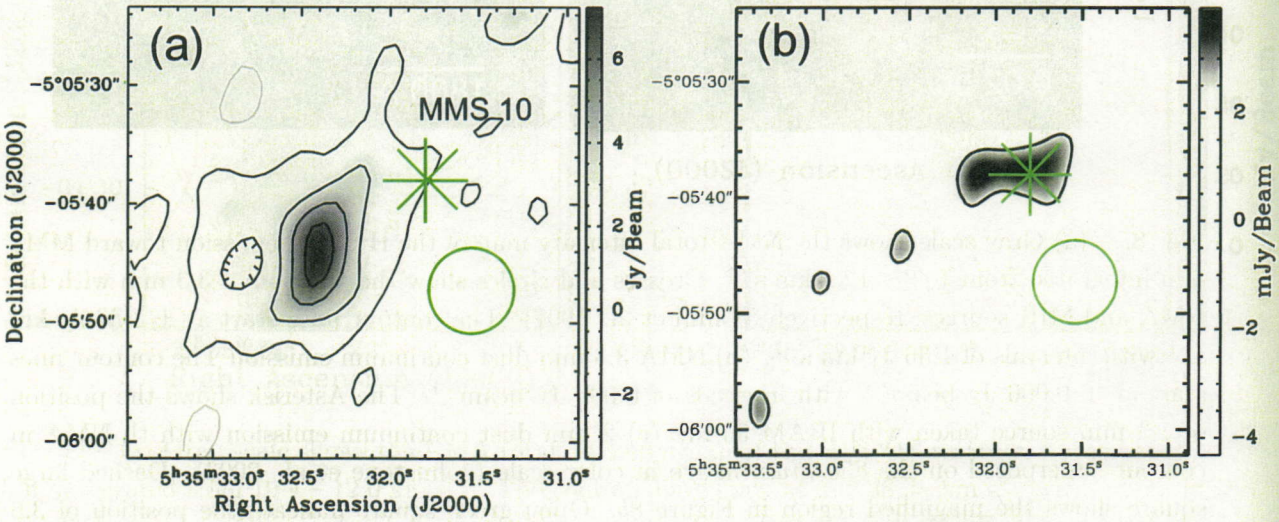

Fig. 10.— (a) NMA total intensity map of the $H^{13}CO^+$ emission toward MMS 10 in integrated from 11.5 – 12.7 km s^{-1}. The contour lines start at ± 1.61 Jy km s^{-1} with intervals of 1.61 Jy km s^{-1}. (b) NMA 3.3 mm dust continuum emission The contour lines start at ± 0.0045 Jy $beam^{-1}$ levels with intervals of 0.0045 Jy $beam^{-1}$. Crosses, asterisk and circles show the position of 3.3 mm with the NMA, 1.3mm with the IRAM 30 m and MIR sources, respectively (Chini et al. 1997).

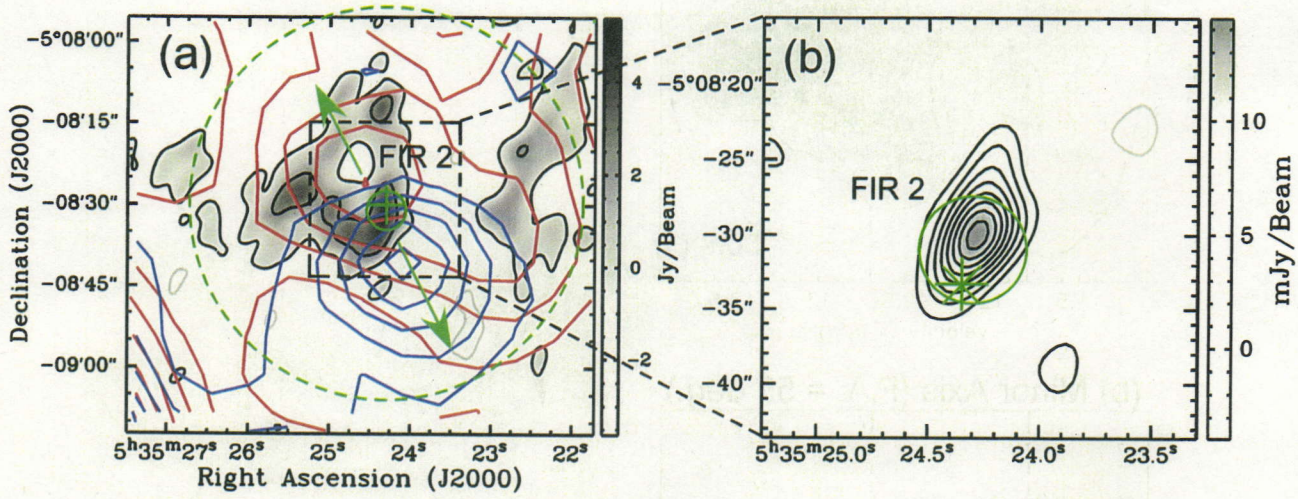

Fig. 11.— (a) Gray scale shows the NMA total intensity map of the $H^{13}CO^+$ emission toward FIR 2 in integrated from 10.1 – 12.6 km s^{-1}. The contour lines start at ± 1.85 Jy km s^{-1} with intervals of 1.85 Jy km s^{-1}. Blue and red contours show the CO(3–2) outflows with ASTE, integrated from -4.1 – 6.7 km s^{-1} and 14.3 – 21.9 km s^{-1}, respectively. Green circle and arrows show the NMA FOV and outflow axis. (b) NMA 3.3 mm dust continuum emission The contour lines start at ± 0.003 Jy $beam^{-1}$ levels with intervals of 0.0015 Jy $beam^{-1}$. Crosses, asterisk and circles show the position of 3.3 mm with the NMA, 1.3mm with the IRAM 30 m and MIR sources, respectively (Chini et al. 1997).

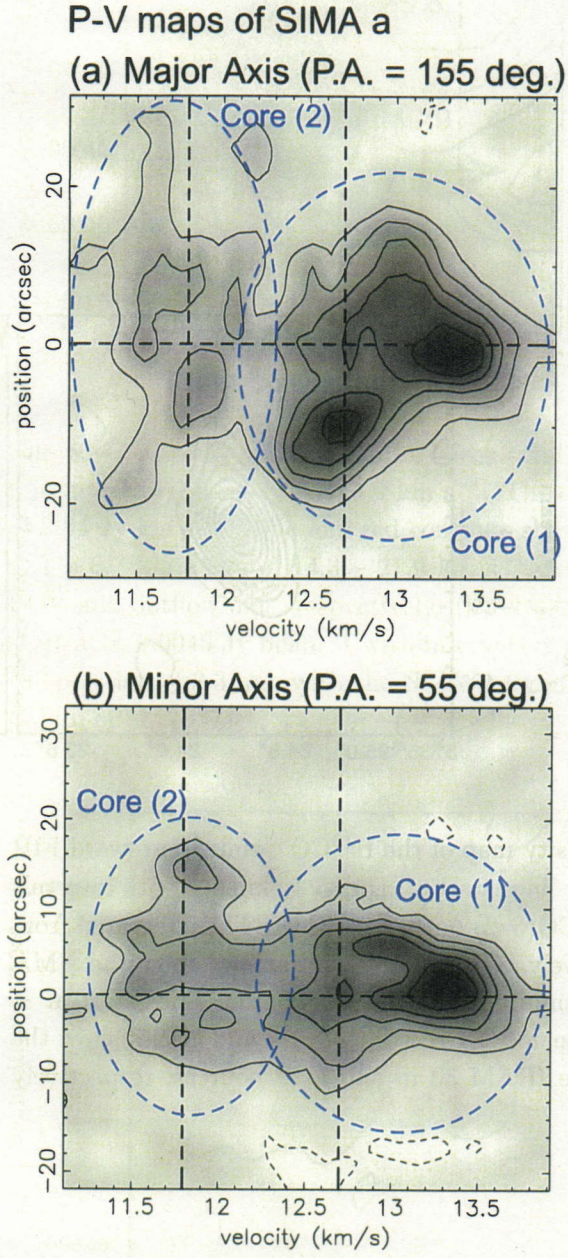

Fig. 12.— $H^{13}CO^+$(1–0) position-velocity maps of SIMA a cut along the major (a) and major axis(b), respectively. Dashed line of vertical and horizontal axis show a systemic velocities of $H^{13}CO^+$ envelopes and position of the 3.3 mm emission peak, respectively. The contour lines start at $\pm 3\sigma$ levels with intervals of 3σ.

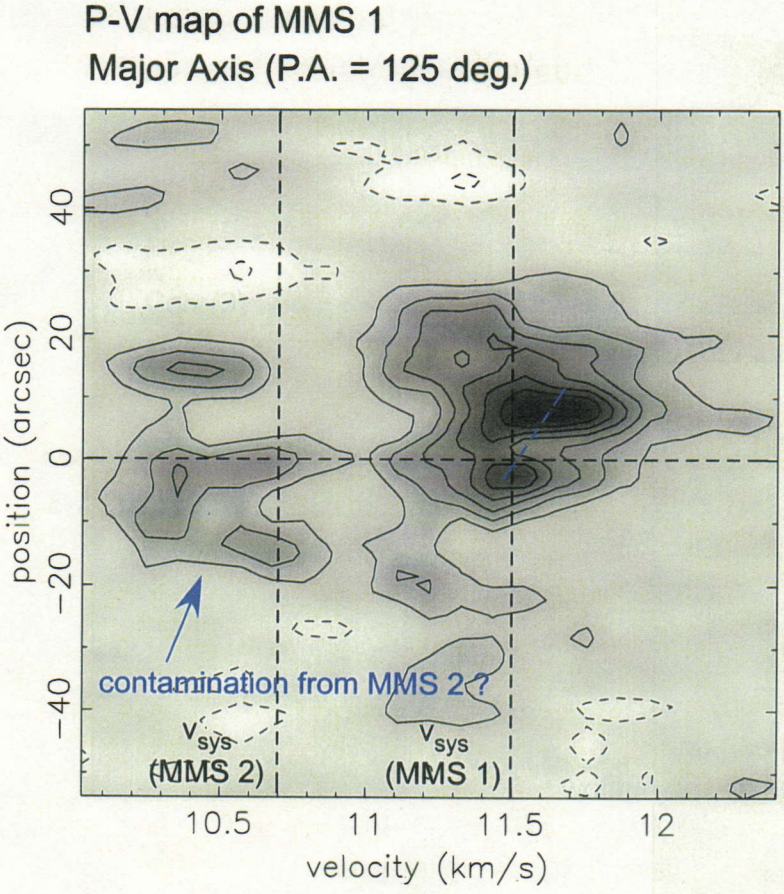

Fig. 13.— $H^{13}CO^+$(1–0) position-velocity map of MMS 1 cut along the major axis. Dashed line of vertical and horizontal axis show a systemic velocity of $H^{13}CO^+$ envelope and position of the 1.3 mm emission peak, respectively. The contour lines start at $\pm 3\sigma$ levels with intervals of 3σ.

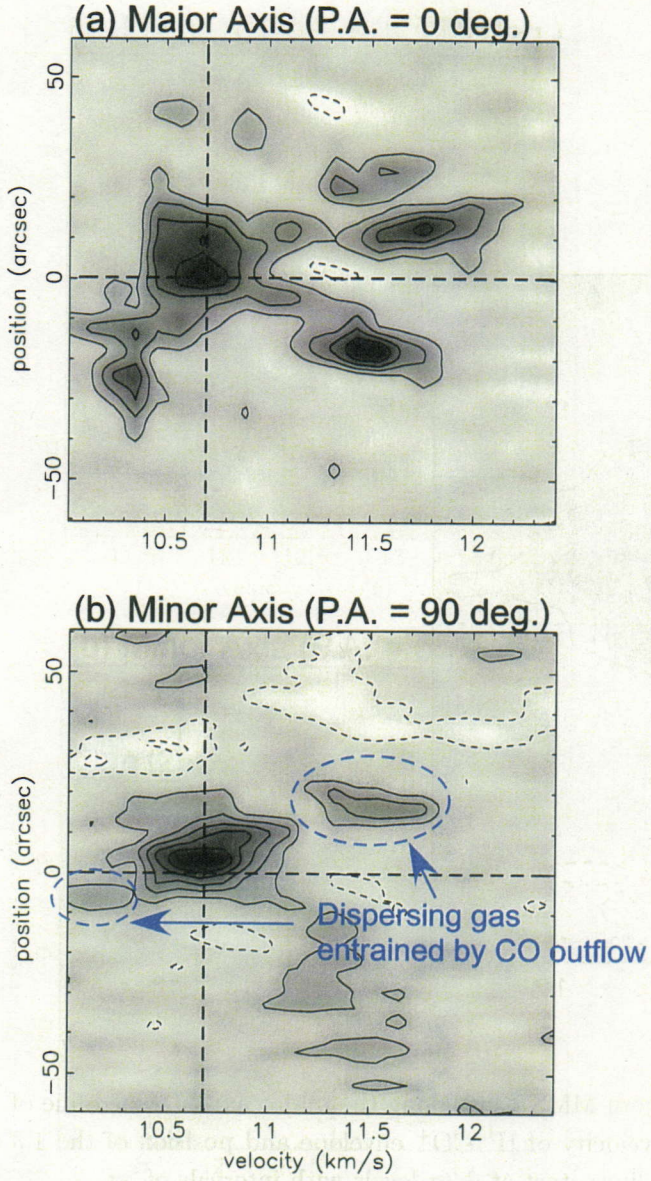

Fig. 14.— $H^{13}CO^+(1–0)$ position-velocity maps of MMS 2 cut along the major (a) and major axis(b), respectively. Dashed line of vertical and horizontal axis show a systemic velocity of $H^{13}CO^+$ envelope and position of the 3.3 mm emission peak, respectively. The contour lines start at $\pm 3\sigma$ levels with intervals of 3σ.

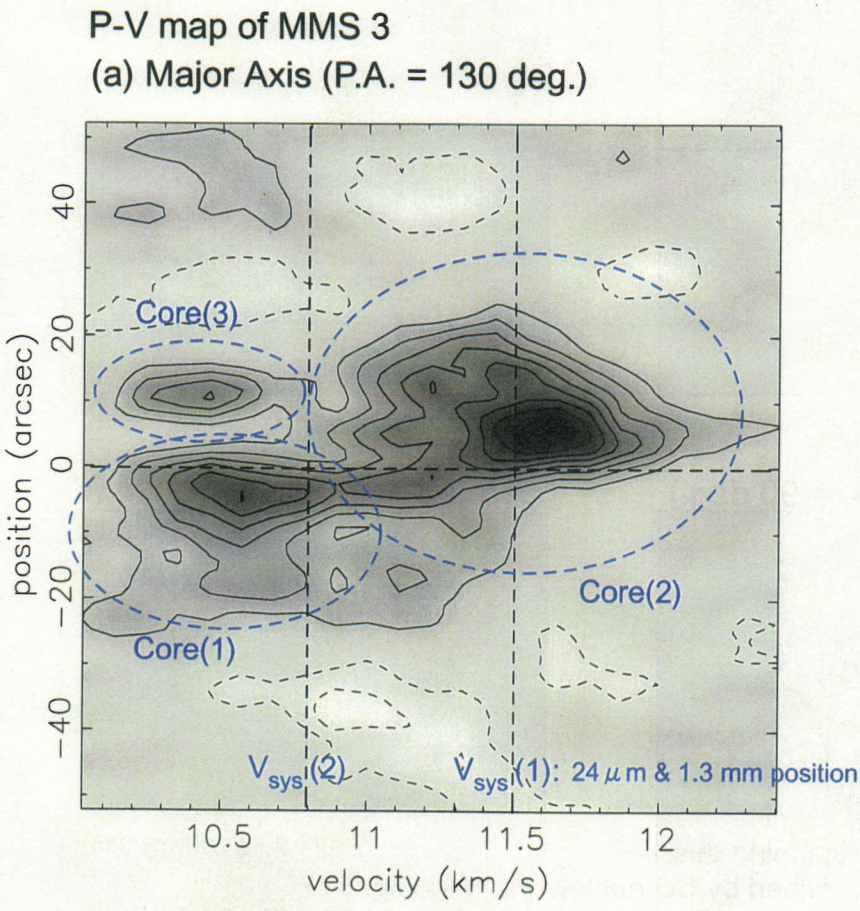

Fig. 15.— $H^{13}CO^+$(1–0) position-velocity map of MMS 3 cut along the major axis. Dashed line of vertical and horizontal axis show a systemic velocities of $H^{13}CO^+$ envelopes and position of the 1.3 mm emission peak, respectively. The contour lines start at $\pm 3\sigma$ levels with intervals of 3σ.

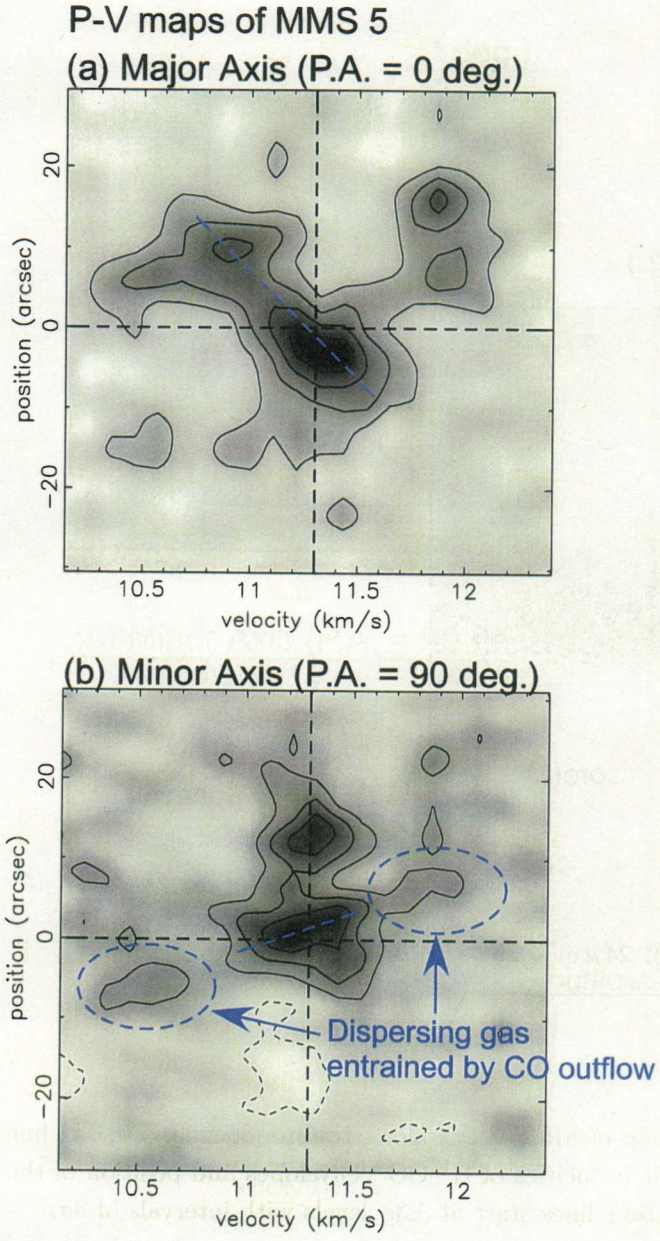

Fig. 16.— $H^{13}CO^+$(1–0) position-velocity maps of MMS 5 cut along the major (a) and major axis(b), respectively. Dashed line of vertical and horizontal axis show a systemic velocity of $H^{13}CO^+$ envelope and position of the 3.3 mm emission peak, respectively. The contour lines start at $\pm 3\sigma$ levels with intervals of 3σ.

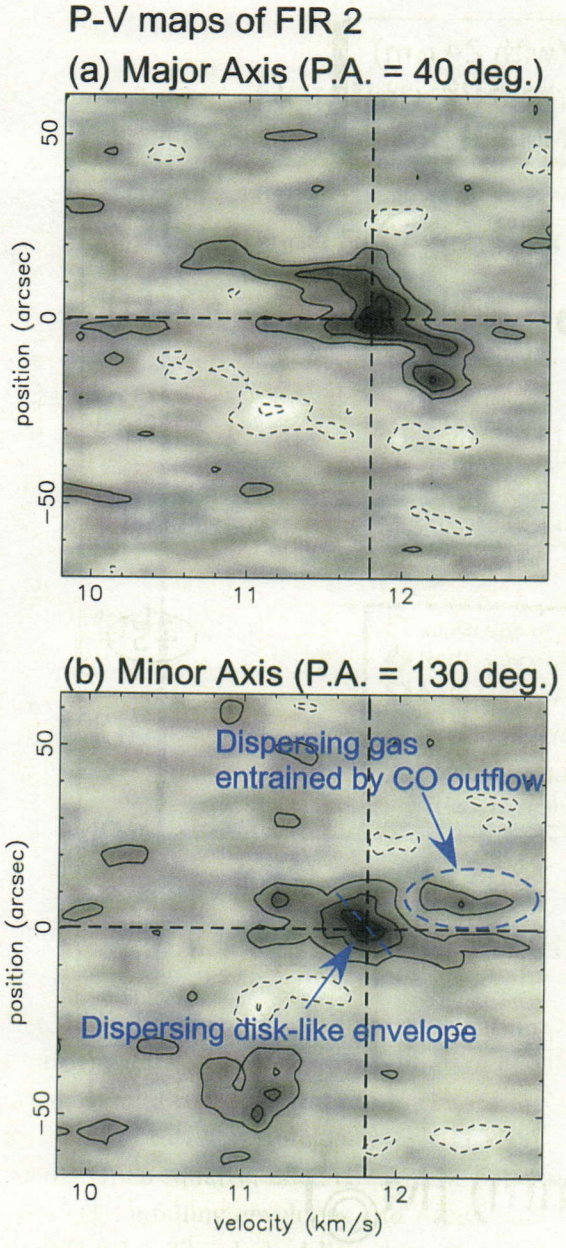

Fig. 17.— $H^{13}CO^+(1–0)$ position-velocity maps of FIR 2 cut along the major (a) and major axis(b), respectively. Dashed line of vertical and horizontal axis show a systemic velocity of $H^{13}CO^+$ envelope and position of the 3.3 mm emission peak, respectively. The contour lines start at $\pm 3\sigma$ levels with intervals of 3σ.

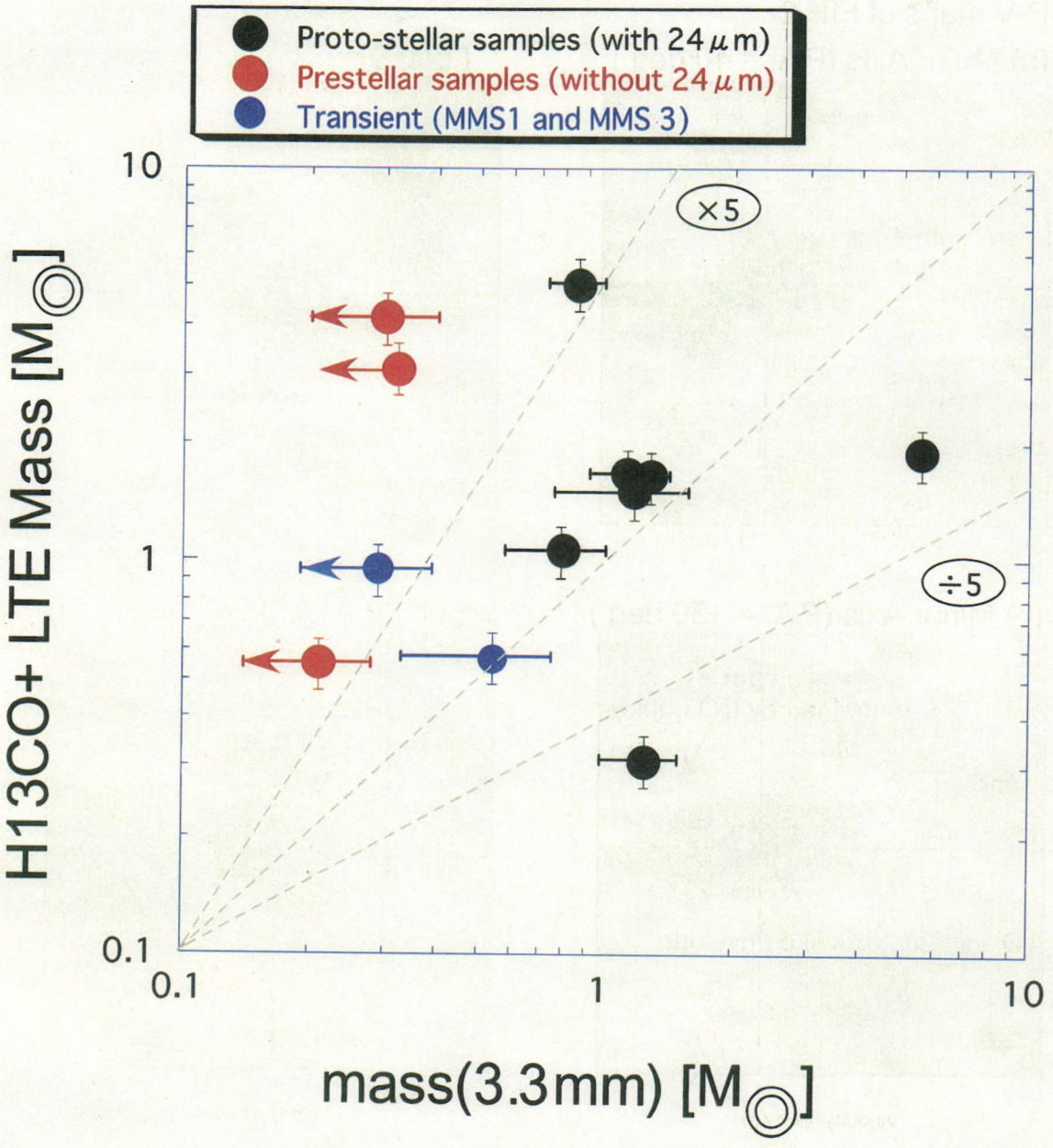

Fig. 18.— $H^{13}CO^+$ LTE mass plotted as a function of the mass derived from NMA- 3.3 mm continuum emission. Black, red and blue plots represent data of protostellar (with 24 μm source), prestellar (without 24 μm source), and transient (i.e., MMS 1 and MMS 3) samples, respectively

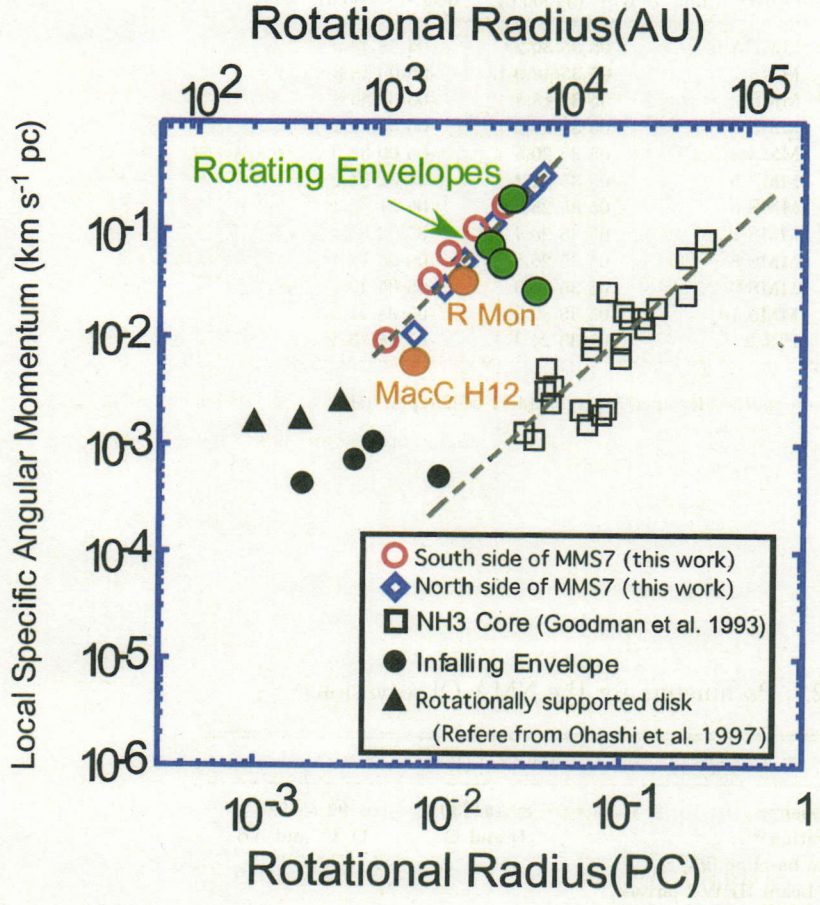

Fig. 19.— Local specific angular momentum plotted as a function of the radius. Filled green circles represent data from this work (the data of SIMBA a, MMS 1, MMS 3, MMS 5 in Table 9). Filled orange circles represent data from the Herbig Ae/Be samples (the data of B0-type star R Mon with a keplarian rotation from Fuente et al. 2006 and A5-type stars MacC H12 from Mannings et al. 2000). Open squares, filled circles, and filled triangles represent data from NH_3 cores (Goodman et al. 1993), infalling envelopes and rotationally supported disks in the Taurus (Ohashi et al. 1997), respectively. The dashed line show power-law fittings with an index of 1.6 to the results of NH_3 cores in low-mass stars and an index of 1.9 to the results of the $H^{13}CO^+$ disk-like envelope in MMS 7, respectively (refer from Chapter II).

Table 1. Observed Source with the NMA

ID[a]	Object Name	R.A. (J2000.0)	decl. (J2000.0)
1	SIMBA a	05 35 30.2	-04 58 48.0
10	MMS 1	05 35 18.0	-05 00 19.8
11	MMS 2	05 35 18.3	-05 00 34.8
12	MMS 3	05 35 19.2	-05 00 51.2
13	MMS 4	05 35 20.5	-05 00 53.0
14	MMS 5	05 35 22.4	-05 01 14.1
15, 16	MMS 6	05 35 23.3	-05 01 32.2
18	MMS 7	05 35 26.4	-05 03 53.4
19	MMS 8	05 35 26.5	-05 05 17.4
20	MMS 9	05 35 26.0	-05 05 42.4
21	MMS 10	05 35 32.3	-05 05 41.8
27	FIR 2	05 35 24.3	-05 08 33.3

[a]Based on source identification in Table 1 of Chapter III.

Table 2. Parameters for the NMA Observations

Parameter	$H^{13}CO^+$(1–0)	Dust Continuum
Rest frequency	86.754330	92.754330
Configuration [a]	D and C	D, C, and AB
Minimum baseline [kλ] [b]	~3	
Primary beam HPWB [arcsec]	77	
Velocity resolution [km s^{-1}]	0.11	—
Band width [MHz]	32	2048
Gain calibrator [c]	0531+135 and 0423-013	
Passband calibrator [d]	3C454.3, 0423-013 and 3C273	
Flux calibrator [e]	3C454.3, 0531+134 and 3C84	
System temperature in DSB [K] [f]	150 - 400	

[a]D and AB are the most compact and sparse configurations, respectively.

[b]Typical value.

[c]A gain calibrator, 0530+135, was observed every 20 minutes.

[d]The passband observations were archived by 40 minute observations of each calibrator.

[e]The flux of each calibrations was determined by the observations of the primary calibrator, Uranus.

[f]The system noise temperature of SIS receiver were measured toward the zenith.

Table 3. Beam Size and Sensitivity of the NMA Observations

ID	Field Center	Beam Size [arcsec]	P.A. [degree]	Map RMS[a] [Jy beam^{-1}]	Beam Size [arcsec]	P.A. [degree]	Map RMS[b] [mJy beam^{-1}]
		$H^{13}CO^+$ (1–0)			3.3 mm continuum		
1	SIMBA a	6.5 × 4.2	-23.7	0.08	5.3 × 3.3	-26.9	0.78
11	MMS 2	6.8 × 5.3	-3.43	0.12	5.0 × 4.3	-19.6	1.21
14	MMS 5	5.8 × 4.0	-24.0	0.13	4.8 × 3.4	-30.9	1.74
15, 16	MMS 6	6.0 × 3.2	-13.4	0.08	4.9 × 3.6	-30.2	1.23
18	MMS 7	6.8 × 4.3	-21.4	0.09	5.1 × 3.6	-25.2	0.79
20	MMS 9	6.8 × 5.5	-23.3	0.12	5.7 × 4.3	-29.6	1.17
21	MMS 10	5.7 × 3.7	-25.3	0.13	5.9 × 4.0	-22.4	1.00
27	FIR 2	7.2 × 4.9	-21.7	0.08	5.3 × 3.7	-26.7	0.86

[a]The rms noises were measured with the velocity width of 0.3 km s^{-1}.

[b]The rms noises were measured emission free region in the 3.3 mm maps before primary beam correction.

Table 4. Parameters for 45m Observations

Parameter	$H^{13}CO^+$(1–0)
Beam size in HPWB [arcsec]	18.5
Main beam efficiency	0.5
Mapping center	SIMBA a, MMS6, MMS 7 and MMS10
Mapping area [arcsec]	190×190
Grid spacing [arcsec]	8.22
Backend	Auto correlator
Velocity resolution [km s^{-1}]	0.11
System temperature in DSB [K] [a]	240
Pointing Object [b]	Orion KL [RA. = 5 h 35 m 14.5 s Dec = -05 d 22 m 30.4 s (J2000)]
RMS noise level	0.1 K (in T_a^*) [c]

[a]Typical value.

[b]The telescope pointing was checked every $\sim$ 90 minutes by five -point cross scans in the SiO($v = 1, J = 1 - 0$) maser emission using the SIS receiver.

[c]RMS noise level were measured to the velocity width of 0.1 km s^{-1}.

Table 5. Identification of 24 μm sources associated with the 1.3 mm sources

ID	Object Name	24 μm	Peak Intensity (Jy/ 5.8 $''$ beam)
1	SIMBA a	053530-045848	0.109
10	MMS 1	—	< 0.054[a]
11	MMS 2	053518-050034	> 0.625[b]
12	MMS 3	053519-050051	0.110
13	MMS 4	—	< 0.042[a]
14	MMS 5	053522-050115	0.211
15	MMS 6	053524-050130	0.332
16		053524-050140	0.578
18	MMS 7	053527-050355	> 0.711[b]
19	MMS 8	—	< 0.048[a]
20	MMS 9	053526-050546	0.117
21	MMS 10	—	< 0.101
27	FIR 2	053524-050831	0.496

[a]Did not detected any of compact sources, i.e., back ground emission.

[b]We measured lower limit of the 24 μm peak flux, because data were saturated in brightest part of the sources.

Table 6. Summary of $H^{13}CO^+$ Line taken with the 45 m Telescope

ID	Object Name	v_{sys} (km s^{-1})	$T_{B(peak)}$ (K)	$\Delta v_{\rm obs}$ in FWHM (km s^{-1})	$R_{\rm mean}$[a] (pc)	$T_{\rm dust}$[b] (K)	M_{virial}[c] ($M_\odot$)
1	SIMBA a (1)	12.7	1.34	1.13	0.064	20	11.1
1	SIMBA a (2)	11.8	1.14	0.53	—	—	—
10	MMS 1	11.5	2.66	0.72	0.028	20 –25	2.7 - 2.9
11	MMS 2	10.7	2.22	0.63	0.036	20	2.89
12	MMS 3 (1)	10.8	1.80	0.47	0.077	20	4.79
12	MMS 3 (2)	11.5	2.66	0.72	0.077	20	7.18
13	MMS 4	11.3	3.64	0.85	0.060	20 –25	6.9 - 7.5
14	MMS 5	11.3	5.08	0.77	0.038	20	3.8
15, 16	MMS 6	11.3	3.78	0.93	0.028	15 – 25	3.4 - 3.9
18	MMS 7	10.6	1.76	1.58	0.035	26	10.9
19	MMS 8	11.5	2.44	0.73	0.044	20	4.2
20	MMS 9	11.5 (?)	2.11	0.57	0.026	20	1.9
21	MMS 10	12.1	1.54	0.94	0.043	20	5.7

[a]Geometrical mean of the major and minor axis of the core, $R_{mean} = (R^2_{\rm min} + R^2_{\rm max})^{0.5}$

[b]From Chini et al. (1997)

[c]Core sizes are assumed the results of the single-dish observations(Chini et al. 1997), and kinetic temperatures are adopted value of dust temperature shown in Table 3.

Table 7. NMA 92 GHz Continuum Results

ID	Object Name	RA (J2000.0)	Dec (J2000.0)	$F_{3.3\ mm}$ (total)[a] (mJy)	Deconvolution Size[b] (AU)	P.A.[b] (deg)	T_{dust}[d] K	M_{H_2} (min.)[d] $M_\odot$	M_{H_2} (max.)[e] $M_\odot$
1	SIMBA-a	05 35 29.8	-04 58 50.0	28.25 ± 3.36	2200 × 1200	124.1	20	1.27 ± 0.16	3.61 ± 0.45
10	MMS 1	05 35 18.0	-05 00 17.3	15.32 ± 5.84	2300 × 1200	131.9	20 – 25	0.54 ± 0.21	1.96 ± 0.74
11	MMS 2	05 35 18.3	-05 00 34.6	17.67 ± 4.66	1500 × 1200	144.6	20	0.79 ± 0.21	2.26 ± 0.60
12	MMS 3	—	—	< 6.42 ± 2.14	—	—	20	< 0.29 ± 0.10	< 0.82 ± 0.27
13	MMS 4	—	—	< 6.75 ± 2.25	—	—	20	< 0.30 ± 0.10	< 0.86 ± 0.29
14	MMS 5	05 35 22.5	-05 01 14.4	25.95 ± 9.14	1800 × 1000	120.6	20	1.17 ± 0.41	3.32 ± 1.68
15, 16	MMS 6	05 35 23.4	-05 01 31.2	157.46 ± 7.26	1200 × 1000	144.6	15 – 25	5.53 ± 0.26	20.12 ± 0.92
18	MMS 7	05 35 26.5	-05 03 55.4	24.61 ± 3.36	1300 × 800	9.4	26 – 50	0.86 ± 0.13	3.14 ± 0.46
19	MMS 8	—	—	< 7.14 ± 2.38	—	—	20	< 0.32 ± 0.01	< 0.91 ± 0.03
20	MMS 9	05 35 26.0	-05 05 44.1	27.56 ± 5.87	2400 × 1000	146.3	20	1.24 ± 0.26	3.32 ± 0.75
21	MMS 10	—	—	< 4.62 ± 1.54	—	—	20	< 0.21 ± 0.07	< 0.59 ± 0.20
27	FIR 2	05 35 24.3	-05 08 29.8	24.84 ± 4.44	2800 × 1000	157.7	20	1.12 ± 0.20	3.17 ± 0.57

References. — 3.3 mm dust continuum parameters were derived from images taken with the NMA C and D configurations.

[a]Total fluxes were measured above 3 σ.

[b]Deconvolution size were derived from the 2-Dimensional Gaussian fitting to the image.

[c]From Chini et al. 1997, Johnstone et al. 2003.

[d]The mass opacities assumed β =1. Dust temperatures and total fluxes were adopted above value.

[e]The mass opacities assumed β =1.5. Dust temperatures and total fluxes were adopted above value.

Table 8. Summary of $H^{13}CO^+$ Line taken with the Nobeyama Millimeter Array

ID	Object Name	$F_\nu dv$ (Jy km s^{-1})	size (AU)	P.A. (deg)	M_{H_2} ($M_\odot$)
1	SIMBA (1)	96.07 ± 0.474	16600 × 8600	-25	1.65 ± 0.0082
1	SIMBA (2)	32.91 ± 0.376	11300 × 4500	-15	0.57 ± 0.0065
10	MMS 1	61.48 ± 0.893	9000 × 4100	-45	1.06 ± 0.0154
11	MMS 2	55.15 ± 0.594	13200 × 6600	0	0.95 ± 0.0102
12	MMS 3/4	240.88 ± 0.971	13200 × 10600	-130	4.15 ± 0.0167
14	MMS 5	87.10 ± 0.973	10600 × 5300	0	1.50 ± 0.0168
15, 16	MMS 6	109.84 ± 0.567			1.89 ± 0.0096
18	MMS 7	294.57 ± 0.793	16500 × 7500[a]	0	5.07 ± 0.0136
19	MMS 8/9	179.49 ± 0.762	14800 × 8400	20	3.09 ± 0.0131
20	MMS 9 (south)	18.17 ± 0.762	—	—	0.31 ± 0.0131
21	MMS 10	32.13 ± 0.790	6700 × 3500	0 – -30	0.55 ± 0.0136
27	FIR 2	97.26 ± 0.736	15000 × 3100[a]	-50	1.67 ± 0.0127

[a]Only measured centrally condensed component.

Table 9. Kinematics of $H^{13}CO^+$ Envelopes

ID colhead	Object Name	Dispersion	Rotation	Angular momentum[a] (km s^{-1} pc)	Expected infalling radius[b] (AU)
1	SIMBA (1)	N	Y	0.145	2900
1	SIMBA (2)[c]	N	N	—	—
10	MMS 1	N	Y	0.053	—
11	MMS 2	Y[d]	N	—	4800
12	MMS 3/4	N	Y?[e]	0.380	—
14	MMS 5	Y [f]	Y	0.097	750
15, 16	MMS 6[g]	—	N	—	—
18	MMS 7	Y[h]	Y	—	5500
19	MMS 8	N	N	—	—
20	MMS 9	N[i]	N	—	4600
21	MMS 10	—	N	—	—
27	FIR 2	Y[j]	N	—	1000

[a]Averaged angular momentum of the $H^{13}CO^+$ envelope derived by $M_{\rm total} \times R_{\rm FWHM} \times \Delta V_{\rm FWHM}$

[b]Infalling radius are derived by $C_s \times t_{\rm CO\ dyn}$

[c]Prestellar core

[d]Gas dispersion perpendicular to the outflow axis

[e]Rotation with two cores (i.e., along core(1) to core(2))

[f]Gas dispersion perpendicular to the outflow axis

[g]Proto-cluster

[h]Gas dispersion along and perpendicular to the outflow axis

[i]No significant gas

[j]Gas dispersion along and perpendicular to the outflow axis

Chapter V

Summary; Structure and Evolution of Intermediate-mass Protostars in the Orion Molecular Cloud -2 and -3 Region

1. Evolutionary Scenario of Intermediate-mass Protostars in the OMC-2/3 region

In order to reveal formation and evolution of intermediate-mass protostars, the author have performed outflow survey in CO(3–2) emission with ASTE and JHK_s observations with the SIRIUS/IRSF, and also performed dense core survey in the $H^{13}CO^+$ and 3.3 mm continuum emission with the NMA toward one of the intermediate-mass star-forming regions, OMC-2/3. As a result of dense core survey, the author revealed varieties of distribution, morphology and kinematics of pre- and proto-stellar envelopes in the $H^{13}CO^+$ and 3.3 mm continuum. In addition, from CO(3–2) unbiased survey, the author succeeded to identify the outflow associated with the intermediate-mass protostars without contamination of the ambient molecular cloud. Further the author found that the CO outflow momentum increase with the enhancement of the 24 μm flux which is caused by the growth of the NIR cavity. In this section, the author will discuss the comprehensive evolutionary scenario of intermediate-mass protostars in the OMC-2/3 region combining the results of our outflow, dense envelope survey and archived and published multi-wavelength data.

1.1. Evolutionary Diagnoses with the multi-wavelength Data

In order to discuss the evolutionary sequence of the intermediate-mass protostars, the author used five independent multi-wavelength data (i.e., our 3.3 mm continuum emission, CO(3–2) emission and JHK_s data taken by SIRIUS/IRSF, archive 24 μm Spitzer data, and published VLA- 3.6 cm data from Reipurth et al. 1999). 3.3 mm and 24 μm compact continuum sources trace a region, which is dense ($\geq 10^7$ cm^{-3}) and hot ($>$ 150 K) inner envelope associated with the protostars. Reflection nebula (i.e., cavity-like structure along the molecular outflow) in JHK_S images related to the dissipation of circumstellar material. Further free-free jet traced by the VLA-3.6 cm emission reflects an activity of central jet. In addition, an enhancement of the size of the CO outflow reflects a growth of the molecular outflow (see Chapter III). The author considers that the evolution of the intermediate-mass protostars are classified observed samples in three categories as "pre-stellar", "Class A" and "Class B"

"Pre-stellar" sources have no 3.3 mm and 24 μm compact sources above 3 σ signal level, suggesting no any signature of the dense and hot inner envelope. Upper-limit of average densities estimated by the 3.3 mm compact dusty component, several $\times$ 10^6 cm^{-3}, is typically one order of magnitude less than that of proto-stellar samples. In this phase, there is no signature of jet and outflow. These objects associated with the relatively extended $H^{13}CO^+$ (1–0) component(s) at a size scale of 0.01 to 0.1 pc, which are gravitationally bound.

"Class A" sources are associated with 3.3 mm and faint 24 μm compact sources, suggesting the presence of the dense and hot envelope. Further 0.1 pc-scale CO outflow are detected toward the objects. These results imply that protostars are already formed in central region and may begin mass accretion, although the author did not detect mass accretion directly. The $H^{13}CO^+$ intensity map has a peak near (or at) the position of 3.3 mm source. The velocity gradient along the major axis is detected in the $H^{13}CO^+$ envelope, suggesting the rotational motion of $H^{13}CO^+$ envelope. The author detected a velocity gradient along the CO outflow (i.e., minor axis of disk-like envelope). This result may imply an evidence that the outer portion of the $H^{13}CO^+$ envelope are entrained by the CO outflow. In this phase, the author did not detect signature of

the free-free jet and reflection nebula.

"Class B" sources are associated with 3.3 mm and bright 24 μm compact sources, suggesting presence of the dense and hot envelope. Both of a 0.5 – 1.0 pc scale of CO outflow and free-free jet are associated with the objects. In addition, JHK_s images show reflection nebula around the heating source, suggesting the formation of the cavity along the outflow axis. Fan-shaped $H^{13}CO^+$ envelopes with a size scale of 0.1 pc have been observed in this status. The peak position of $H^{13}CO^+$ emission does not coincide with the 3.3 mm continuum emission.

In the above classification, pre-stellar sources are SIMA a (2), MMS 4, MMS 8, and MMS 10. Class A source are SIMBA a (1), MMS 5 and FIR 2, and Class B source are MMS 2, MMS 7 and MMS 9. This classification only apply to the single (or binary) system. Here, the author excepts MMS 6 in this categorization, because of protocluster candidate.

From these results, the author considers that the above classification with observational results support the formation scenario of the intermediate-mass protostars with dissipating processes of circumstellar materials. Since protostars are formed in densest region ($\geq 10^7$ cm^{-3}) traced by the 3.3 mm continuum emission taken with the NMA, inner hot envelopes are observed by the 24 μm emission. Class A is corresponding to the earlier evolutionary stage of the proto-stellar cores. $H^{13}CO^+$ emission are associated with the protostar with a rotating motion. In this phase, small scale outflow with a size scale of 0.1 pc are observed. Class B is corresponding to the later evolutionary stage of the proto-stellar cores. An expanding motion at the outer portion of the $H^{13}CO^+$ gas toward Class B samples, MMS 2 and MMS 7 were detected in this phase. Particularly, one of the Class B sources: MMS 7, the $H^{13}CO^+$ envelope is already gravitationally unbound, and gas dispersion is not only along the outflow axis but also perpendicular to the outflow axis with a significant mass outflow rate of $\sim 10^{-5}$ $M_\odot$ yr^{-1}. On the other hand, the author did not detect significant $H^{13}CO^+$ emission toward MMS 9, implying effect of depletion or dissipation of the dense gas. In this phase, large scale outflow (0.5 – 1 pc) are observed.

Figure 1 summarized a schematic picture of evolutionary sequence of the intermediate-mass protostars. and the author also listed properties of our observing sources (i.e., evolutionary status of each source) in Table 1. The author identified MMS 1, which is associated with the 3.3 mm emission but no 24 μm source, and MMS 3, which is associated with the 24 μm, source but no 3.3 mm emission, as "exception " objects in this categorization. Especially, the author considers that MMS 1 may trace a "transient phase" of pre-stellar to Class A.

1.2. Physical Nature and Evolution of intermediate-mass protostars

As a next step, the author focuses the evolution of physical properties of the protostellar samples. Figure 2 shows 24 μm flux density plotted as a function of the outflow momentum derived from identified CO (3–2) outflows (see Chapter III). The author already mentioned enhancement of the 24 μm flux density with the outflow evolution in Chapter III. In addition, the author separates these plots by different colors in evolutionary sequence from Class A and Class B, although limited samples. The author found that the proposed evolutionary scenario follows the enhancement of 24 μm and outflow momentum in the evolutionary sequence of Class A to B. This result is closely related to the dissipation of circumstellar materials. In fact, as mentioned Section 5.1, $H^{13}CO^+$ envelope are dissipate as the core evolutionary sequence from Class A to Class B. Further JHK_s band images also show a bright reflection nebula, which is closely

related to the formation of cavity along the outflow axis, in later evolutionary phase of protostars (denoted by black filled circles in Figure 2). These results suggest that the dissipation of the circumstellar materials and growth of the molecular outflow play an essential role in evolution of the intermediate-mass protostars. In addition, the author did not detect the gradient of the evolutionary sequence along the OMC filament as shown in Figure 3.

2. Summary

The author have newly performed a survey of millimeter-, submillimeter-, and near infrared-wave observations using the NMA, ASTE and IRSF/SIRIUS toward the Orion Molecular Cloud -2 and -3 region, to understand formation and evolution of intermediate-mass protostars. The main results are summarized as follows.

- **Outflows associated with the intermediate-mass protostars**
  Using the ASTE and SIRIUS/IRSF, the author has performed an extensive outflow search in the submillimeter CO(3–2) emission and at JHK_s toward 43 protostellar candidates in the OMC-2/3 region. The author totally identified 15 outflows, including eight newly identified outflows. Detected CO outflows typically contain mass of 0.08 $M_\odot$, and momentum rates of 1.0×10^{-4} $M_\odot$ km s^{-1} yr^{-1}, which are one order of magnitude larger than those of low-mass counterpart in Taurus. Comparing the estimated CO outflow momentum and Spitzer 24 μm flux, which is roughly correlated, the author has revealed a correlation between the outflow evolution and the dissipation of the circumstellar material associated with the intermediate-mass protostars.
- **Evolutionary scenario of intermediate-mass protostars.**
  Using the high-resolution capabilities offered by the NMA, the author observed 3.3 mm dust continuum and $H^{13}CO^+$(1-0) emission in 12 pre- and proto-stellar candidates identified previously in single-dish millimeter observations, which are a part of objects of 43 protostellar candidates mentioned above. Based on our $H^{13}CO^+$, 3.3 mm continuum, CO(3–2) outflow and JHK_S results, combined with the published VLA 3.6 cm and archived 24 μm data taken by the Spitzer, the author unveiled the evolutionary changes of morphology and velocity structure of the dense envelope, and accompanied CO outflow around intermediate-mass protostars for the first time. The author classified these intermediate-mass pre- and protostellar candidates into three evolutionary phases: (the author)Prestellar phase, (ii) Class A which is a earlier evolutionary stage of proto-stellar cores with a 0.1 pc scale compact outflow, and (iii) Class B which is a later stage of proto-stellar cores with a dispersing dense envelope and 0.5 – 1 pc scale giant CO outflow. Our survey results suggest that dissipation of the dense gas envelope plays an important role in the evolution of the intermediate-mass protostars.
- **Kinematics of the dense envelope traced by the $H^{13}CO^+$ emission** NMA observations in the $H^{13}CO^+$(1–0) emission revealed the velocity gradient along the major and minor axis of the dense gas envelope with a size scale of 0.1 pc. From our survey for 12 sources, five sources (i.e., SIMBA a(1), MMS 1, MMS 3, MMS 5 and MMS7) show the rotating motion. Estimated angular momenta in OMC-2/3 samples are typically one order of magnitude larger than those of low-mass counterpart. In 4/12 objects in Class A and Class B sources (i.e., MMS 2, MMS 5, MMS 7 and FIR 2), the author detected the velocity gradient along the minor axis, suggesting the dispersing (destructing) motion at the outer portion of the dense envelope along and perpendicular to the CO outflow axis. On the other hand, the author did not detect any clear evidence of dynamical mass accretion toward the central protostar in the $H^{13}CO^+$ emission.
- **Comprehensive view of the formation and evolution of the intermediate-mass stars** From our survey and previous observations of Herbig Ae/Be stars, the author proposes the evolutionary scenario of intermediate-mass protostars as follows; Intermediate-mass star are formed in a dense cloud traced by the $H^{13}CO^+$ emission with a typical mass and size

scale of 10^5 cm^{-3} and 0.1 pc scale, respectively. When the average density of the central region with a size scale of a few $\times$ 1000 AU becomes higher than $\geq 10^7$ cm^{-3}, 3.3 mm and 24 μm source are observed in the central region which is a signature of the heating source. Once the central star is formed, proto-stellar core evolves with a significant dissipation of dense gas traced by the $H^{13}CO^+$ emission. In fact, the author detected the dispersing motion of the $H^{13}CO^+$ envelope toward 4/6 of protostellar samples. With the dense core evolution, the associated CO molecular outflow grow. Further with the outflow growth, the 24 μm flux density also increase as an evolutionary sequence, caused by the growth of the cavity. These phenomena are consistent with the dense core dissipation. It is considered that the time scale of the intermediate-mass protostars are $\sim$ 0.1 Myr (Fuente et al. 2002). With dense core evolution, the outflow activities have been dispersing the surrounding envelope as shown in Figure 1. Finally, a visible central star appears, that is, "Herbig Ae" stars. The evolutionary scenario of the after Herbig Ae stars are proposed by Fuente et al. (2002) with the observations of ^{13}CO(1–0) emission which can trace a more diffuse region ($\sim 10^3$ cm^{-3}) of the molecular cloud than $H^{13}CO^+$ emission as mentioned Chapter I.2 (also see Figure I-2). In a few 0.1 Myr, the star becomes visible and the outflow fades. Some material is dispersed from $\sim$ a few 0.1 to 1 Myr. Since the outflow declines and the stars are still too cold to generate UV photons, stellar winds are expected to be the only dispersal mechanism. In $>$ 1 to 10 Myr late-type intermediate-mass stars (later than B6) meets the ZAMS. The star is hot enough to produce UV photons and stars excavating the molecular cloud. Intermediate-mass stars become the ZAMS several to one-order of faster than low-mass young stars with a significant mass loss. Figure 4 shows the schematic picture of the evolutionary sequence between low- and high-mass YSOs as already shown in Figure I-1. In this Figure, we newly proposed the evolutionary scenario of intermediate-mass protostars (i.e., before Herbig Ae phase) as Class A and Class B.

□ **Comparison with the evolutionary sequence between low- and intermediate-mass YSOs** Figure 5*a* and *b* show the schematic picture of the core mass and outflow activity plotted as a function of YSOs evolution, respectively. The author compared the each parameter between low- and intermediate-mass YSOs. Because of the limitation of the observations and analysis, it is difficult to compare the absolute value directly in each parameter. The author, here, described the peak values of each value as unit. As mention follows, the evolution processes of the intermediate-mass protostars are quantitatively different, but qualitatively similar.

- **Dissipation processes of circumstellar gas** In the case of low-mass starformation, dense gas traced by the $H^{13}CO^+$ (1–0) emission associated with the protostars dissipates during Class 0 to Class I with a time scale of several $\times$ 10^5 yr (Saito et al. 2001). After that, surrounding diffuse gas traced by the ^{13}CO(1–0) emission are dissipated by a stellar wind or molecular outflow in Class II phase (e.g., Kitamura et al. 1998). Finally central star meets ZAMS with a time of around several $\times 10^7$ yr. On the other hand, in the case of intermediate-mass starformation, dense gas trace by the $H^{13}CO^+$ emission factor of faster than dissipates low-mass counterparts with a time scale of less than 10^5 yr (this work). After that, surrounding diffuse gas traced by the ^{13}CO(1–0) emission are dissipated by a stellar wind or molecular outflow and that the central star meets ZAMS between 10^6 to 10^7 yr (Fuente et al. 2002 as mentioned above paragraph). The mass of natal cores associated with the intermediate-mass stars are typically one-order of magnitude larger than low-mass counter parts.

– **Outflow Activities** In the previous low-mass studies, the outflow activity reflects the corresponding decay in the accretion/infall rate from Class 0 to Class I (i.e., $F_{CO} - L_{bos}$ correlation by Bontemps et al. 1996). On the other hand, outflows associated with the intermediate-mass protostars in OMC-2/3 suggest opposite sence. In other word, outflow activities seems to be enhanced with the protostar evolution with an age of several $\times 10^3 - 10^4$ yr. One possible explanation is that our sample traces the earliest stage of protostellar cores. In fact, derived dynamical time scale of the outflow are typically one order of magnitude smaller than low-mass counterpart, $10^4 - 10^5$ yr. Our results imply the possibility of the evolutional processes of the CO outflows.

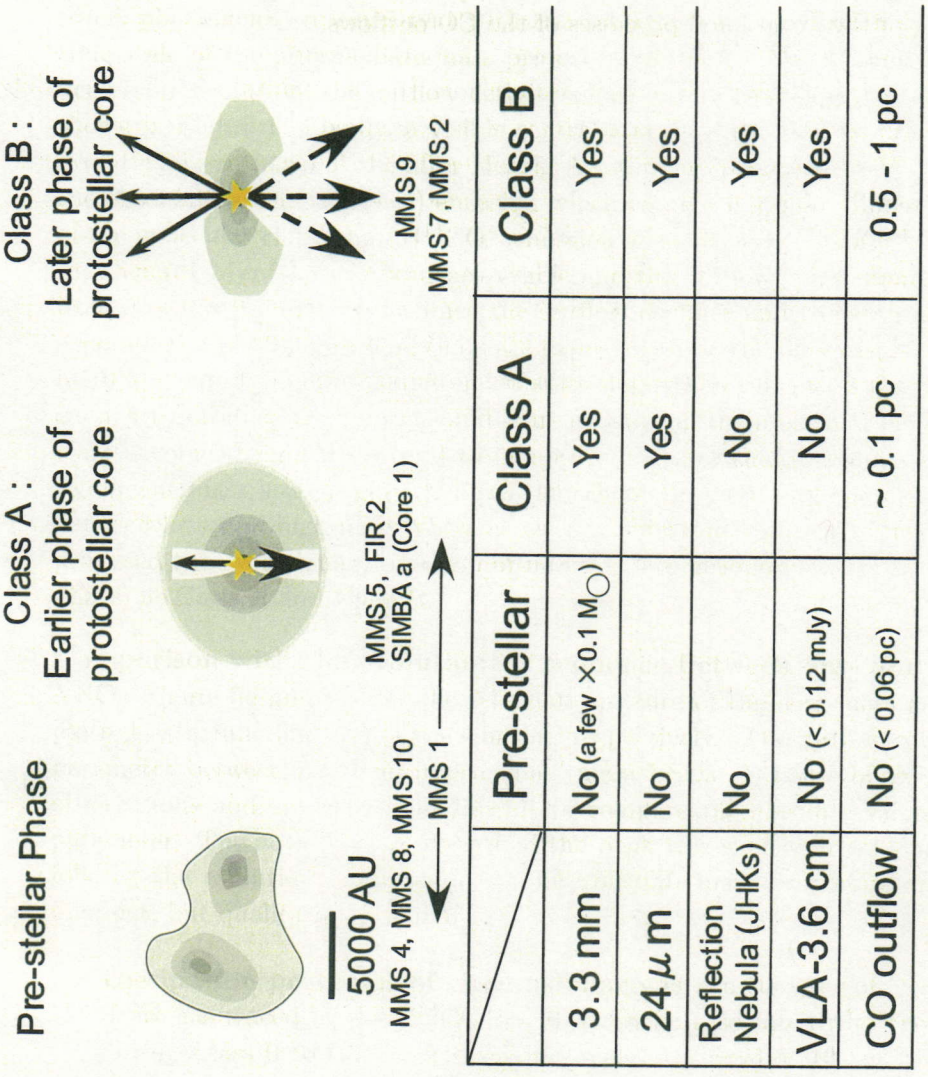

	Pre-stellar	Class A	Class B
3.3 mm	No (a few ×0.1 $M_\odot$)	Yes	Yes
24 μm	No	Yes	Yes
Reflection Nebula (JHKs)	No	No	Yes
VLA-3.6 cm	No (< 0.12 mJy)	No	Yes
CO outflow	No (< 0.06 pc)	~ 0.1 pc	0.5 - 1 pc

Fig. 1.— Schematic Picture of Evolutionary Scenario in Intermediate-mass Protostars

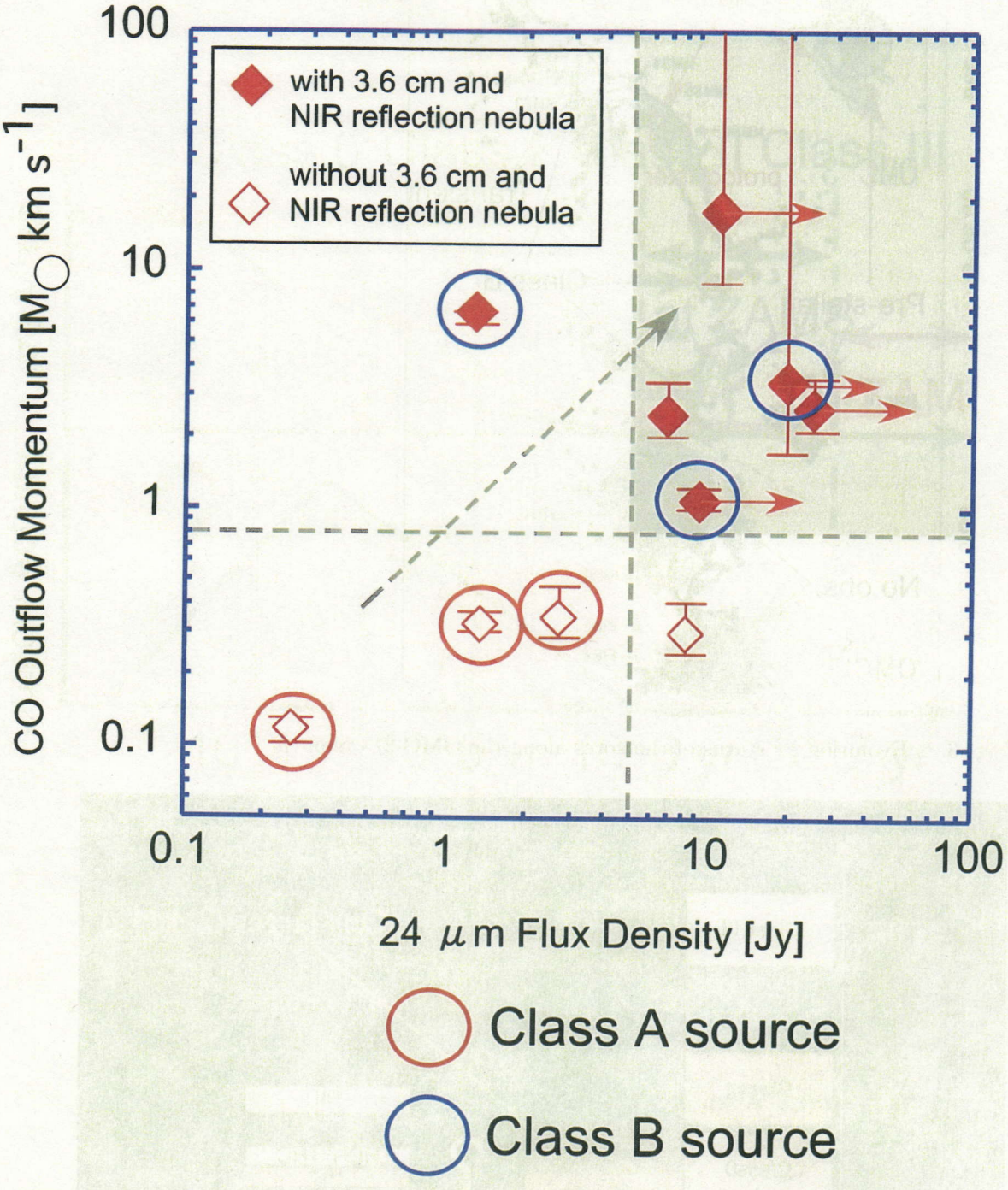

Fig. 2.— 24 μm peak density plotted as a function of outflow momentum derived from CO (3–2) observations.

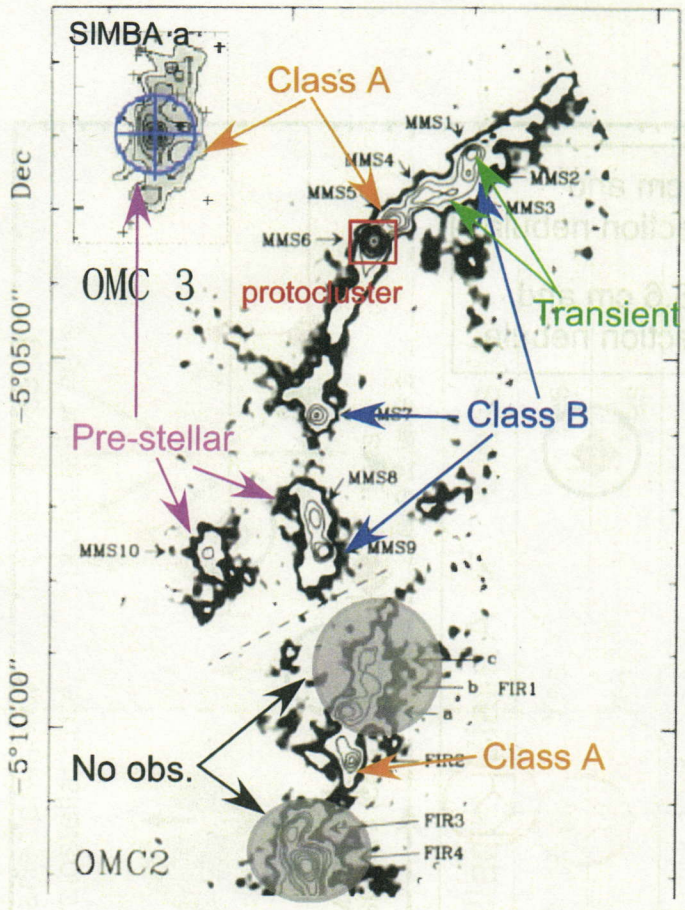

Fig. 3.— Evolutionary status of the cores along the OMC-2/3 filament

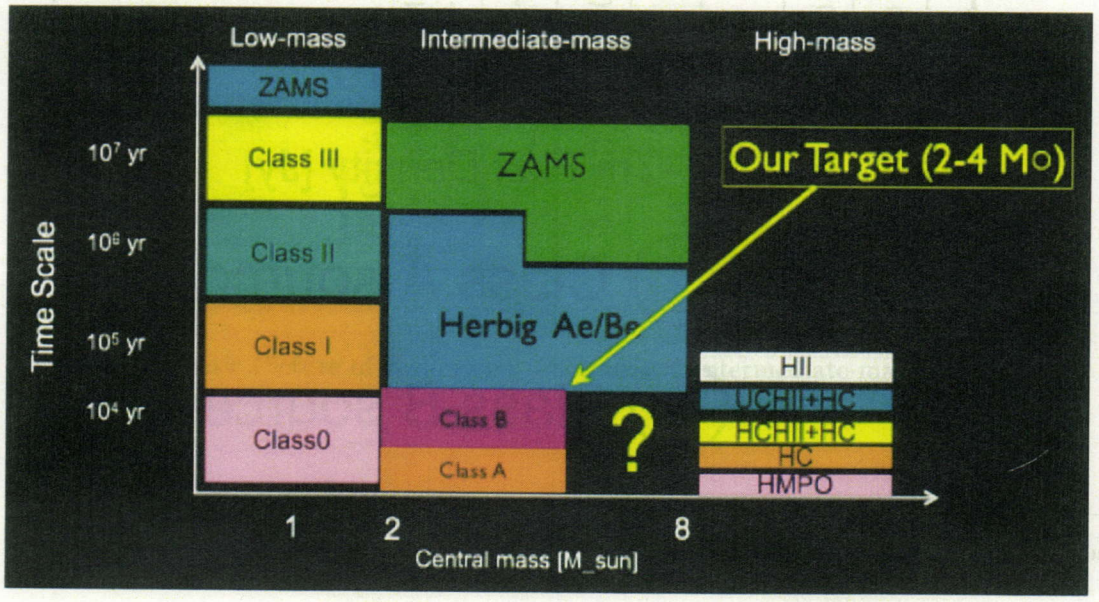

Fig. 4.— Schematic picture of the evolutionary sequence between low- and high-mass YSOs

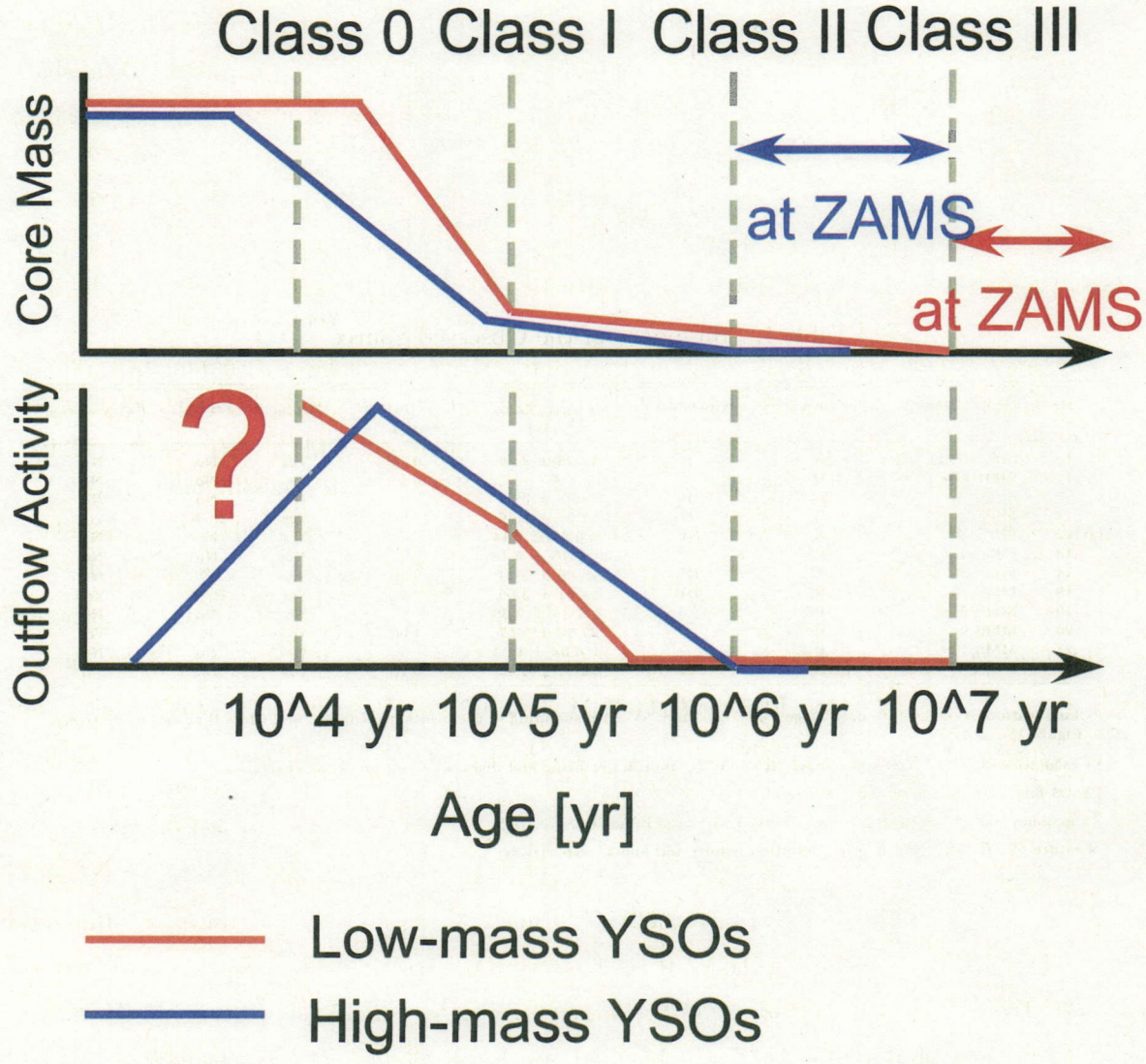

Fig. 5.— Schematic picture of the core mass (*top panel*) and the outflow activity (*bottompanel*) plotted as a function of YSOs evolution, respectively.

Table 1. Summary of the Observed Source

ID	Object Name	Classification[a]	Kinematics[b]	$F_{3.3mm\ (total)}$[c] (mJy)	CO Outflow[d] (pc)	$F_{24\mu m}$	JHK_s[e]	$F_{VLA-3.6cm}$
1	SIMBA (1)	A	R	28.25 ± 3.56	0.14	Yes	No	No
1	SIMBA (2)	P	—	—	—	—	No	No
10	MMS 1	P	R	15.32 ± 5.84	—	No	No	No
11	MMS 2	B	D	17.67 ± 4.66	0.62	Yes	R, K	Yes
12	MMS 3	A	R	< 6.42 ± 2.14	—	Yes	No	No
13	MMS 4	P	—	< 6.75 ± 2.25	—	No	No	No
14	MMS 5	A	DR	25.95 ± 9.14	0.10	Yes	K	No
18	MMS 7	B	DR	24.61 ± 3.56	0.98	Yes	R, K	Yes
19	MMS 8	P	—	< 7.14 ± 2.38	—	No	No	No
20	MMS 9	B	—	27.56 ± 5.87	1.00	Yes	K	Yes
21	MMS 10	P	—	< 4.62 ± 1.54	—	No	No	No
27	FIR 2	A	D	24.84 ± 4.44	0.10	Yes	No	No

[a]Classification of the evolutionary stage; "P", "A", and "B" corresponding to the prestellar, Class A and Class B phase, respectively (see Figure 1).

[b]Kinematics of the $H^{13}CO^+$ envelope; "R" and "D" indicate rotating and dispersing motion of the envelope.

[c]Total flux were measured above 3 σ level.

[d]Maximum size of CO (3–2) outflow observed with ASTE (see Chapter III).

[e]Feature of JHK_s; R and K show reflection nebula and knots, respectively.

References

Adams, F. C., Lada, C. J., & Shu, F. H. 1987, ApJ, 312, 788

André, P., Ward-Thompson, D., & Barsony, M. 1993, ApJ, 406, 122

Anglada, G., 1995, RMxAC, 1, 67

Anglada, G., Villuendas, E., Estalella, R., Beltran, M. T., Rodriguez, L. F., Torrelles, J. M., & Curiel, S., 1998, ApJ, 116, 2953

Arce, H. G., & Sargent A. I., 2006, ApJ, 646, 1070

Arce, H.G., Shepherd, D., Gueth, F., Lee, C.-F., Bachiller, R., Rosen A., & Beuther, H., Protostars and Planets V, B. Reipurth, D. Jewitt,and K. keil (eds), University of Arizona Press, Tuson, 951, p.p, 2007

Aso, Y., Tatematsu, K., Sekimoto, Y., Nakano, T., Umemoto, T., Koyama, K., & Yamamoto S., 2000, ApJ, 131, 465

Bachiller, R., & Tafalla, M., The Origin of Stars and Planetary Systems. Edited by Charles J. Lada, and Nikolaos d. Kylafis. Kluwer Academic Publishers, 1999, p227

Beichman, C. A., Myers, P. C., Emerson, J. P., Harris, S., Mathieu, R., Benson, P. J., & Jennings, R. E. 1986, ApJ, 307, 337

Belloche, A., Andre, P., & Motte, F., 2001, ASPC, 243, 313

Beltran, M. T., Cesaroni, R., Codella, C., Testi, L., Furuya, R. S., Olmi L., 2006, Nature, 443, 427

Bergin, E.A., Alves, J., Huard, T., & Lada, C. J., 2002, ApJ, 570L, 101

Beuther, H., Churchwell, E, B., McKee, C. F., & Tan, J. C., 2007, Protostar and Planets V, B. Reipurth, D. Jewitt, and K. Keil (eds.), University of Arizona Press, Tucson, 951 pp., 2007., p 165

Bonnel, I.A., Matthew, R., Zinnecker, H., 1998, MNRAS, 298, 93,

Bontemps, S., Andre, P., Terebey, S., & Cabrit, S., 1996, A&A, 311, 858

Bourke, T. L., Myers, P. C., Robinson, G., Hyland, A. R., ApJ, 554, 916

Butner, H. M., Evans, N.J. II, Lester, D.F., Levreault R.M., & Strom, S. E. 1991, ApJ, 376, 636

Caselli, P., Walmsley, C. M., Tafalla, M., Dore, L., & Myers, P. C., 1999, ApJ, 523L, 165

Cesaroni, R., & Wilson, T. L., 1994, A&A, 281, 209

Cesaroni, R., Galli, D., Lodato, G., Walmsely, C.M., & Zhang, Q., Protostars and Planets V, B.Reipurth, D. Jewitt, and K. Keil (eds.), University of Arizona Press, Tucson, 951, pp., 2007

Chini, R,. Ward-Thompson, D,. Bally, J,. Nyman, L.-Å., Sievers, A,. & Billawala, Y,. 1997, ApJ, 474, L135

Cohen, M., Emerson, J.P., & Beichman, C.A., 1989, ApJ, 339, 455

Curiel, S., Canto, J., & Rodriguez, L.F., 1987, RMxAA, 14, 595,

Curiel, S., Rodriguez, L.F., Canto, J., & Torrelles, J.M., 1989, RMxAA, 17, 137

Crutcher, R.M., 1999, ApJ, 520, 706

di Francesco, J., Evans, N.J., II, Caselli, P., Myers, P.C., Shirely, Y., Aikawa, Y., & Tafalla, M., 2007, Protostars and Planets V, B. Reipurth , D. Jewitt, and K keil (eds.), University of Arizona Press, Tucson, 951, pp., 2007

Ezawa, H., Kawabe, R., Kohno, K., & Yamamoto, S., 2004, SPIE, 5489, 763

Emerson, D. T., & Graeve, R., 1998, A&A, 190m 353

Frerking, M. A., Langer, W. D., & Wilson, R. W., 1982, ApJ, 262, 590

Fuente, A., Martin-Pintado, J., Bachiller, R., Rodriguez-Franco, A., & Palla, F., 2002, A&A, 387, 977

Fuente, A., Rizzo, J.R., Caselli, P., Bachiller, R., & Henkel, C. 2005, A&A, 433,535

Fuente, A., Alonso-Albi, T., Bachiller, R., Natta, A., Testi, L., Neri, R., & Planesas, P., 2006, A&A, 649,L119

Genzel, R. & Stutzki, J., 1989, ARA&A, 27, 41

Goch, R. E., 1995 in ASP conf. ser. 77, Astronomical Data Analysis Software and System IV, ed. R.A. Shaw, H. E. Payne, & J. J. E. Hayes (San Francisco: ASP), 144

Goodman, A. A., Benson, P. J., Fuller, G. A., Myers, P. C., ApJ, 406, 528

Guilloteau, S., & Dutrey, A., 1998, A & A, 339, 467

Hayashi, C., 1966, ARA&A, 4, 171,

Hayashi, M., Ohashi, N., & Miyama, S, M,. 1993, ApJ, 418, L71

Haro, G. 1953, ApJ, 117, 73

Hillenbrand, L. A., Meyer, M.R., Strom, S. E., & Skrutskie, M. F., 1995, AJ, 109, 280

Hogerheide, M., van Dishoeck, E. F., Blake, G.,A., van Langevelde, H. J., 1998, ApJ, 502, 315

Houde, M., Dowell, C. D., Hildebrand, R. H., Dotson J. L., Vaillancourt, J. E., Phillips, T. G., Peng, R., & Bastine, P., 2004, ApJ, 604, 717

Johnstone, D., & Bally, J., 1999, ApJ, 510L, 49

Johnstone, D., Boonman, A. M. S., & van Dishoeck, E. F., 2003, A&A 412, 157

Kamazaki, T., Ezawa, H., Tatematsu, K., Yamaguchi, N., Kuno, N., Morita, K., Yanagisawa, K., Horigome, O., & Maekawa, J., 2005, ASPC, 347, 533

Kawabe, R., Ishiguro, M., Omodaka, T., Kitamura, Y., & Miyama, S. M., 1993, ApJ, 404L, 63

Kenyon, S.T., & Hartmann, L., 1990, ApJ, 349, 197

Kenyon, S.T., Calvet, N., & Hartmann, L., 1993, ApJ, 414, 676

Kenyon, S.T., Gomez, M., Marzke, R. O., & Hartmann, L., 1994, ApJ, 180, 251

Kitamura, Y., Kawabe, R., & Saito, M., 1996, ApJ, 457, 277

Kitamura, Y., Momose, M., Yokogawa, S., Kawabe, R., Tamura, M., & Ida, S.,, ApJ, 581, 357

Kohno, K., Yamamoto, S., Kawabe, R., Ezawa, H., Sakamoto, S., Ukita, N., Hasegawa, T., et al. 2004, dimg. conf 349,

Lada, C. J., & Wilking, B. A., 1984, ApJ, 287, 610

Lada, C. J. 1991, in The Physics of Star Formation and Early Stellar Evolution, ed. C. J. Lada & N. D. Kylafis, Dordrecht: Reidel, 1991, 329

Lada, C. J., & Lada, E. A., 2003, ARA&A, 41, 57

Larson, R. B. 1969, MNRAS, 145, 271

Larson, R. B. 1969, MNRAS, 145, 297

Leung, C. M., Herbst, E., & Huebner, W. F. 1984, ApJS, 56, 231

Sawada et al. 2007, to be submitted in PASJ.

Shimajiri, Y., in a master thesis (University of Tokyo, Japan, 2007)

Shu, F. H. 1977, ApJ, 214, 488

Li, Z.-Y., & Nakamura, F., 2006, ApJ, 640L, 187

Lis, D.C., Serabyn, E., Keene, J., Dowell, C.D., Benford, D. J., Phillips, T. G., Hunter, T. R., & Wang, N., 1998, ApJ, 509, 299

Mannings, V., & Sargent, A.I., 2000m ApJ, 529, 391

Matthews, B. C., Lai, S-P., Crutcher, R.M., & Wilson, C. D., 2005, ApJ, 626, 959

Matthews, B. C., & Wilson, C. D., 2000, ApJ, 531, 868

McKee, C. F., & Tan, J.C., 2003, ApJ, 585, 850

Momose, M., Ohashi, N., Kawabe, R., Nakano, T., & Hayashi, T., 1998, ApJ, 504, 314

Myers, P. C., & Goodman, A. A., 1998a, ApJ, 324, 907

Myers, P. C., & Goodman, A. A., 1998b, ApJ, 326L, 27

Myers, P. C., Evans, N. J., II, & Ohashi, N., 2000, Protostars and Planets IV (Book- Tuson: University of Arizona Press; eds Mannings, V., Boss, A.P., Russell, S.S.), p.271

Nakazato, T., Nakamoto, T., & Umemura, M., 2003, ApJ, 583, 322

Nagashima C., Nagayama, T., Nakajima, Y., Tamura, M., Sugitani, K., Nagata, T., Hirao, T., Nakaya, H., Yanagisawa, K., & Sato, S., 1999, sf99.proc, 397

Nagayama, T., NagashimaC., Nakajima, Y., Nagata, T., Sato, S., Nakaya, H., Yamamuro, T., Sugitani, K., & TamuraM., 2003, SPIE, 4841, 459

Nakajima, Y., Kato, D., Nagata, T., Tamura, M., Sato, S., et al. 2005, AJ, 129, 776

Nakano, T., Hasegawa, T., & Norman, C., 1995, ApJ, 450 183

Nakamura, F., & Li, Z.-Y., 2006, ApJ, 237, 52

Nielbock, M., Chini, R., Muller S. A. H., 2003, A&A, 408, 245

Ohashi, N,. Hayashi, M,. Kawabe, R., & Ishiguro, M., 1996 ApJ, 466, 317

Ohashi, N,. Hayashi, M,. Ho, P,T,P., & Momose, M., 1997a, ApJ, 475, 211

Ohashi, N,. Hayashi, M,. Ho, P,T,P., Momose, M., Tamura M., Hirano, N., & Sargent, A, I. 1997b, ApJ, 488, 317

Ohashi, N,. Lee, S. W., Wilner, D. J., & Hayashi, M., 1999, ApJ, 518L, 41

Onishi, T., Mizuno, A., Kawamura, A., Tachihara, K., & Fukui, Y., 2002, ApJ, 575, 950

Okumura, K, S., Momose, M., Kawaguchi, N., Kanzawa, T., Tsutsumi, T., Tanaka, A., Ichikawa, T., & Suzuki, T., et al. 2000 PASJ, 52,393

Patel, N. A., Curiel, S., Sridharan, T.K., Zhang, Q., Hunter T. R., Ho, P.T.P., Torrelles, J.M., Moran, J.M., Gomez, J.F., & Anglada, G., 2005, Nature, 437, 109

Pelletier, G., & Pudritz, R. E., 1992, ApJ, 394, 117

Pyo, T.-S., Hayashi, M., Kobayashi, N., Terada, H., Goto, M., Yamashita, T., Tokunaga, A. T., & Ito, Y., 2002, ApJ, 570, 724

Pyo, T.-S., Hayashi, M., Kobayashi, N., Tokunaga, A. T., Terada, H., Tsujimoto M., Hayashi. S. S., Usuda, T., et al. 2005, ApJ, 618, 817

Reipurth, B., Heathcote, S., 1995, S&T, 90, 38

Reipurth, B., Rodriguea, L. F., & Chini R., 1999, ApJ, 118, 983

Reipurth, B., Rodriguea, L. F., Anglada, G., & Bally, J., 2004, ApJ, 127, 1736

Reynolds, S. P. 1986, ApJ, 304, 713

Rho, J. W., William, T., lefloch, B., Fazio, G. G., 2006, ApJ, 643,965

Saito, M., Kawabe, R., Kitamura Y., & Sunada, K., 1996,ApJ, 473, 464

Saito, M., Kawabe, R., Kitamura Y., & Sunada, K., 2001,ApJ, 547, 840

Saraceno, P., Andre, P., Ceccarelli, C., Griffin, M., Molinari, S., 1996, A&A, 309, 827

Shepherd, D. S., & Churchwell, E., 1996, ApJ, 472, 225

Skinner, S. L. 1994, in The nature and evolution of Herbig Ae/Be stars, ed. P.S. The, M. R. Perez, & E.P. I. Van den Heuvel (San Francisco: ASP), 143

Shu,F.H. 1977, ApJ, 214, 488

Snell, R. L., Loren, R. B., & Plambeck R. L., ApJ, 239L, 17

Stanke, T., McCaughrean, M. J., Zinnecker H., 2002, A&A, 392, 239

Tafalla, a., Myers, P. C., & Wilner, D. J., 1994, Clouds, Cores, and Low Mass Stars ASP Conference Series, Vol. 65, p.391

Takakuwa, S., Mikami, H., Saito, M., & Hirano N., 2000, ApJ, 542, 367

Takakuwa, S., Kamazaki T., Saito, M., & Hirano, N., 2003, ApJ, 584, 818

Takakuwa, S., Ohashi, N., & Hirano, N., 2003, ApJ, 590,932

Takahashi, S., Saito, M., Takakuwa, S., & Kawabe, R., 2006, ApJ, 651, 933

Tatematsu, K., Umemoto, T., Kameya, O., Hirano, N., Hasegawa, T., Hayashi, M., et al. 1993, ApJ, 404, 643

Tsuboi, Y., Koyama, K., Hamaguchi, K., Tatematsu, K., Sekimoto, Y., Bally, J., & Reipurth, B., 2001, ApJ, 554, 734

Tsujimoto, M., Koyama, K., Kobayashi, N., Saito, M., Tsuboi, Y., & Chandler, C.J., 2004, PASJ, 56, 341

Tsujimoto, M., Koyama, K., Kobayashi, N., Goto, M., Tsuboi, Y., & Tokunaga, A.T., 2002, AJ, 125, 153

Yorke H.W., & Sonnhalter, C., 2002, ApJ, 569, 846

Yu, K. C., Bally, J., & Devine, D., 1997, ApJ, 485, L48

Velusamy, T., & Langer, W. D., 1998, Nature, 392, 685

Williams, J. P., Plambeck, R. L., & Heyer, M. H., 2003, ApJ, 591, 1025

Wilner, D. J., & Welch, W. J., 1994, ApJ, 427, 898

Wu, Y., Zhang, Q., Chen, H., Yang, C., Wei, y., & Ho, P.T.P., 2005, ApJ, 129, 330

Zhang, Q., Hunter, T.R., Brand, J., Sridharan. T.K., Molinari, S., Kramer, M.A., & Cesaroni, R., 2001, ApJ, 552L, 167